A High-Strength Ductile Demountable Shear Connector for Composite Floors with Precast Hollow-Core Slab Units

Eliza Feidaki

Submitted for the degree of Doctor of Philosophy

Heriot-Watt University

Energy, Geoscience, Infrastructure and Society (EGIS)

July 2018

Abstract

A novel demountable steel yielding mechanism is proposed for use in steel concrete composite beams in conjunction with precast hollow core slab units. This is the first time in existing literature that an attempt is made to combine deconstructable systems with precast hollow core slab units. The proposed steel yielding mechanism has a unique shape which promotes a ductile force-slip behaviour and allows the facilitation of the deconstruction procedure since it is not fully embedded in the concrete slab. After deconstruction, the structural parts of the proposed demountable connection can be reused in a new building's geometry with proper modifications. Twelve horizontal full scale push out tests were performed to investigate the physical behaviour of the novel demountable connection, to determine the force-slip curves and the failure modes. Theoretical models were developed to predict the strength of the proposed connection based on fundamental mechanics. A number of advanced non-linear numerical models were additionally developed to verify the experimental results using the Abaqus Standard software. The experimental results showed that the proposed connection had high shear resistance and very high slip capacity if properly designed. The deconstruction was implemented within the lab environment by disassembling, reusing structural components and retesting. The theoretical models based on fundamental mechanics and the FEM results can predict the strength obtained in the tests.

Dedication

This PhD thesis is dedicated to my mother, my father and my brother who supports me the most the last four years. I want to thank them for their support and understanding the hard times which I was under pressure.

Acknowledgements

I would like to thank my supervisor Dr. George Vasdravellis for funding this experimental program through EPSRC and for the continuous support of the work undertaken within this research project. Many thanks to Dr. Demitrios Cotsovos for always being willing to answer my questions. Many thanks to all the technicians of the structural lab of Heriot Watt University for being patient and willing to fulfil the demands of this experimental program.

Declaration Statement

ACADEMIC REGISTRY
Research Thesis Submission

Name*:*	Eliza Feidaki		
School:	EGIS		
Version: *(i.e. First, Resubmission, Final)*	Final	Degree Sought:	Doctor of Philosophy

Declaration

In accordance with the appropriate regulations I hereby submit my thesis and I declare that:

1) the thesis embodies the results of my own work and has been composed by myself
2) where appropriate, I have made acknowledgement of the work of others and have made reference to work carried out in collaboration with other persons
3) the thesis is the correct version of the thesis for submission and is the same version as any electronic versions submitted*.
4) my thesis for the award referred to, deposited in the Heriot-Watt University Library, should be made available for loan or photocopying and be available via the Institutional Repository, subject to such conditions as the Librarian may require
5) I understand that as a student of the University I am required to abide by the Regulations of the University and to conform to its discipline.
6) I confirm that the thesis has been verified against plagiarism via an approved plagiarism detection application e.g. Turnitin.

* *Please note that it is the responsibility of the candidate to ensure that the correct version of the thesis is submitted.*

Signature of Candidate*:*		Date:	

Submission

Submitted By *(name in capitals):*	
Signature of Individual Submitting:	
Date Submitted:	

For Completion in the Student Service Centre (SSC)

Received in the SSC by *(name in capitals):*			
Method of Submission *(Handed in to SSC; posted through internal/external mail):*			
*E-thesis Submitted (**mandatory for final theses)***			
Signature:		Date:	

Table of Contents

List of Tables

List of Figures

Glossary

α_b Factor of edge distance and spacing in bolted connection

α Throat thickness of weld

β_w Correlation factor depending on the steel grade

γ_{M2} Safety factor (1.25)

Δ Imposed displacement at the top of the yielding' mechanism steel strips

ε Strain recordings

ϵ_p Engineering plastic strain

ϵ Eccentricity coefficient used in numerical analysis

ϵ_{c1} Compressive strain of concrete in peak stress

ϵ_{cu} Ultimate strain of concrete in compression

ϵ_{tp} Tensile strain of concrete in peak stress

ϵ_{tu} Ultimate strain of concrete in tension

σ_1 Normal stress perpendicular to the weld throat

σ_R Normal stress perpendicular to the axis of the weld

σ_{true} True stress

τ_1 Shear stress (in the plane of the throat) perpendicular to the axis of the weld

τ_2 Shear stress (in the plane of the throat) parallel to the axis of the weld

μ Coefficient of friction between concrete interfaces

ρ Percentage steel ratio in concrete

ψ Dilation angle of concrete used in numerical analysis

A Cross section area of yielding mechanism's vertical wall

A_w Cross section area of the weld between the yielding mechanism and the steel plate at the bottom

A_c Area of concrete shear interface

$A_{c,tooth}$ Area of concrete tooth in contact with the yielding mechanism

A_s Area of steel reinforcement in concrete

b Width of structural hollow section's tube

b_1 Width of plate welded at the bottom of yielding mechanism

c Cohesion coefficient

d Diameter of bolt

d_0 Diameter of drilled holes

DfD Design for deconstruction

DSC(s) Demountable shear connection(s)

$D_{p,strip}$ Top end displacement of a steel yielding's mechanism steel strip

$D_{p,wall}$ Top end displacement of a yielding's mechanism vertical wall

E_s Modulus of Elasticity of yielding mechanism's steel material

E_{cm} Modulus of Elasticity of concrete

e_1 Edge distance between bolts and connected plates in the direction of load transfer

FEM Finite element modelling

f_y Yield strength of yielding mechanism's material

f_{yb} Yield strength of bolts' material

$f_{y,s}$ Yield strength of reinforcement steel

f_u Minimum ultimate strength between two connected steel plates

f_{ub} Ultimate strength of bolts' material

f_c Average uniaxial compressive strength of standard cylindrical concrete samples

f_t Average uniaxial tensile strength of standard cylindrical concrete samples

$f_{t,split}$ Average splitting tensile strength of concrete

$F_{p,walls}$ Shear strength provided by the yielding's mechanism vertical walls

$F_{p,strips}$ Shear strength provided by the yielding's mechanism steel strips

F_p Total shear strength provided by the yielding's mechanism steel strips and vertical walls

$F_{b,Rd}$ Bearing resistance of the connected plates at the bolt holes

$F_{y,b}$ Yield shear strength of the bolts

F_c Shear strength of a cracked shear plane in terms of kN

F_{tooth} Strength of concrete tooth under uniaxial compression

$F_{y,exp}$ Yield strength of the proposed connection obtained from experiments

$F_{max,exp}$ Maximum strength obtained from experiments

$f_{b'}/f_c$ Ratio of compressive strength of concrete under biaxial to uniaxial loading used in numerical analysis

GF Gauge factor

HCU(s) Hollow core slab unit(s)

h Steel strips' height of yielding mechanism

h_1 Steel strips' height within which steel strips' width is minimum

I_{strips} Second moment of area of yielding's mechanism steel strips

I_{walls} Second moment of area of yielding's mechanism vertical walls

$I_{y,w}$ Second moment of area of the weld between the yielding mechanism and the steel plate

K_i Stiffness obtained from experiments

k_r Reduction factor for reduced anchorage of rebars

k_{walls} Stiffness provided by the yielding's mechanism vertical walls

k_{strips} Stiffness provided by the yielding's mechanism steel strips

k Total stiffness provided by the yielding's mechanism steel strips and vertical walls

K_c Ratio of tensile to the compressive meridian used in numerical analysis

$M_{p,strip}$ Plastic moment resistance of a yielding mechanism's steel strip

$M_{p,wall}$ Plastic moment resistance of a yielding mechanism's vertical wall

m Number of bolts used in the proposed demountable connection

n Number of steel strips per side of yielding mechanism

PNA Plastic neutral axis

p_1 Spacing between bolts in the direction of load transfer

$\bar{p}$ Hydrostatic equivalent stress used in numerical analysis

$\bar{q}$ Mises equivalent stress used in numerical analysis

SHS Structural hollow section

t Thickness of yielding mechanism

t_f Thickness of steel section's flange

V_r Difference in voltage ratio from unrestrained to restrained state (strain gauges)

v_u Shear strength of a cracked plane in terms of N/mm^2

w	Steel strips' width of yielding mechanism
YP(s)	Demountable steel -yielding mechanism(s)
Z_p	Lever arm of cross section of yielding mechanism's vertical wall
z_{max}	Distance between a critical point and the gravity centre of the weld

List of Publications

1. E. Feidaki, G. Vasdravellis, 9th December 2015, *Modular composite beams utilizing precast slabs and a steel yielding mechanism: numerical pilot study*, Proceedings of the Infrastructure and Environment Scotland 3rd Postgraduate Conference, Heriot-Watt University, Edinburgh, p. 53-59

2. E. Feidaki, G. Vasdravellis, 13-15 September 2017, *Push out tests of a novel shear connection mechanism for use in demountable precast composite beams*, Proceedings of Eurosteel 2017, ce/papers 1, No. 2 & 3, Copenhagen, Denmark, p. 2060-2069

3. E. Feidaki, G. Vasdravellis, 27-29 June 2018, *Horizontal push out tests on a steel yielding demountable shear connector*, 12th International Conference on Advances in Steel –Concrete Composite Structures (ASCCS 2018), Valencia, Spain, p. 221-228

4. E. Feidaki, G. Vasdravellis, J. He, S. Wang, *A steel-yielding demountable shear connector for composite floors with precast hollow-core slab units*, J. Struct. Eng., ASCE, Manuscript No: STENG-7226 (2018) <under review>

Chapter 1– Introduction

1.1 Introduction

Steel and concrete are the most widely used constructional materials, the production of which generates high levels of carbon dioxide; yet, the demand for their use is continuously increasing. Cement production is considered to be the third largest source of anthropogenic carbon emissions contributing about 5% to global carbon emissions [1.1], while steel and iron production based on recent research contributes as much as 6.5% [1.2]. Future predictions for steel demand shows increase of about 60% by 2050 compared to todays' needs [1.2]. A continuously increasing trend has grown in recent years for reducing carbon dioxide emissions and preserving raw natural resources. It is therefore urgent that new strategies should be employed by the construction sector towards this direction.

Sustainable solutions in construction may be achieved by employing 'Design for Deconstruction' (DfD) principles when designing new buildings [1.3]. According to this concept, the building is designed in such way so that it can be easily deconstructed after the end of its service life and the structural components are reused as extracted or slightly modified in a new building. By employing the deconstruction concept in building design rather than demolishing buildings after the end of their service life, a number of environmental advantages are offered related to the preservation of the natural resources since the steel can be reused, the conservation of energy and reduction of waste that goes to landfill.

However, the DfD concept cannot be applied on steel-concrete composite beams as they are currently constructed. Steel-concrete composite beams are commonly used in UK by a percentage of 70% in non-residential buildings and their construction is related to a number of advantages such as achievement of long spans without propping, fast erection, steel weight savings and construction cost savings [1.4]. The composite connection between the concrete slabs and the steel section is achieved through the use of mechanical shear connectors; the most widely used are the headed studs. Headed studs are welded onto the top flange of the steel section and are embedded in concrete. The concrete slabs of the steel-concrete composite beams are cast on site slabs including or not a profile steel sheeting, solid precast slab units or hollow core slab units.

Enhanced structural performance in steel-concrete composite beams may be achieved by utilizing precast hollow core slab units (HCUs) acting compositely with the steel section [1.5]. In all cases, the monolithic nature of this connection prevents the deconstruction from being implemented because the concrete slabs cannot be separated from the steel sections. Few studies have focused on testing demountable shear connectors for use in steel concrete composite beams; the majority of the demountable shear connectors proposed and tested so far employs a design approach which is limited in conservatively changing the geometrical characteristics and shape of the shear connectors [1.6]. Very few researchers have considered the evaluation of the construction-deconstruction procedure and the feasibility of reusing the structural components.

1.2 Precast Hollow Core Slab Units

Precast floor construction with HCUs is very popular. It is estimated that 30 million m^2 of such units are produced every year in Europe. This particular type of precast slab offers a number of advantages such as fast and easy on –site installation, quality control of the final products and promotion of a cost-effective way of construction [1.7]. The HCUs include a number of tubular voids spanning through the full length of the units.

Figure 1.1 HCUs

Some types of HCUs include oval holes produced by the slip-forming technique. Figure 1.1 shows HCUs produced by the slip forming technique. The self- weigh of the slab units can be reduced as much as 50% compared to solid ones depending on the selected depth and geometry of the unit. The span to depth ratio is usually around 50,

which is considered high enough in order to achieve long spans up to 18 m especially when deeper slabs are preferred. Most of the HCUs used are prestressed [1.7]. The typical width of a HCU is 1200 mm and the slab depth ranges between 150-450 mm, though the most commonly used range lies between 150-300 mm [1.7]. Holes and cut outs are formed to serve construction requirements and are subjected to restrictions imposed by the manufacturing companies, i.e. some of those are mentioned in [1.7], and recommendations according to [1.8]. Design criteria for the construction of the HCUs, construction tolerances and mechanical properties are given in [1.9]. Figure 1.2 shows two parts of HCUs seated on a steel section. The minimum, the nominal and the maximum bearing widths are shown.

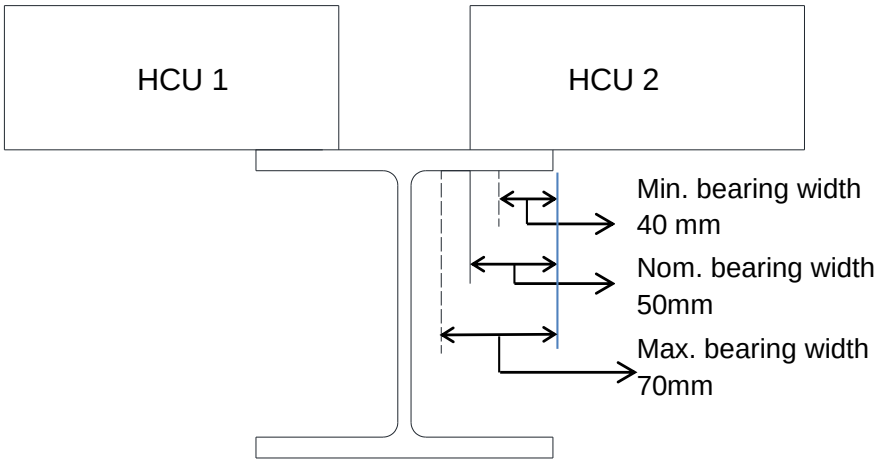

Figure 1.2 Bearing width

The minimum bearing width for non-isolated components is taken equal to 40 mm according to BS-EN 1992-1-1 [1.10]. The nominal bearing width specified in drawings, should account for allowances of spalling at supports and construction inaccuracies in addition to the minimum bearing width. The allowances for spalling at supports are estimated according to [1.10]. The construction inaccuracies include deviation in the setting out, onsite construction process, manufacture and erection process adopted for the precast components; they can be estimated around 15 mm or 3 mm per metre distance between the faces of the steel supports [1.11]. Therefore, the maximum bearing width can be estimated around 70 mm, emanated from the sum of the minimum bearing width, the inaccuracies emanated from the spalling of the units at supports and the construction inaccuracies.

1.3 Objective of the Research

In keeping with the DfD concept to achieve sustainable solutions in construction, this thesis presents a novel demountable shear connector which is used in combination with HCUs for steel concrete composite buildings.

This is the first time in literature review that a deconstructable system is used in combination with HCUs. The proposed demountable shear connection (DSC) offers easy and fast assembly on-site without the use of weld and off-site quality-controlled production of all the component parts. The shear connector proposed is a full –depth shear connector and thus the deconstruction procedure is facilitated by working only from the top side of the steel section. Due to the large shape of the demountable shear connector, the concrete component of the connection is less prone to damages compared to the conventional headed studs which impose a large concentrated force onto the concrete slab. The structural performance of the proposed DSC was evaluated by performing a number of full-scale push out tests in a horizontal test arrangement. The disassembly of the connection was implemented within the lab environment and the feasibility of reusing the structural components was assessed. The yield strength of the proposed DSC during the push out tests was controlled by simplified equations which were based on plastic beam analysis. The shear-friction theory was used to reasonably predict the shear resistance of the concrete slabs of the push out specimens. The experimental results showed that the novel DSC possesses increased strength compared to the conventional headed studs and very high slip capacity which is very important in the case of partial shear connection design of the composite beams. Advanced non-linear numerical models were developed including material and contact non-linearities to validate the experimental results and very good accuracy was obtained.

1.4 Scope of the Thesis

This thesis aims at the development and evaluation of the structural behaviour of a novel demountable DSC to provide composite action between the steel section and the HCUs. The structural behaviour of the proposed DSC was investigated through a number of push out tests. The strength, the stiffness, the ductility, the failure modes and the force-slip curves were established during tests. The construction procedure, the deconstruction procedure and the feasibility of reusing the structural components of the proposed connection were evaluated by assembling, disassembling, reassembling and

reusing the undamaged structural components of the push out specimens within the lab environment. Simplified equations were proposed based on fundamental mechanics to control the strength of the proposed DSC during tests. The shear resistance of the specimens' concrete slab was calculated based on a shear-friction model available in the literature review. Numerical models for the push out specimens were developed to validate the experimental results. The work is arranged in seven chapters. Chapter 2 summarizes the previous published research work carried out on DSCs including a review ranging from early studies. Chapter 3 includes the conceptual design and the description of the proposed DSC. Simplified equations based on fundamental mechanics to predict the yield strength of the proposed DSC obtained from tests are included. Potential damages of the concrete slab during the tests are discussed. Chapter 4 includes the design of the push out specimens, the parameters considered during tests, the test set up, the loading procedures followed and the instrumentation installed on the specimens. Chapter 5 consists of the experimental results including material testing, failure modes, force-slip curves, strain gauges results and comparisons with the theoretical predictions proposed in Chapter 4. Chapter 6 includes the numerical modelling of the push out specimens using the Abaqus Standard software (v.16), the numerical results and comparisons between experimental and numerical results. Chapter 7 summarizes the major findings, the conclusions from the tests performed and the numerical studies and includes future work and recommendations.

1.5 Reference List

[1.1] E. Worrell, L. Price, N. Martin, C. Hendriks, *Carbon dioxide emissions from the global cement industry*, Annual Review of Energy and the Environment, 26 (1), 303-329 (2001)

[1.2] IEA 2010, *World Energy Outlook 2010*, International Energy Agency, 9 rue de la Fédération 75739 Paris Cedex 15, France (2010). <http://www.worldenergyoutlook.org/media/weo2010.pdf> (June 2018)

[1.3] D. Tingley and Davison, *Design for deconstruction and material reuse*, ICE Proceedings, Energy 164 November 2011, IssueEN4

[1.4] Multi-storey office buildings. <http://www.steelconstruction.info/Multi storey_office_buildings> (June 2018)

[1.5] D. Lam, K.S. Elliott, D.A. Nethercot, *Experiments on composite steel beams with precast concrete hollow core floor slabs*, Proc. Instn. Civ. Engrs Structs & Bldgs, May,140, 127-138 (2000)

[1.6] M.C. Moynihan, J.M. Allwood, Viability and performance of demountable composite connectors, J. Constr. Steel Res., 88, 47-56 (2014)

[1.7] K.S. Elliott, C. K. Jolly, Multi-storey Precast Concrete Framed Structures, 2nd edition, Wiley Blackwell, 9600 Garsington Road, Oxford, UK (2013)

[1.8] FIP Recommendations, Precast Prestressed Hollow-Core Floors, FIP Commission on Prefabrication, Thomas Telford, London, UK (1988)

[1.9] BSI (British Standard Institution). BS-EN 1168:2005+A3:2011, Precast concrete products-Hollow core slabs, London, UK (2005)

[1.10] BSI (British Standard Institution). EN 1992-1-1 - Eurocode 2 - Design of concrete structures - Part 1-1: General rules and rules for buildings, European Committee for Standardization (CEN), 92-93 (2004)

[1.11] BSI (British Standard Institution). BS 8110-1:1997- Structural use of concrete. Code of practice for design and construction

Chapter 2-Literature Review

2.1 Introduction

This chapter includes a brief summary of the composite action achieved by the use of welded headed studs embedded in solid concrete as currently constructed followed by a review of the welded headed studs used in conjunction with HCUs. Attention is focused on explaining the basic mechanisms of shear transfer in the conventional structural systems. An extensive review is presented on previous work carried out on demountable shear connectors from 1968 up to date focused primarily on DSCs in steel concrete composite buildings. Recent advances in the use of DSCs in bridges are also discussed. The chapter closes with conclusions and comments on the previously research work carried out on DSCs.

2.2 Composite Action and Composite Action with Headed Studs

Composite action in steel concrete composite beams is achieved through the use of mechanical shear connectors. The role of mechanical shear connectors is to resist the longitudinal slip in the interface between the steel section and the concrete slab and the vertical separation in order to safeguard the composite action. The composite connection allows the member to exhibit increased strength and stiffness compared to beams where no connection between the steel section and the concrete slab is achieved. The strength of the composite cross section is governed by the weakest part of the connection between the strength of the concrete slab, the strength of the steel section and the strength of the shear connection. The strength of each component is calculated by applying rigid plastic analysis. The strength of the concrete component is equal to $0.85\ A_c\ f_c$, where A_c is the area of the cross section of the slab and f_c is the compressive strength of the concrete in cylindrical samples. The strength of the steel section is $A_s\ f_y$, where A_s is the area of the steel cross section and f_y is the yield strength of the steel. The strength of the shear connection is equal to $P_s\ L_s$, where P_s is the shear flow strength of the connection and L_s is the length of a shear span, e.g. half-length in case of simply supported composite beams. The resultant force acting on each component is equal to the lowest strength between the three components. Full shear connection is achieved when the strength of the shear connection is greater than the strength of the weaker of the other two components. The position of the neutral axis of the composite

cross section lies within the strongest component. The number of shear connectors distributed should be enough to transfer the shear forces through the steel concrete interface. When the strength of the shear connection is lower compared to the strengths of the other two components, partial shear connection is achieved resulting in the co - existence of two neutral axes in the composite cross section (since neither the concrete nor steel component fully yields). The number of the shear connectors distributed along the beam is now less than the number required for achieving a full shear connection [2.1]. Degree of shear connection is called the ratio between the strength of the shear connection divided by the strength of the shear connection to achieve full shear connection. Limitations for the use of the partial shear connection in steel concrete composite beams in buildings are provided in Eurocode [2.2]. The condition of full shear connection is related to the condition of full shear interaction; the first is a term to describe the strength of the composite connection while the second one is a term to describe the stiffness of the composite connection as reported in [2.1]. When the relative slip in the interface between the two structural components is fully prevented a full shear interaction is achieved as opposing to partial shear interaction, where limited slips are permitted.

A number of mechanical shear connectors have been used in order to achieve composite action; the most commonly used are the welded headed studs. The shear connectors resist longitudinal slip by working as dowels embedded in concrete. Figure 2.1 shows the mechanism under which the shear force is transferred through the interface. The concrete adjacent to the bearing zone and locally resists stresses as high as seven times the uniaxial compressive strength of the concrete due to triaxility [2.1]. Welded headed studs as opposed to other mechanical shear connectors require slip to develop in the interface, enable them to resist the shear forces while preventing the vertical separation through the presence of the head. A limited height at least four times the diameter of the shank is specified in order to avoid pull out of the concrete element. According to Eurocode 4 [2.2] a limited characteristic slip capacity of 6 mm is specified for a shear connector to be considered as ductile and this is needed for the redistribution of inelastic forces in a composite beam at ultimate limit state. The slip capacity of a headed stud according to [2.1] is about 0.3 times the diameter of the stud, which means that stud diameters above 19 mm and below 25 mm [2.2] should be chosen in practice to meet the ductility criterion. The headed studs are welded on the top flange of the steel

section to achieve a monolithic connection between the two connected structural components.

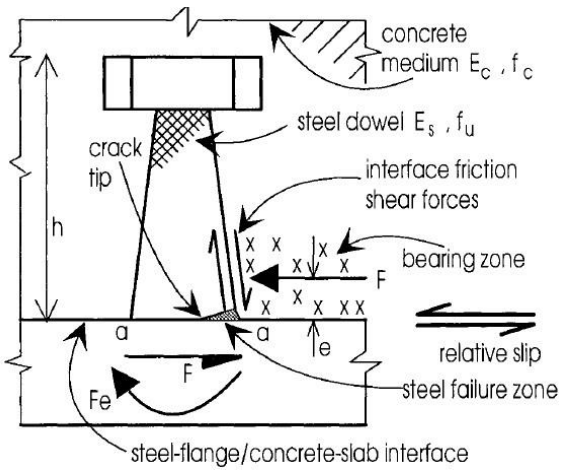

Figure 2.1 Dowel action of welded headed studs [2.3]

The shear connectors impose highly concentrated force onto the concrete slab causing splitting failures. A common failure mode in steel concrete composite beams is the longitudinal splitting which is resulted by the transverse dispersal of this concentrated force [2.3]. Figure 2.2 shows the transverse resultant of this force denoted as 'T' which can cause longitudinal splitting. A longitudinal crack along the length of the composite beam at the position of the shear connectors is formed when the transverse tensile stresses exceed the tensile strength of the concrete. Figure 2.3 shows the splitting failure of a steel concrete composite 'T' beam caused by the movement of a vertical load along the length of the beam [2.3].

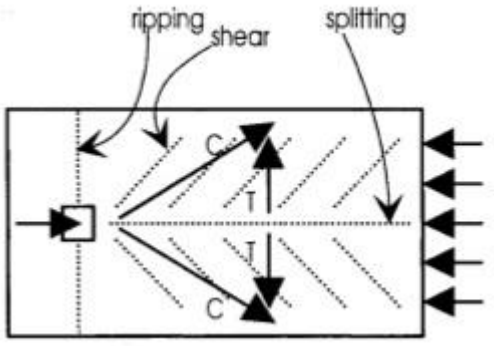

Figure 2.2 Concentrated force imposed by the shear connector [2.3]

In order to alleviate the problem, placing of transverse reinforcement crossing the cracks is recommended. The strength of the connection depends on the amount of the

reinforcement placed across the cracks after splitting occurs. The design of the composite beam against splitting is based on analyses of concrete prisms of various shapes with concepts employed by Leonhart [2.4]. This particular problem related to the structural behaviour of the headed studs is important since the dowel strength of the connector cannot be achieved if a transverse crack is formed close to the bearing zone. The dowel strength of the connectors can be reduced as much as 20% [2.5]. Thus, the role of the transverse reinforcement is to resist the splitting force, to maintain the triaxility state of stress in the bearing zone so as the maximum dowel action can be achieved and to change the type of the failure mode from brittle to ductile after splitting occurs.

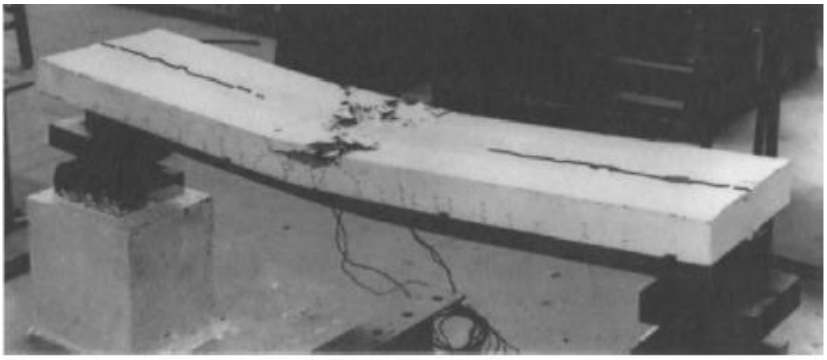

Figure 2.3 Splitting failure of composite 'T' beam [2.3]

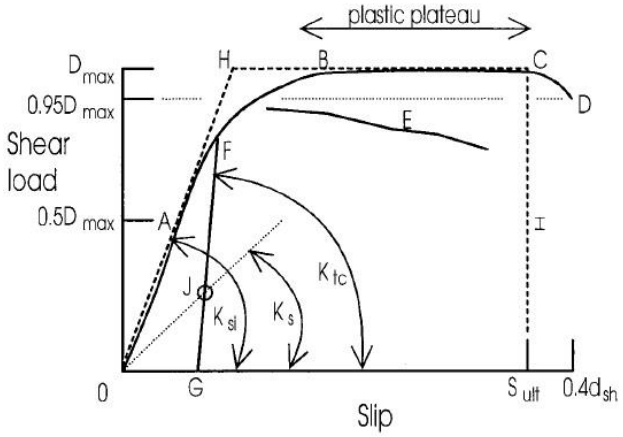

Figure 2.4 Schematic force-slip behaviour of a ductile welded headed stud embedded in *in situ* concrete [2.3]

A typically used 19 mm diameter welded headed stud embedded in solid concrete slabs of medium concrete strength can achieve mean dowel strength of about 130 kN in push out tests [2.3]. A typical force-slip behaviour of a ductile headed stud embedded in *in situ* concrete is shown in Figure 2.4.

The welded headed studs became very popular since there is a lot of relevant experimental data available in combination with standard design methods. The installation procedure is easy and fast. The behaviour of the welded headed studs is studied by many researchers and well documented, e.g. Oehlers and Bradford [2.1, 2.3], Ollgaard et al. [2.6], Oehlers and Coughlan [2.7], and Johnson [2.8]. The force –slip behaviour and shear strength of the headed studs is currently determined by push out tests performed according to Annex B of Eurocode 4 [2.2] which provide instructions for the test set up, the casting, the reinforcement lay out and the characteristic strength derivation.

The use of the welded headed studs is associated with a number of disadvantages. A number of safety protection measures should be satisfied before the welding process take place related to fire and gazes exposure, oxygen deprivation and noise. The quality of the final work strongly depends on the technical operatives that undertake the job. Wet environments influence the welding process. Potential damage in the weld requires the removal of a large area of the structure in order to be repaired. From a structural point of view, the concentrated load transferred through the headed studs to the concrete component makes the slab prone to splitting cracking, as it was previously explained.

Additionally, a steel concrete composite connection including welded headed studs cannot be deconstructed because of the monolithic nature of the connection. Any potential effort to take apart the concrete slab and the steel section would cause unrecoverable damages to the structural components.

2.3 Composite Action with Headed Studs Embedded in Hollow Core Slab Units

Figure 2.5 shows a segment of a steel concrete composite beam using welded headed studs in conjunction with HCUs. The welded headed studs are pre-welded to the top flange of the steel section. The HCUs include alternate pre-opened cores for the placement of transverse reinforcement of around 500 mm length. The ends of the HCUs may be squared or chamfered. Figure 2.5 shows HCUs with chamfered ends. The transverse joint between adjacent HCUs is usually filled with medium to high workability concrete characterized by medium strength and consolidated by manual vibration. The diaphragm (in -plane) forces are transferred with the aid of the shear key, which is a special formation of the ends of the HCUs found transversely to the steel section axis'.

A well compacted amount of *in situ* concrete is placed and consolidated around the welded headed studs. The spacing between the shear connectors is chosen depending on the degree of shear connection that needs to be achieved.

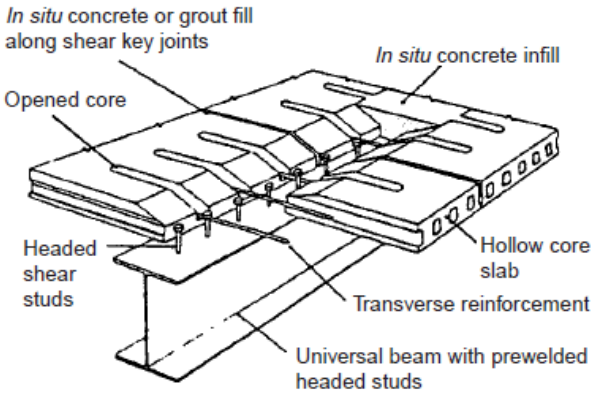

Figure 2.5 Typical 3d segment of a composite beam with HCUs [2.11]

The composite action between the steel section and the HCUs has been extensively investigated by Lam [2.9] and Lam et al. in [2.10-2.12]. A new horizontal test set up arrangement for push out tests was established and validated against the standard one included in Annex B of Eurocode 4 [2.2]. The standard tests according to Annex B of Eurocode 4 [2.2] are performed in a vertical test arrangement and the specimens include *in situ* concrete slabs of 600x600 mm size casted in a horizontal position. The reasons for the development of horizontal test arrangement adopted by [2.9] are a) practical, since the typical dimensions of HCUs are usually larger than the dimensions of the *in situ* concrete slabs specified in Eurocode 4 [2.2]; the reinforcement lay out is also unsuitable for HCUs. According to the tests specified in [2.2] the *in situ* concrete slabs of the push out specimens include longitudinal and transverse rebars placed every 150 mm. Only transverse reinforcement is placed in HCUs; b) constructional; and c) safety as the method of construction of the push out specimens according to [2.2] is not suitable when HCUs are used in specimens. According to [2.2] the steel section is placed vertically and subsequently two slabs are attached on it. When HCUs are used the handling of the slabs including precast- *in situ* concrete interfaces should be avoided after casting. Additionally, the shear strength obtained from the standard push out tests may be affected by frictional forces which are introduced to the base of the concrete slabs of the specimens due to the vertical test set up arrangement as reported in [2.9]. The horizontal test arrangement [2.9] was validated by conducting additional tests including specimens with *in situ* concrete slabs casted according to [2.2]. The shear

strength obtained from the push out tests using the horizontal test arrangement was compared to the shear strength derived from various Standards and good correlation was achieved [2.9].

A number of test variables have been identified in 72 push out tests performed in [2.9] including the transverse steel ratio percentage, stud size, depth of HCUs, gap size between ends of HCUs, end profiles of the HCUs, squared or chamfered, and *in situ* concrete infill strength. Three failure modes were identified composing of concrete cone failure before yielding of studs, yielding of studs with no concrete failure and mixed failure mode. The push out results showed that the key structural component of the connection is the transverse reinforcement controlling the ductility of the connection and resisting the splitting forces. Figure 2.6 shows the typical force-slip behaviour of two push out specimens including high and low reinforcement ratio.

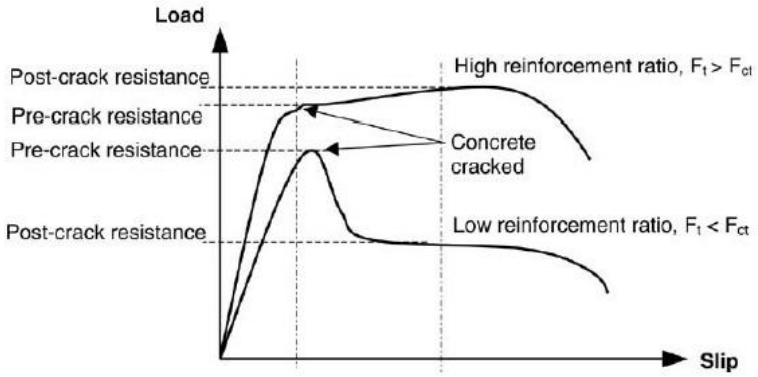

Figure 2.6 Schematic force-slip behaviour of welded headed studs in HCUs [2.9]

The specimens including low reinforcement ratio exhibited low ductility not reaching 6 mm of slip. Indicatively, the maximum recorded load of a ductile headed stud of 19 mm diameter was around 130 kN at 6 mm of slip. Design equations were proposed for the ultimate limit state based on the push out tests results. Beam test results in [2.11] showed that the composite action between the steel section and the HCUs increased by 70% compared to the steel beam itself and the initial stiffness was also much higher. The experimental results were verified with numerical results in [2.12]. Two dimensional FEM were developed in [2.13] aiming at verifying and expanding the previously obtained experimental results. The effective width of the steel concrete composite beams utilizing HCUs was investigated with the aid of additional compressive tests on HCUs and numerical results obtained by Lam in [2.14], Lam and

El-Lobodi [2.15] and El-Lobodi and Lam in [2.16]. A simplified approach mentioned in [14] suggested that the effective width can be considered equal to L/5, where L is the span of the composite beam. A detailed design example of steel concrete composite beams including HCUs is presented in [2.17] by Lam and Uy.

The extensive research work of all the studies mentioned above led to two publications from the Steel Construction Institute of the documents P287 [2.18] and later of P408 [2.19], according to provisions of Eurocode 4 [2.2], for detailed design of steel concrete composite beams including welded headed studs and HCUs.

Recently, twenty push out tests were performed in 19 mm welded headed studs in combination with HCUs including structural topping by Araújo et al. [2.20], who used a modified vertical test set up to suit the provisions of Eurocode 4 [2.2]. They found that the strength of the *in situ* concrete infill and the steel ratio are the most important parameters controlling the shear strength and the ductility of the connection. Indicatively, the maximum recorded shear strength in the push tests showing ductile mode was around 130 kN at approximately 6 mm relative slip.

2.4 Demountable Shear Connectors

One of the earliest research works aimed at developing an alternative rigid connection against the more conventional one which employs welded headed studs was performed by Dallam [2.21] and Dallam and Harpster [2.22] who used high strength friction grip bolts. The shear transfer mechanism developing when using this type of bolts is based on the friction at the steel-concrete interface triggered by the tightening of the bolts. Therefore this type of bolt usually presents high initial stiffness. Dallam [2.21] performed twelve push out tests using 13, 16 and 19 mm diameter bolts and headed studs embedded in normal weight and high quality concrete. The results showed that the friction grip bolts had very high initial stiffness, increased resistance against slip under service load and almost double ultimate shear strength in relation to the welded headed studs. The latter was justified by the superior mechanical characteristics of the high strength friction grip bolts compared to the welded headed studs used. Dallam and Harpster [2.22] performed six beam tests and thirteen accompanied push out tests aiming primarily at validating the results taken from the push out tests. The shear strength of the shortest bolts used in tests was found similar to the one obtained from

the push out tests. The shear strength of the longest bolts used in tests was found higher in beam tests compared to the one taken from the push out tests.

Marshall et al. [2.23] also investigated the performance of high strength friction grip bolts continuing the work of Sattler [2.24]. They performed eleven push out tests using 16 mm diameter bolts and *in situ* and precast slab units with 36-50 N/mm^2 compressive cube strength. The parameters investigated were the level of pretension force applied to the bolts, the concrete strength and the casting procedure adopted for the construction; *in situ* and precast slab units were used. Higher resistance to slip was exhibited by the specimens with level of pretension force applied onto the bolts higher. The shear capacity of the high strength friction grip bolts was higher by 30% compared to that of the welded headed studs of equal diameter. The beam tests were arranged in two groups; the first one included precast slab units of 63 N/mm^2 concrete cube strength while the second one included *in situ* concrete slabs characterized by a 40 N/mm^2 concrete cube strength. The strains developed to the steel and concrete component and the deflection of the composite beams belonging to the first group were measured during tests. The results showed that the experimental results were predicted by theoretical calculations considering a full shear connection. The ultimate load was higher by 40-65% for the case of the beams belonging to the first testing group. The sequence of failure was not described clearly though. They concluded that the steel concrete composite connection proposed had adequate ductility and robustness in relation to non-composite cross sections and that the slip in the interface can be minimized under service loading on condition that full shear connection is achieved.

The work of Dedic and Klaiber [2.25] focused on post- installed shear connectors for strengthening old bridges decks. They conducted eleven push out tests including high strength friction grip bolts, double nut bolts with a single embedded nut and welded headed studs to draw comparisons. Figure 2.7 shows the post-installed shear connectors tested by the researchers. Figure 2.8 shows the average force-slip curves (kip-in) obtained from the push out tests. The DSC exhibited superior performance compared to the welded headed studs in terms of initial stiffness and ductility. The welded headed studs exhibited reduced ductility below 4 mm. The shear capacity was similar between all the shear connectors. The force-slip behaviour of the bolts was unstable when the load reached 89 up to 200 kN, as shown in Figure 2.8. This can be explained by the movement of the bolts inside the drilled holes of the top steel flange until complete

bearing of the bolts occur at the drilled holes. The researchers concluded that the DSC tested is capable of carrying shear forces in the interface between concrete and steel component and can be used with safety in rehabilitation works. They also suggested that the DSC can be used in new structures too.

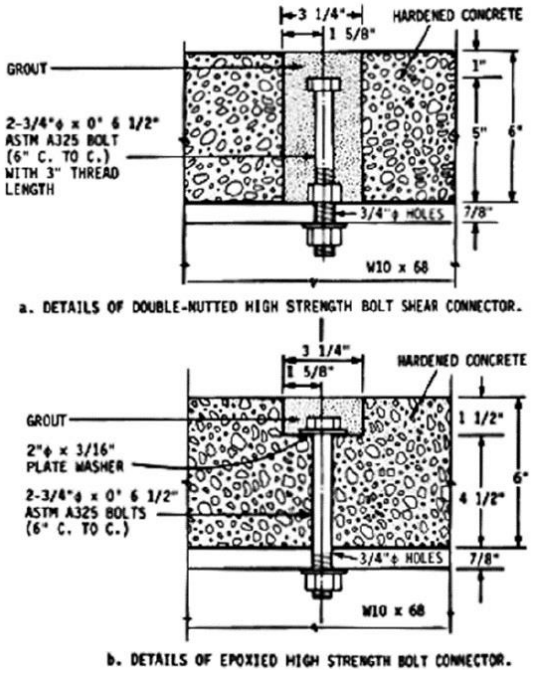

Figure 2.7 DSC tested by Dedic and Klaiber [2.25]

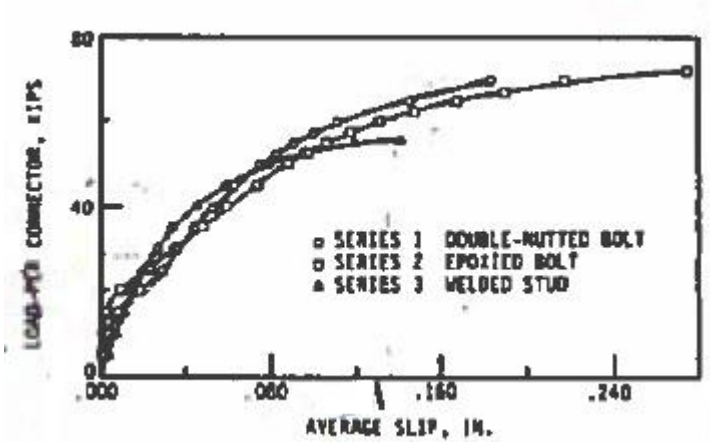

Figure 2.8 Force-slip curves (kip-in) of DSC tested by Dedic and Klaiber [2.25]

More recently, Hungerford in [2.26], Kayir in [2.27] and Schaap in [2.28] tested the high strength friction grip bolts and the double nut bolts including additionally adhesive anchor bolts focusing on strengthening the floor systems of existing bridges too. They conducted tests on post installed shear connectors of 19 mm diameter under static and dynamic loading and proposed design equations for the ultimate strength. Kwon et al.

in [2.29] following their research work performed eight single –shear connector tests on these bolts choosing a bolt diameter of 22 instead of 19 mm. Figure 2.9 shows the post installed shear connectors tested by Kwon at al. Figure 2.10 shows the force-slip curves of the high strength friction grip bolts, denoted as HTFGB, and the force-slip curves of the double nutted bolts, denoted as DBLNB. Since the high strength friction grip bolts use the friction force to transfer the load, the behaviour is initially characterized by high initial stiffness followed by a large slip at the interface till the bearing of the shank of the bolt to the drilled holes. Subsequently, the shear resistance is provided by the bolt bearing against the holes. The behaviour of the double nut bolts was characterized by inconsistency due to the random movement of the bolts inside the drilled holes causing different amounts of slip from specimen to specimen. The adhesive anchor bolts exhibited the lowest stiffness, probably because the behaviour of this type is dependent on the torque applied during the installation of the bolts. All the shear connectors exhibited adequate ductility and failed primarily in shear. The concrete in the bearing zone of the double nut bolts was not crushed due to the large bearing area provided by the presence of the nut. Kayir's equation [2.27] for the calculation of the ultimate strength of post installed shear connector was found to yield conservative results.

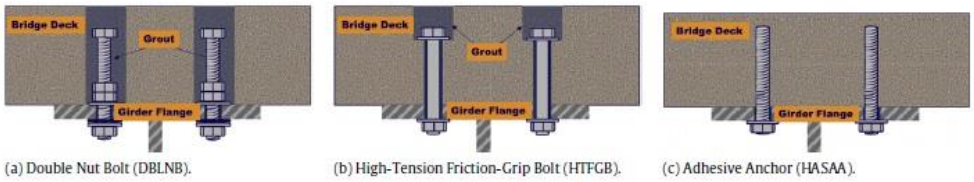

Figure 2.9 Post installed shear connectors tested by Kwon et al. [2.29]

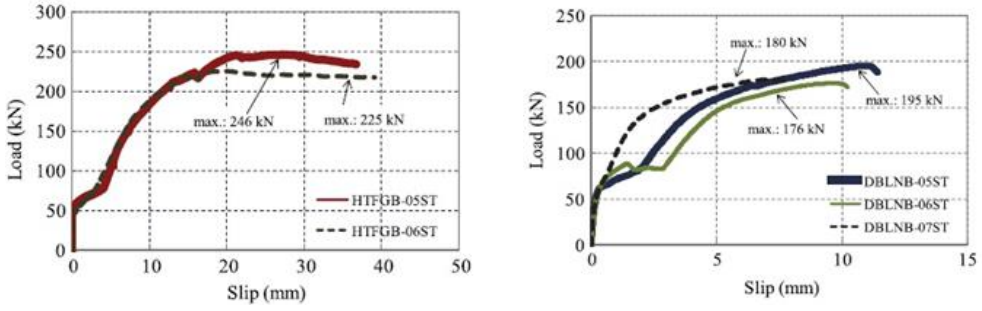

a) b)

Figure 2.10 Push test results of a) High Strength Friction Grip Bolts and b) Double Nutted Bolts tested by Kwon et al. [2.29]

Since the work of Known et al. focused on existing bridges, the primary target was the fatigue and static strength determination of the post installed shear connectors, proposing design equations for the former. Beam tests were performed by the researchers in [2.30] and found that a partial degree of shear connection around 30% is adequate to result an increase in the beam capacity by 40% compared to a non-composite beam. They further conducted analytical and numerical studies and suggested that the ductility of the beams may be increased if the shear connectors were distributed in a non-uniform order near to the ends of the beam. This conclusion was additionally verified by performing a beam test using the adhesive anchor bolts. The results of their research work found implementation on an existing non composite bridge in Texas.

Lee and Bradford in [2.31] in an attempt to find environmentally friendly solutions for deconstruction proposed the use of the common high strength friction grip bolts in combination with precast geo-polymer concrete slab units instead of the common ordinary Portland cement concrete slabs. They performed five push out tests and they developed a simple shear connection numerical model to verify the experimental results. The test parameters were the diameter of the holes drilled in the steel flange which was 24 and 28 mm and the pretension force. Figure 2.11 shows the force-slip curves obtained in tests. The behaviour of the high strength friction grip bolts was characterized by three trends showing similar behaviour to the post installed shear connectors tested by Kwon et. al. The results presented in Figure 2.11 are given for the total number of the demountable shear connectors used in a specimen and should be divided by 4, apart from the results taken for the specimen of M20 bolt size, 8.8 steel grade and full pretension which should be divided by 8 to obtain the strength of an individual shear connector. The strength and the ductility exhibited by those shear connectors are between the highest of all the shear connectors proposed and presented in this literature review. Indicatively, the maximum shear strength achieved was around 200 kN with corresponding relative slip above 25 mm. The researchers were also experimented with the deconstruction procedure by unloading the bolts within the service loading and subsequently re-pretensioning the bolts and then re-loading to failure. Rowe M. and Bradford M.A. in [2.32] developed a simple mechanistic model to simulate the multi-stage force-slip behaviour of the high strength friction grip bolts in steel concrete composite beams.

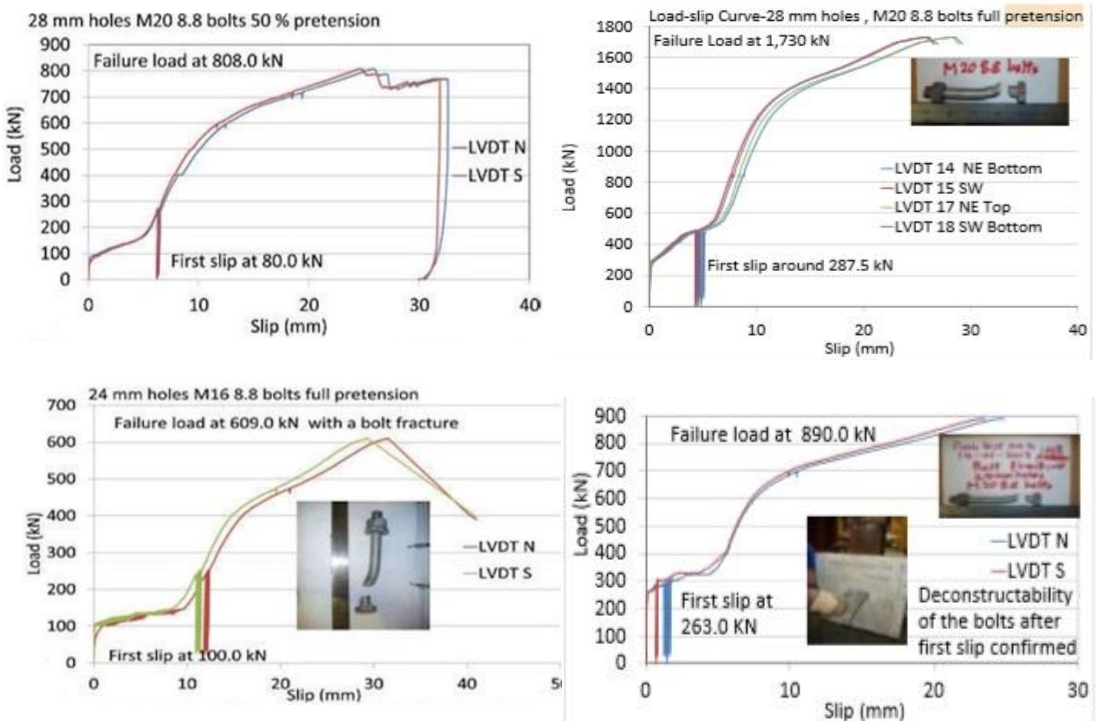

Figure 2.11 Force-slip curves obtained by Lee et.al [2.31]

The DSC was also simulated by Bradford M.A. and Pi Y.L. in [2.33] who developed a non- linear FEM model by performing hand calculations and incorporating non –linear materials. The same DSC was later investigated by Liu et al. in [2.34] who performed numerical FEM models and parametric studies to further expand the push out test results previously obtained by Lee and Bradford. The numerical parameters investigated were the pretension force, the diameter of the drilled holes, the tensile strength of the DSC and the compressive strength of the slab. They found that the parameters that mostly influence the behaviour of the DSC were the pretension force under service loading and the tensile strength and the diameter of the bolts under ultimate loading. Numerical parametric 3D models of composite beams were additionally developed in [2.35, 2.36] using the Explicit solver of Abaqus software and including quasi-static analyses. The results showed that the partial shear connection was capable of achieving higher ultimate strength compared to the counterpart non-composite beam.

Eventually, Ataei et al. [2.37] investigated the structural performance of the high strength friction grip bolts in geopolymer precast slab units in three full scale composite beam tests subjected to monotonic loading. One supplemental test with double nut bolts embedded in *in situ* geopolymer slabs was performed to be used as a reference. The

results showed that the reference beam achieved higher capacity compared to the one with the high strength friction grip bolts. They evaluated the deconstruction procedure by loading one composite beam up to 40% of the expected failure load, cycled 25 times between 5 and 40% of this expected failure load and then unloading. The deconstruction was implemented by removing the slabs with the aid of cranes as shown in Figure 2.12. They concluded that all the structural components of the system could be reused in a new beam within the service range of loading since no damages were seen.

Figure 2.12 Deconstruction of composite beam using high strength friction grip bolts [2.37]

Chen et al. [2.38] investigated the same type of DSC independently of the other researchers mentioned above by conducting ten push out tests, developing a mechanistic model to predict the shear capacity of the connector and by conducting parametric studies using the Abaqus software.

Pavlovic et al. [2.39] performed four push out tests in double nut bolts in conjunction with precast slab units of C30/37 strength class and developed non-linear numerical models. The bolts were of 16 mm diameter and of 8.8 steel grade. Figure 2.13 shows the non-linear numerical models which were developed using the Abaqus/Explicit software. FEM models of welded headed studs were additionally created. The numerical results showed that the double nut bolts entered faster to the plastic region than the welded headed studs, showing a lower initial stiffness by 50%. Two possible reasons were given for that. The first reason was the existence of threads in the interface between the steel and concrete. The second reason was the reduced bearing capacity in a region towards the nut. The latter was further investigated by modelling

the behaviour of one double nut bolt and one welded headed stud with similar characteristics. The shear connectors were enforced to slip at 3 mm, activating their strength by 90%. Since the embedded nut of the double nut bolts provides a large bearing area the stresses in front of the nut decrease and the bearing zone moves upwards above the nut, due to inclination of the nut. The ultimate shear strength was similar between the two shear connectors.

Figure 2.14 shows the experimental force-slip curves of the two shear connectors superimposed with the numerical ones. A failure criterion was established aiming at investigating the failure modes, taking into account the interaction of axial, shear force and bending moment. Parametric studies were conducted aiming at finding those limits within which the bolts behaves with ductility, by varying the height to diameter ratio. A new factor was proposed for the reduction of the shear resistance which fitted better with the numerical results. Eurocode 3 [2.40] failed to predict the shear capacity of the double nut bolts by 20%.

Pavlovic et al. in [2.41] further performed a number of push out tests in double nut bolts of 16 and 24 mm diameter embedded in concrete pockets of precast slab units. The double nut bolts with the largest diameter achieved the highest stiffness, shear strength of 220 kN and adequate ductility of around 8 mm.

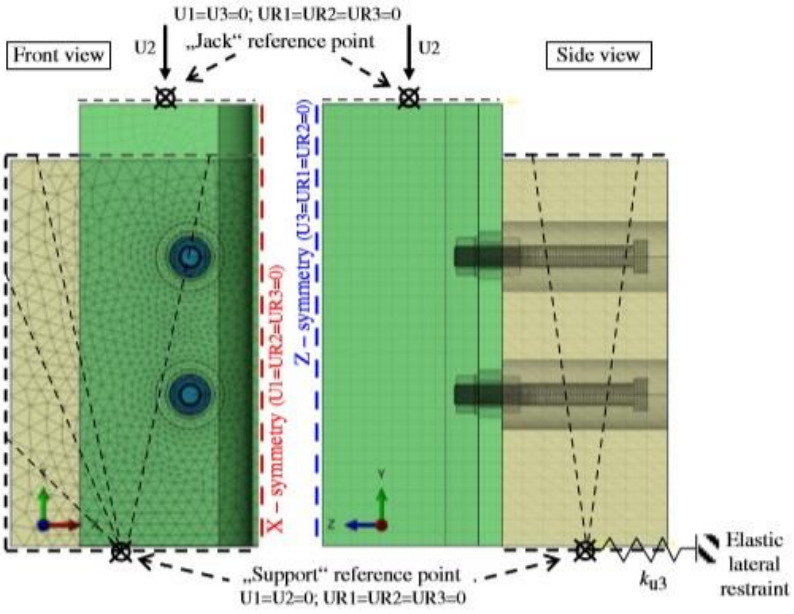

Figure 2.13 Numerical model developed by Pavlovic et al. [2.39]

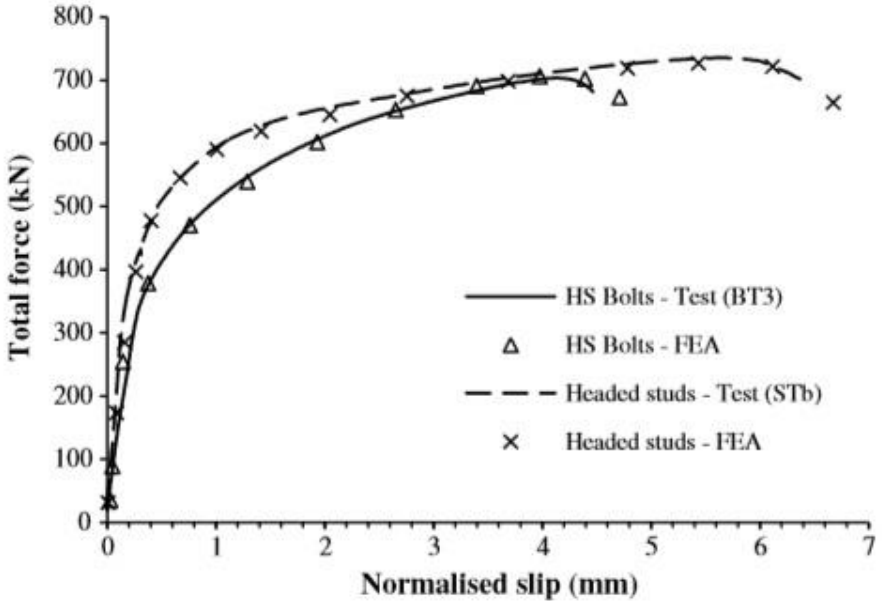

Figure 2.14 Average push out tests results obtained by Pavlovic et al. [2.39]

Two types of blind bolts offering the advantages of one side installation were investigated by Mirza et al. [2.42] in push out tests and Pathirana et al. [2.43] in beam tests. Figure 2.15 shows the blind bolts tested and Figure 2.16 shows the force-slip curves obtained. The first type of blind bolts exhibited satisfactory performance in terms of strength and ductility, showing a similar stiffness to the welded headed studs, which additionally were tested to draw comparisons. The shear capacity of an individual blind bolt was around 90-100 kN taken from the results showing in Figure 2.15 by dividing the total shear strength by 8.

Figure 2.15 Blind bolts tested by Mirza et al. and Pathirana et al. [2.42, 2.43]

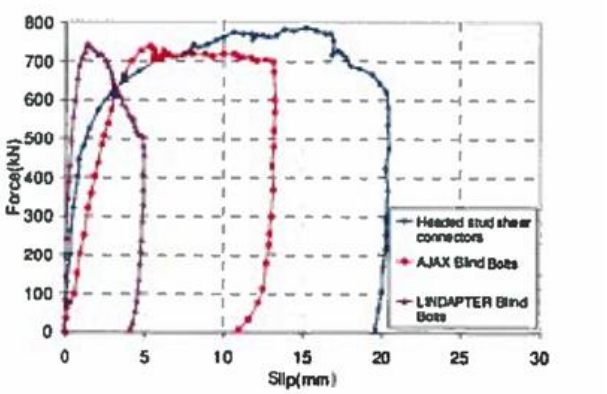

Figure 2.16 Push out test results of blind bolts [2.42]

The second type of blind bolts exhibited very high initial stiffness showing a brittle failure mode. The installation of the second type of blind bolts requires the expansion of the sleeves of the bolts inside the concrete making it prone to local damages in the surrounding concrete when loading. Thus, the failure modes of the blind bolts were associated to concrete cracking and crushing together with pull out failure. The performance of the blind bolts in beam tests was satisfactory. The researchers experimented with the deconstruction procedure by unbolting and re-bolting several bolts in a loading level up to 40% of the ultimate design load of the demountable beam and observed no degradation of the shear connection upon further increase of the loading. The blind bolts were used in retrofitting existing steel concrete composite beams in [2.44, 2.45]. The dynamic behaviour of the bolts was later investigated by Henderson et. al. in [2.46, 2.47, 2.48] who performed push out and beam tests. Time dependent effects on steel concrete composite beams with blind bolts were investigated by Ban et al. in [2.49].

An innovative demountable shear connector embedded in concrete was firstly presented and tested in [2.50] by Lam and Saveri and later in [2.51] by Lam et al. in eight push out tests. The shear connector derived from proper process of standard T.W. Nelson studs of 19 mm diameter and 16 mm threaded part and were formed either with a collar or not. Figure 2.17 shows the demountable shear connectors proposed. The parameters investigated were the stud collar size and the concrete strength as shown in Figure 2.18. Figure 2.19 shows the test results obtained from the push out tests including additional tests in welded headed studs to draw comparisons. The failure modes of the DSCs included stud fracture and concrete crushing. The ultimate strength of the connection derived from the push out tests was similar between the headed studs and the

demountable shear connectors, independent on the collar size used for the latter. The shear capacity obtained was around 70-90 kN for all specimens in which similar concrete strength was utilized. The increased concrete strength used for one test, little affected the ultimate strength, by 20%. Ductility requirements were fulfilled according to Eurocode 4 [2.2]. The force-slip behaviour of the shear connectors proposed was predicted by FEM analyses and equations were provided in [2.52] by Dai et al. who further performed numerical parametric analyses.

Figure 2.17 DSC tested by Lam and Saveri [2.50]

Ref.	Concrete Cube Strength, f_{cu} (MPa)	Stud Type	Max. Load per stud (kN)	Slip at Max. Load (mm)	Mode of Failure
PT 1	19.85	16mm	75.0	8.75	Stud fracture
PT 2	21.45	17mm collar	93.5	7.94	Stud fracture
PT 3	20.10	18mm collar	71.9	22.03	Concrete crushing
PT 4	25.20	18mm collar	81.5	18.22	Concrete crushing
PT 5	29.90	18mm collar	90.0	21.25	Concrete crushing
PT 6	61.38	18mm collar	107.5	22.03	Stud fracture
PT 7	20.10	19mm welded	71.6	5.20	Concrete crushing
PT 8	29.90	19mm welded	92.7	9.00	Concrete crushing

Figure 2.18 Test program and failure modes of push tests tested by Lam et al. [2.51]

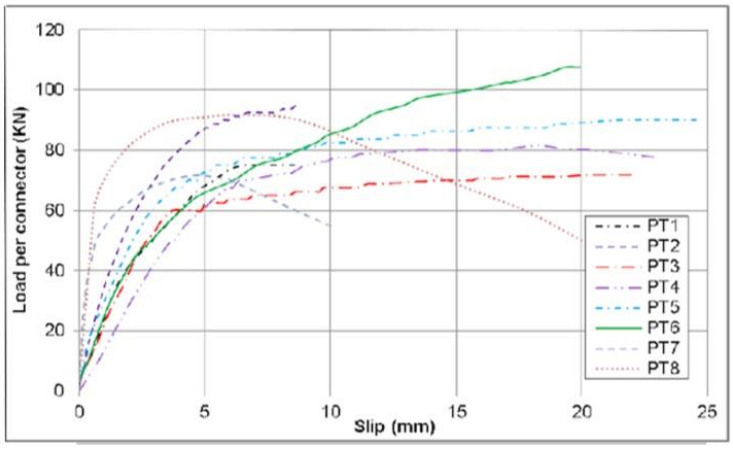

Figure 2.19 Push test results obtained by Lam et al. [2.51]

Moynihan and Allwood in [2.53] were the first that tested those type of demountable shear connectors embedded in *in situ* concrete slabs formed with profile steel sheeting in three full scale beam tests. Their research work aimed at evaluating the construction and deconstruction procedure of the composite beams. The performance of the demountable shear connectors was compared to the one of welded headed studs published elsewhere. The deconstruction procedure was facilitated by the usage of high strength bolts of M20 diameter and oversized holes drilled in the top flange of the steel beam of 24 mm. The beams of 2, 10 and 5 m length were tested in three, six and four point loading, respectively. The deconstructability was achieved by assembling, loading to service, disconnecting and then reassembling and reloading till failure the beams of 2 and 10 m length. The 5 m specimen was derived from the un-failed right part of the 10 m beam and then was loaded till failure. All the beams were successfully demounted and reassembled. The behaviour of the specimens was similar before and after the demounting. The capacities of the steel concrete composite beams were underestimated by the Eurocode 4 [2.2]. A similar behaviour and manner of failure was reported between the DSC proposed and the welded headed studs published elsewhere. Nevertheless, the shear connection was adequate after the testing and the capacity greater than it was predicted. The researchers highlighted that the performance of the DSC may be improved by changing the material and the geometric characteristics of the bolts. They also mentioned that the precast slab units may be used to further speed up the construction procedure. They concluded that the establishment of a reliable design procedure including DSCs needs further research.

Recently, Rehman et al. in [2.54, 2.55] and Lam et al. in [2.56] used the modified threaded studs in combination with concrete slabs formed in a profiled steel decking to create a demountable composite floor system. The researchers performed twelve push out tests and two full scale beam tests including the modified threaded studs and welded headed studs to draw comparisons. The push out test results showed that the behaviour of the modified threaded studs was comparable to the one of the headed studs, satisfying the limited ductility requirements imposed by Eurocode 4 [2.2]. Similarly, the beam test results showed an overall comparable behaviour between the two types of shear connectors given in Figure 2.20 and denoted as DCFS and WCFS for the demountable shear connectors and the welded studs respectively. The researchers concluded that the demountable floor system proposed could be used as an alternative to the conventional

one since the beams could be easily deconstructed at the end of the test not showing any damage of the structural members.

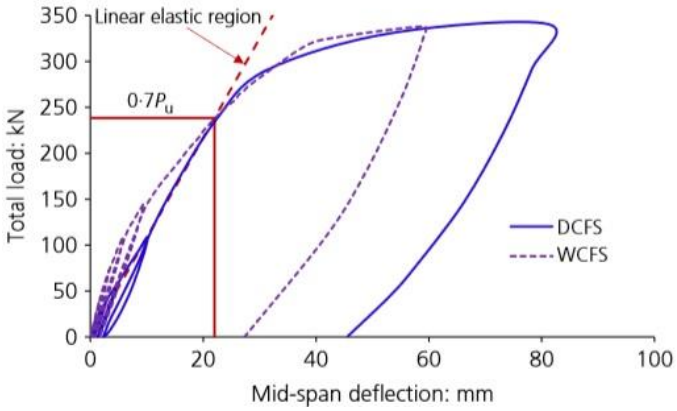

Figure 2.20 Load-deflection curve of the demountable and conventional composite floor system tested by Rehman et al. [2.54]

Suwaed and Karavasilis in [2.57] conceived and tested in push out tests a novel DSC aiming at surpassing the problem of the slippage of the bolts inside the drilled holes of the steel section's flange. This problem has been previously presented by the multistage behaviour showing in the force-slip curves of the high strength friction grip bolts, i.e. push tests conducted by Kwon et. al. and Lee et. al. Figure 2.21 shows the DSC proposed. In order to prevent the slippage a special locking nut in a cone form was used. The connection utilized a number of washers and nuts and slab pockets to fit the steel parts of the connection in such way as to prevent slippage and to delay concrete damage. A number of push out tests were performed and the results showed superior performance to the one of welded headed studs. The DSC was proposed for use in rapid deconstructable bridges using precast slab units.

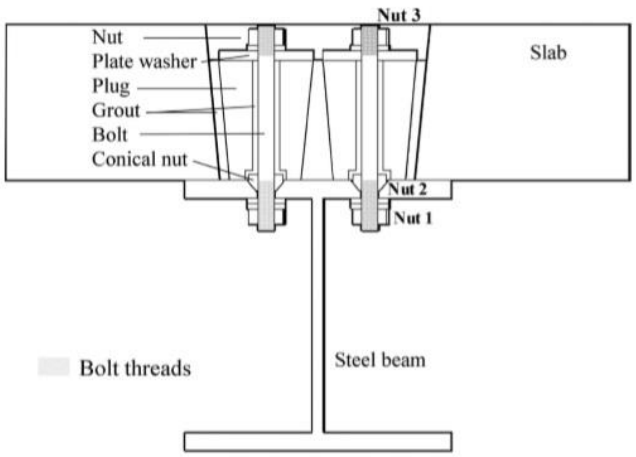

Figure 2.21 Novel DSC with conical nuts by Suwaed and Karavasilis [2.57]

Another novel demountable shear connector was proposed by Yang et al. in [2.58]. The demountable shear connectors were embedded in *in situ* concrete blocks of 500 mm depth and were tested in push out tests. The research work focused mainly on the determination of the shear strength of the DSC precluding potential damages in the concrete component by using concrete slabs of large dimensions. The conceptual design of the proposed DSC aimed at simplifying the deconstruction procedure by unscrewing the bolts only from the bottom side of the beam, thus working only from one side and thus facilitating the deconstruction procedure. The DSC consisted of a short bolt, firstly installed during construction, a large bolt and a coupler between them as shown in Figure 2.22. The bolts failed in shear. The majority of the DSCs exhibited inadequate ductility below 6 mm. Some DSCs including large bolt diameter of 27 mm exhibited ductility around 6 mm.

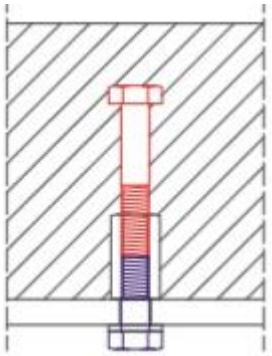

Figure 2.22 Novel DSC tested by Yang et al. [2.58]

Recent innovative deconstructable systems were developed on beam –to –column composite connections. Ataei et al. in [2.59, 2.60] tested a demountable semi-rigid beam –to–column composite connection using precast slab units of reduced content of ordinary Portland cement and post-tensioned bolted shear connectors. Numerical models were additionally developed. They performed three push out test to determine the strength of the post tensioned bolts and full scale tests in composite beam –to –column joints. The composite beam-to-column joint tests showed adequate rotation capacity of the proposed demountable connection exceeding the requirements of Eurocode 4 [2.2] by 50%. A new deconstructable timber-steel composite floor system was investigated by Hassanieh et al. in [2.61, 2.62] who intended to replace the concrete composite slabs with timber ones having reduced weight. A number of push out specimens was designed including screws, bolts and high strength bolts embedded in grouted pockets. The test results showed that the maximum shear resistance achieved in

some push out tests was around 150 kN with adequate ductility of 20 mm.

2.5 Conclusions

The majority of the demountable shear connectors presented herein use pretension and friction forces to transfer the load. The pretension generates the clamping force required to keep the bolts and the connected elements of a joint together. The accuracy that the pretension force is applied depends on the tightening method; some methods may have an error estimation about 25%, i.e. wrench control method. The pretension may be 'relaxed' with time due to many reasons, i.e. temperature changes which can result contractions or expansions of the joints and that further causes changes in the pretension force. The high strength friction grip bolts exhibited a three-stage force-slip behaviour which consists of very high initial stiffness due to friction followed by a zero slip resistance stage till the bearing of the bolts at the drilled holes. This particular problem of the gap around the bolts has been addressed in the past by Johnson and Buckby [2.63] who suggested either grouting this gap after the tightening of the bolts or considering that the ultimate strength of the bolts is the frictional resistance. The gap between the bolt and the drilled hole may result in non -uniform slippages inside the drilled holes along the composite beam and may cause non uniform transfer of shear flows as mentioned by Moynihan and Allwood in [2.53]. There is a limited number of research works dealt with the issue of construction and deconstruction procedure. The issue of facilitating the construction-deconstruction procedure by conceiving a proper structural system is very new and few research works have dealt with this subject so far. Some DSCs recently proposed by Yang et al. [2.58] and focused on this issue showed inadequate ductility. Suwaed and Karavasilis in [2.57] proposed an efficient demountable system though was primarily focused for use on bridges. Ataei et al. [2.37] evaluated the deconstruction procedure in demountable composite beams with high strength friction grip bolts by separating the slabs from the steel section using the aid of cranes within a lab environment.

There are additional practical questions of whether the deconstruction is easily achieved or not since the majority of the demountable shear connectors proposed are embedded in concrete slabs apart from the type of through-friction grip bolts tested by Chen et al. [2.38]. Blind bolts were used by Mirza et al. [2.42] and Pathirana et al. [2.43-2.45].

This type of bolts offers the advantages of one side installation and thus the construction procedure of the beams is facilitated by working from the side of the steel section only. All the previous research work on DSCs summarized in the present literature review use *in situ* concrete slabs, solid or formed in a profile steel decking, and solid precast slab units. There is no demountable structural system that utilizes HCUs for use in steel concrete composite beams. The use of HCUs offer a number of standard advantages as cited in 1.2. The only extensive available research on the composite action achieved between the steel sections and the HCUs has been led by Lam et al. as presented in [2.9-2.15, 2.17] using the conventional welded headed studs. Thus, the concept of deconstruction was out of the scope of their research work.

The present research work aiming at filling the gap of the previously work undertaken on DSCs used in combination with solid concrete slabs proposes a DSC which utilizes HCUs. This is the first time in lit review that HCUs are used in a demountable structural system for use in steel concrete composite beams in buildings. An innovative shear connector to provide composite action between the steel section and the HCUs is proposed having unique features which aim at surpassing common problems associated with the use of the pretension force and the slippage of the bolts inside the drilled holes shown by the high strength friction grip bolts [2.29, 2.31] and the double nutted bolts [2.25, 2.29]. The proposed DSC attempts to facilitate the deconstruction procedures by presenting a full-depth demountable shear connector which can be easily installed and un-installed by working only from the top side of the steel section. Due to the large shape of the steel yielding mechanism proposed, the concrete component of the connection is less prone to damages compared to shear connectors which impose a large concentrated force onto the concrete slab. Compared to other DSCs [2.58] which showed limited ductility, the proposed DSC is expected to achieve high slip capacity based on capacity calculations elaborated in the following chapter.

2.6 Reference List

[2.1] D.J. Oehlers, M.A. Bradford, *Elementary behaviour of composite steel & concrete structural members*, Butterworth-Heinemann, Oxford, UK (1999)

[2.2] BSI (British Standard Institution). BS EN 1994-1-1: 2004: Design of composite steel and concrete structures- Part 1.1: General rules and rules for buildings, London , UK (2004)

[2.3] D.J. Oehlers, M.A. Bradford, *Composite steel and concrete structural members: fundamental behaviour*, Elsevier Science Ltd, Oxford, UK (1995)

[2.4] F. Leonhardt, *Prestressed Concrete, Design and Construction*, 2nd edition, Wilhelm Ernst and sohn, Berlin-Munich, German (1964)

[2.5] D.J. Oehlers, *Splitting Induced by Shear Connectors in Composite Beams*, J. Struct. Eng., ASCE, 115 (2), 341-362 (1989)

[2.6] J.G. Ollgaard, R.G. Slutter, J.W. Fisher, *Shear strength of stud connectors in lightweight and normal-weight concrete*, J. ACI Struct., 8, 55–64 (1971)

[2.7] D.J. Oehlers, C.G. Coughlan, *The shear stiffness of stud shear connections in composite beams*, J. Constr. Steel Res., 6, 273–284 (1986)

[2.8] R.P. Johnson, *Composite structures of steel and concrete: Vol. 1: Beams, slabs, columns, and frames for buildings*, 3rd edition, Blackwell Scientific, Oxford, UK, 32 (2004)

[2.9] D. Lam, *Capacities of headed stud shear connectors in composite steel beams with precast hollow core slabs*, J. Constr. Steel Res., 63, 1160-1174-72 (2007)

[2.10] D. Lam, K.S. Elliot, D.A. Nethercot, *Push-off Tests on Shear Studs with Hollow-cored Floor Slabs*, The Struct. Eng., 76 (9) (1998)

[2.11] D. Lam, K.S. Elliott, D.A. Nethercot, *Experiments on composite steel beams with precast concrete hollow core floor slabs*, Proc. Instn. Civ. Engrs Structs & Bldgs, May,140, 127-138 (2000)

[2.12] D. Lam, K.S. Elliott, D.A. Nethercot, *Designing composite steel beams with precast concrete hollow-core slabs*, Proc. Instn Civ. Engrs Structs & Bldgs, May 140, 139-149, (2000)

[2.13] D. Lam, K.S. Elliott, D.A. Nethercot, *Parametric Study on composite steel beam with precast concrete hollow core floor slabs*, J. Constr. Steel Res., 54 (2), 283-304 (2000)

[2.14] D. Lam, *Composite steel beams with precast hollow core slabs: behaviour and design*, Proc. Strct. Engineering Materials, 4, 179-185 (2002)

[2.15] D. Lam, E. El-Lobody, *Finite element modelling of headed stud in composite steel beams with precast hollow core slabs*, Proc. of the International Conference on Steel and Composite Structures, Pusan, Korea, 14-16 June 2001, 1253-1260 (2001)

[2.16] E. El-Lobody, D. Lam, *Determining the effective width of composite beams with precast hollow core slabs*, Structural Engineering & mechanics, 21(3), 295-313 (2005)

[2.17] D. Lam, B. Uy, *Recent research and development in composite steel beams with precast hollow core slabs*, J. Steel Constr., 37(2), 1-14 (2003)

[2.18] S.J. Hicks, R.M. Lawson, *Design of Composite Beams Using Precast Concrete Slabs*, SCI Publications P287 (2003)

[2.19] G.H. Couchman, *Design of composite beams using precast concrete slabs in accordance with Eurocode 4*, SCI Publication P401 (2014)

[2.20] Daniel de Lima Araújo, Marcel William Reis Sales, Silenio Marciano de Paulo, Ana Lúcia H. de Cresce El Debs, *Headed steel stud connectors for composite steel beams with precast hollow-core slabs with structural topping*, J. Eng. Struct., 107, 135-150 (2016)

[2.21] L.N. Dallam, *High Strength Bolt Shear Connectors-Push out tests*, ACI J. 65 (9), 767-9 (1968)

[2.22] L.N. Dallam, J.L. Harpster, *Composite beam tests with high-strength bolt shear connectors*, Report for Missouri State Highway Department, Department of Civil Engineering, University of Missouri-Columbia, Missouri, USA (1968)

[2.23] W.T. Marshall, H.M. Nelson, H.K. Banerjee, *An experimental study of the use of high strength friction-grip bolts as shear connectors in composite beams*, The Structural Engineer, 49(4), 171-178 (1970)

[2.24] K. Sattler, *Betrachtungen uber die Verwendung hochzugfester Schrauben bei Stahltragerverbund konstructionen*, Vorbericht IVBH (1960)

[2.25] D.J. Dedic, W.F. Klaiber, *High- Strength Bolts as Shear Connectors in Rehabilitation Work*, J. Concr. Int, 6 (7), 41-46 (1984)

[2.26] B.E. Hungerford, *Methods to develop composite action in non- composite bridge floor systems: Part II*., MSc thesis, Dept. of Civil, Architectural and Environmental Engineering, Univ of Texas, Austin, TX. (2004)

[2.27] H. Kayir, *Methods to develop composite action in non-composite bridge floor systems: Fatigue behaviour of post-installed shear connectors*, M.S. thesis, Dept. of Civil, Architectural and Environmental Engineering, Univ. of Texas, Austin, TX. (2006)

[2.28] B.A. Schaap, *Methods to develop composite action in non-composite bridge floor systems: Part I*, M.S. thesis, Dept. of Civil, Architectural and Environmental Engineering, Univ. of Texas, Austin, TX (2004)

[2.29] G. Kwon, M.D. Engelhardt, R.E. Klingner, *Behaviour of post-installed shear connectors under static and fatigue loading*, J. Constr. Steel Res., 66 (4), 532-541, 2010

[2.30] G. Kwon, M.D. Engelhardt, R.E. Klingner, *Experimental Behaviour of Bridge Beams Retrofitted with Post-installed Shear Connectors*, Journal of Bridge Engineering, 10.1061/(ASCE)BE.1943-5592.0000184, 536-545 (2011)

[2.31] M.S.S. Lee, M.A. Bradford, *Sustainable composite beams with deconstructable bolted shear connectors*, Research and Applications in Structural Engineering, Mechanics and Computation, Taylor & Francis Group, London, UK (2013)

[2.32] M. Rowe, M.A. Bradford, *Partial Shear Interaction in Deconstructable Steel-Concrete Composite Beams with Bolted Shear Connectors*, Design, Fabrication and Economy of Metal Structures, International Conference Proceedings 2013, 585-590, Miskolc, Hungary

[2.33] M.A. Bradford, Y.-L. Pi, *Computational Modelling of Deconstructable Composite Steel-Concrete Beams*, Proceedings of the 11th International Conference on Computational Structures Technology, Civil-Comp Press 153, 1-15, Stirlingshire, Scotland (2012)

[2.34] X. Liu, M.A. Bradford, S.S.M. Lee, *Behaviour of high strength friction grip bolted shear connectors in sustainable composite beams*, J. Struct. Eng., 10.1061 /(ASCE) ST.1943-541X.0001090, 04014149 (2014)

[2.35] X. Liu, M.A. Bradford, Q.J. Chen, H. Ban, *Finite element modelling of steel–concrete composite beams with high-strength friction-grip bolt shear connectors*, Journal of Finite Elements in Analysis and Design, 108, 54-65 (2016)

[2.36] X. Liu, M.A. Bradford, A. Ataei, *Flexural performance of innovative sustainable composite steel-concrete beams*, J. Eng. Struct., 130, 282 – 296 (2017)

[2.37] A. Ataei, M.A. Bradford, X. Liu, *Experimental study of composite beams having a precast geopolymer concrete slab and deconstructable bolted shear connectors*, J. Eng. Struct., 114, 1–13 (2016)

[2.38] Y.-T Chen, Y. Zhao, J.S. West, S. Walbridge, *Behaviour of steel–precast composite girders with through-bolt shear connectors under static loading*, J. of Constr. Steel Res., 103, 168–178 (2014)

[2.39] M. Pavlovic, Z. Markovic, M. Veljkovic, D. Budevac, *Bolted shear connectors vs. headed studs behaviour in push out tests*, J. Constr. Steel Res., 88:134-149 (2013)

[2.40] BSI (British Standard Institution). BS EN 1993-1-8:2005 Eurocode 3: Design of steel structures –Part 1-8: Design of joints, London, UK (2005)

[2.41] M. Pavlovic, M. Spremic, Z. Marcovic, D. Budevac, M. Veljkovic, *Recent research of shear connection in prefabricated steel-concrete composite beams*, Journal of applied Engineering Science 12 (2014)1, 279, 75-80 (2014). Retrieved from< http://scindeks-clanci.ceon.rs/data/pdf/1451-4117/2014/1451-41171401075P.pdf> (June 2018)

[2.42] O. Mirza, B. Uy, N. Patel, *Behaviour and strength of shear connectors utilizing blind bolting*, Steel and Composite Structures-Proceedings of the 4th International Conference July, 2010, 791-796

[2.43] S.W. Pathirana, B. Uy, O. Mirza, X. Zhu, *Flexural behaviour of composite steel concrete beams utilising blind bolt shear connectors*, J. Eng. Struct., 114, 181 – 194 (2016)

[2.44] S.W. Pathirana, B. Uy, O. Mirza, X. Zhu, *Strengthening of existing composite steel concrete beams utilising bolted shear connectors and welded studs*, J. Constr. Steel Res, 114, 417–430 (2015)

[2.45] S.W. Pathirana, B. Uy, O. Mirza, X. Zhu., *Bolted and welded connectors for the rehabilitation of composite beams*, J. Constr. Steel Res., 125, 61 – 73 (2016)

[2.46] I.E.J. Henderson, X.Q. Zhu, B. Uy, O. Mirza, *Dynamic behaviour of steel-concrete composite beams with different types of shear connectors. Part I: Experimental study*, J. Eng. Struct., 103, 298–307 (2015a)

[2.47] I.E.J. Henderson, X.Q. Zhu, B. Uy, O. Mirza, *Dynamic behaviour of steel-concrete composite beams with different types of shear connectors. Part II: Modelling and comparison*, J. Eng. Struct., 103, 308–317 (2015b)

[2.48] I.E.J. Henderson, X.Q. Zhu, B. Uy, O. Mirza, *Dynamic behaviour of steel-concrete composite beams retrofitted with various bolted shear connectors*, J. Eng. Struct.,131, 115-135 (2017)

[2.49] H. Ban, B. Uy, S.W. Pathirana, I. Henderson, O. Mirza, X. Zhu, *Time-dependent behaviour of composite beams with blind bolts under sustained loads*, J. Constr. Steel Res., 112, 196–207 (2015)

[2.50] D. Lam, E. Saveri, *Shear capacity of demountable shear connectors*, Proc. of the 10th International Conference on Advances in Steel Concrete Composite and Hybrid Structures, Singapore Research Pub. Services, 2-4 July 2012, Singapore

[2.51] D. Lam, X. Dai, E. Saveri, *Behaviour of Demountable Shear Connectors in Steel-Concrete Composite Beams*, International Conference on Composite Construction in Steel and Concrete VII, ASCE, 618-63, 28-31 July, North Queensland, Australia

[2.52] X. Dai, D. Lam, E. Saveri, *Effect of Concrete Strength and Stud Collar Size to Shear Capacity of Demountable Shear Connectors*, J. Struct. Eng., 10.1061/(ASCE)ST.1943-541X.0001267, 04015025 (2015)

[2.53] M.C. Moynihan, J.M. Allwood, *Viability and performance of demountable composite connectors*, J. Constr. Steel Res., 88, 47-56 (2014)

[2.54] N. Rehman, D. Lam, A. Ashour, *Experimental study on demountable shear connectors in composite slabs with profiled decking*, J. Constr. Steel Res., 122, 178-189 (2016)

[2.55] N. Rehman, D. Lam, X.H. Dai, A. Ashour, *Testing of composite beam with demountable shear connector*, Structures & Buildings, Proceedings of the ICE-Structures and Buildings 1-14 (2017)

[2.56] D. Lam, X. Dai, A. Ashour, N. Rehman, *Recent research on composite beams with demountable shear connectors*, Steel Construction 10, 125-134 (2017)

[2.57] Ahmed S. H. Suwaed, Theodore L. Karavasilis, *Novel Demountable Shear Connector for Accelerated Disassembly, Repair, or Replacement of Precast Steel-Concrete Composite Bridges*, J. Bridge Eng., 22(9), 04017052 (2017)

[2.58] F. Yang, Y. Liu, J. Zhibo, X. Haohui, *Shear performance of a novel demountable steel-concrete bolted connector under static push-out tests*, Engineering Structures, 160, 133-146 (2018)

[2.59] A. Ataei, M.A. Bradford, H.R. Valipour, *Experimental study of flush end plate beam-to-CFST column composite joints with deconstructable bolted shear connectors*, Eng. Struct., 99, 616–630 (2015)

[2.60] A. Abdolreza, M.A. Bradford, R.V. Hamid, *Finite element analysis of HSS semi-rigid composite joints with precast concrete slabs and demountable bolted shear connectors*, J. Finite Elements in Analysis and Design, 122, 16-38 (2016)

[2.61] A. Hassanieh, H.R. Valipour, M.A. Bradford, *Load-slip behaviour of steel-cross laminated timber (CLT)*, J. Constr. Steel Res., 122, 110-121 (2016)

[2.62] A. Hassanieh, H.R. Valipour, M.A. Bradford, *Composite connections between CLT slab and steel beam: Experiments and empirical models*, J. Constr. Steel Res., 138, 823-836 (2017)

[2.63] R.P. Johnson, R.J. Buckby, *Composite structures of steel and concrete: Volume2: Bridges*, 2nd edition, Collins Professional and Technical Books, London, UK (1986)

Chapter 3-Demountable Steel Concrete Composite Beams with Hollow Core Slab Units

3.1 Introduction

The proposed DSC utilizes HCUs and a novel steel yielding mechanism to achieve composite action between the steel section and the HCUs. The conceptual design and the description of the structural system are presented. Simplified equations are given based on fundamental mechanics to control the yield strength of the proposed DCS. This yield strength is used to control the yield strength obtained from the tests and the numerical results are given in the following chapter. Capacity calculations are used to ensure that the connected steel elements have adequate strength in order to avoid steel failures in the tests and the numerical results are given in the following chapter. Potential damages of the concrete slab during the tests are discussed. The shear resistance of the concrete slab is calculated employing the shear- friction theory applied across a crack. At the end of the chapter an indicative example of a composite floor construction including the DSC proposed and conventional headed studs to draw comparisons is presented considering typical design loads, full and partial shear connection.

3.2 Conceptual Design and Description of the Proposed DSC Connection

The proposed steel concrete composite connection utilizes HCUs and a novel steel yielding mechanism denoted as yielding pocket (YP). Figure 3.1 shows a 3d segment of a steel section with two HCUs seated on it and one YP installed. The HCUs include open cores to facilitate the placement of transverse reinforcement for the effective connection between adjacent units. Additional edge cut -outs are required through the depth of the HCU at the edges parallel to the beam axis to accommodate the installation of the YP. The number of the edge cut outs required is dependent on the degree of shear connection (full or partial) of the composite beam. The YP is a steel square hollow section (SHS) having an additional plate welded at the bottom and total length equal to the slab's depth. Vertical elongated holes are cut on the sides of the YP, parallel to the steel section's axis in order to form vertical steel strips. Aligned horizontally slotted holes are also opened on the same sides of the YP. Figure 3.1 shows the YP including the vertical strips and the two aligned horizontally holes formed

in the longitudinal direction of the beam. A rebar passes through the horizontally slotted hole of the YP and it is placed in the middle open core of the HCUs. It is expected that the uplift of the slab is prevented through the middle rebar. However this needs additional experimental studies to ensure that the middle rebar is capable of resisting the uplift forces under the longitudinal bending of a composite beam.

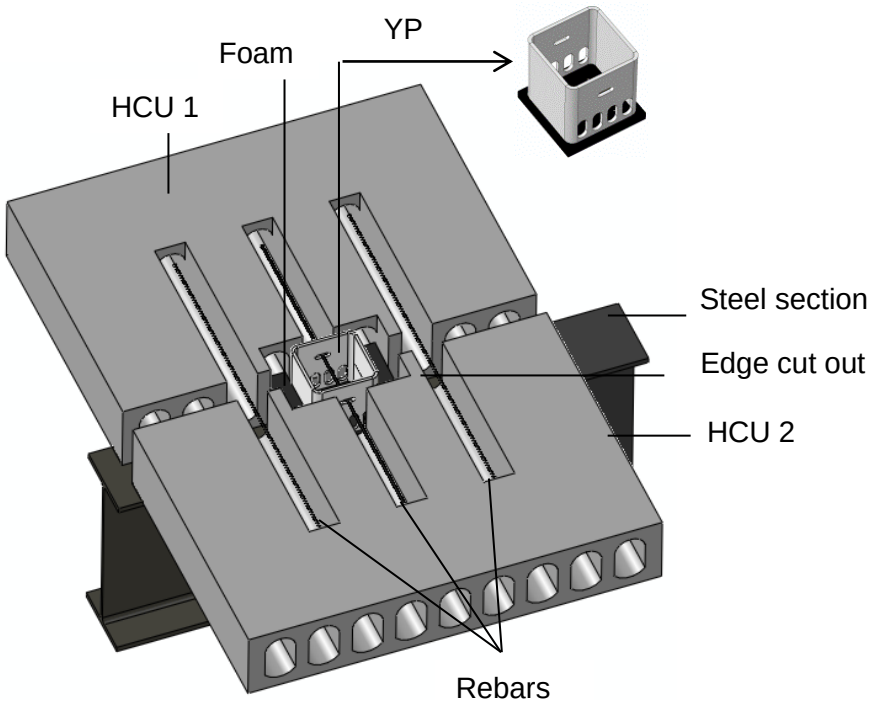

Figure 3.1 3D view of the proposed DSC

Figure 3.2 shows a longitudinal section of a composite beam. The YP is fixed on the top flange of the steel section using four high strength bolts. *In situ* concrete is poured to cover the open cores and the gaps between the YPs and the HCUs. Before pouring the *in situ* concrete, polythene foam is placed properly around the YP to keep the bottom part of the YP separated from the concrete and reduce the contact area between the concrete and the YP, as shown in Figure 3.2. By doing so, a ductile mode of failure due to yielding of the YP is promoted instead of a brittle shear failure of the bolts that would occur if the concrete was in full contact with the YP. The expected deformed shape of the YP is shown in the inset of Figure 3.2. The longitudinal shear force resultant is moved above the base of the YP and is resisted by the bending of the vertical steel strips and walls of the YP that are perpendicular to the direction of the steel section. To allow for the above plastic shear-resisting mechanism to develop, potential damage of any other steel part of the connection and concrete failure should be prevented.

The construction procedure of the proposed system consists of the following steps: a) The HCUs are positioned on the steel beams; b) the YPs are then fixed on the top flange of the steel sections using the four high-strength bolts; c) the rebars are placed in the open cores and polythene foam is placed around the YPs; and d) *in situ* concrete is poured to cover the open cores and the gaps between the YPs and the HCUs.

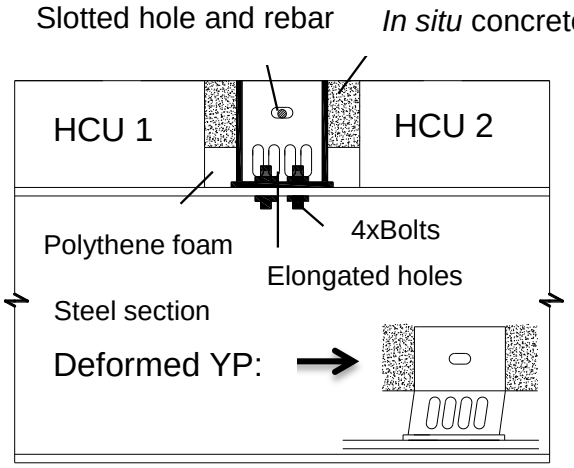

Figure 3.2 Longitudinal section of the proposed DSC

The deconstruction procedure consists of the following steps: a) the small area of concrete around the YP is removed, e.g. by using concrete cutting blades; b) the rebar passing though the YP is cut; c) the bolts are untightened and the YPs are removed. This procedure is achieved working only from the top side of the steel section (this is elaborated further in paragraph 4.2 of chapter 2); d) the slabs are removed; and e) all the steel structural components can be reused for the construction of a new building or including proper modifications to suit other buildings' geometry.

The proposed demountable steel yielding shear connector used in conjunction with HCUs has the following unique characteristics: a) it is not fully embedded thus the deconstruction procedure is facilitated by working from the top side of the steel section only; b) the shape of the shear connector promotes a ductile and predictable force-slip behaviour; c) the large shape of the shear connector distributes the shear force in a large area into the concrete component avoiding the development of high stress concentration that could potentially cause cracks and therefore concrete is less prone to damages as opposing to the welded headed studs; and d) strength and stiffness can vary depending on the selected geometry.

3.3 Plastic Steel -Yielding Mechanism of the Proposed DSC Connection

Figure 3.3 shows the geometric characteristics of the YP, which are the width of the steel strips, w, the height of the steel strips, h, and the thickness of the SHS tube, t. The foam around the YP is placed in such way that a concrete tooth is formed as shown in Figure 3.3a). The bottom fibres of the concrete tooth are in line with the top end of the vertical strips. Figure 3.3b) shows a plan view of a YP indicating the vertical walls as hatched regions. Under the longitudinal bending of a composite beam, the YP is

deformed under displacement, Δ, imposed by the concrete tooth as shown in Figure 3.4. The resistance of the YP is therefore provided by the bending of the steel strips and vertical walls. Assuming fixed boundary conditions, the vertical strips are expected to develop two plastic hinges at both ends of the height h_1 within which the width of the steel strips is minimum, as shown in Figure 3.4a). The forces developed due to the displacement imposed are shown in Figure 3.4b). The plastic moment of resistance of one steel strip section assuming rectangular cross section is given by:

$$M_{p,strip} = f_y \frac{t\, w^2}{4} \tag{1}$$

, where f_y is the yield strength of the YP's material, t is the thickness of the YP and w is the width of the steel strips. Based on plastic analysis principles, the shear strength provided by the steel strips is given by:

$$F_{p,strips} = 2\, F_{p,strip} = 2\, \frac{2\, M_{p,strip}}{h_1}\, n \tag{2}$$

, where n is the total number of the YP's steel strips per side.

Similarly, the vertical walls are expected to develop plastic hinges at both ends of the height h. The plastic moment resistance of one transverse vertical wall is calculated using plastic analysis of the cross section shown in Figure 3.5. The plastic neutral axis of the cross section is denoted as PNA in Figure 3.5. The plastic moment resistance of one transverse wall is given by:

$$M_{p,wall} = \frac{1}{2} f_y\, A\, Z_p \tag{3}$$

, where A is the cross section area and Z_p is the lever arm. Thus, the strength provided by the vertical walls is given by:

$$F_{p,walls} = 2\,F_{p,wall} = \frac{4\,M_{p,wall}}{h} \quad (4)$$

Thus, the total shear resistance, F_p, provided by the YP is:

$$F_p = F_{p,strips} + F_{p,walls} \quad (5)$$

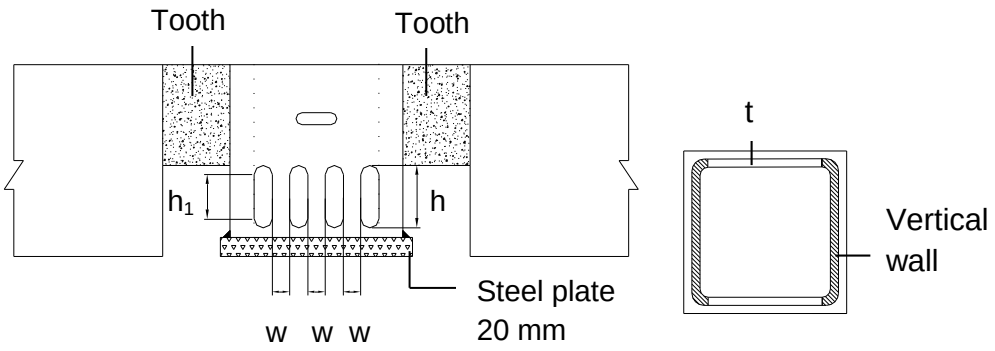

Figure 3.3 a) Geometrical characteristics of the steel yielding mechanism; and b) plan view of a YP showing the vertical wall's section

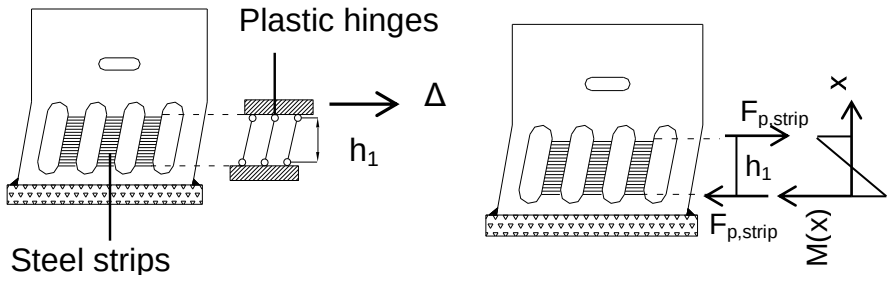

Figure 3.4 a) Steel strips' plastic yielding mechanism; and b) forces at the ends of a steel strip

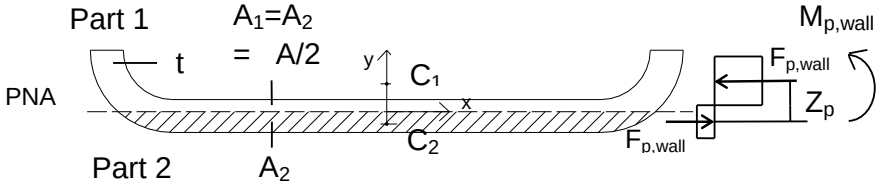

Figure 3.5 Plastic analysis of a YP's vertical wall

The theoretical stiffness provided by the steel strips is given by:

$$k_{strips} = \frac{12\ E_s\ I_{strips}}{{h_1}^3}\ n \tag{6}$$

, where I_{strips} is the second moment of area of the steel strips per side. The top end displacement of the steel strip is given by:

$$D_{p,strip} = \frac{F_{p,strips}}{k_{strips}} \tag{7}$$

Similarly, the stiffness provided by the two transverse walls is given by:

$$k_{walls} = \frac{12\ E_s\ I_{walls}}{h^3} \tag{8}$$

, where I_{walls} is the second moment of area of the two transverse walls. The top end displacement of the transverse wall is given by:

$$D_{p,wall} = \frac{F_{p,walls}}{k_{walls}} \tag{9}$$

The total stiffness of the YP is the sum of the products k_{strips} and k_{walls}. Therefore,

$$k = \frac{12\ E\ I_{strips}}{{h_1}^3} n + \frac{12\ E\ I_{walls}}{h^3} \tag{10}$$

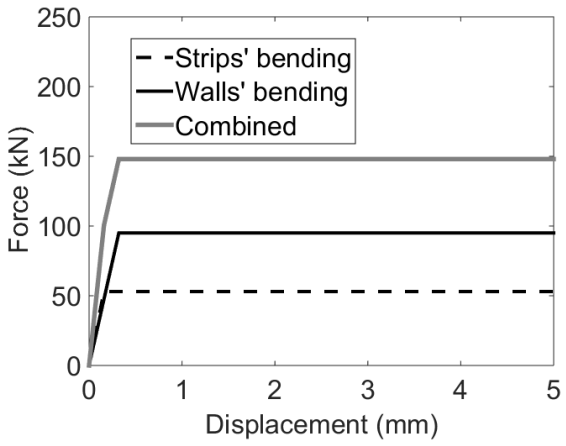

Figure 3.6 Theoretical force-displacement behaviour

A theoretical force-displacement behaviour is given in Figure 3.6 by substituting w=17 mm, h=75 mm, t=8 mm, f_y=390 N/mm^2 and E=208000 N/mm^2 in equations (1)-(10). The plastic neutral axis of a YP's vertical wall is determined by a repetitive trial-and-error procedure. The plot is given in order to show that since the steel strips' plastic yielding mechanism enter to the plastic region faster than the one of the vertical walls, the theoretical combined force-displacement curve of the YP under the assumptions made above is a trilinear curve.

3.4 Capacity Calculations for Steel Parts

The shear strength of the bolts, the bearing resistance of the connected plates at the bolt holes and the size of the weld at the bottom of the YP should be overdesigned to withstand the force and the moments applied, as shown in Figure 3.7. It is noted that since no experimental tests were performed to obtain the actual material properties of these steel parts, the design equations adopted by Eurocode 3 [3.1] and presented in this paragraph were used in order to select the dimensions of these steel parts and therefore to avoid premature steel failures during the tests. It was assumed that the steel parts should have at least double the yield strength provided by the YP to avoid steel failures in tests. The numerical results are given in the following chapter. The steel plate welded at the bottom of the YP is chosen to be thick enough to avoid premature failure, i.e. 20 mm. The bending moment shown in Figure 3.7 is carried by the system composed of: the bolts, the steel plate welded at the bottom of YP and the top flange of the steel section. The friction force developed between the steel section and the HCUs and between the steel section and the welded plate of YP after tightening of the bolts is neglected since it is very small.

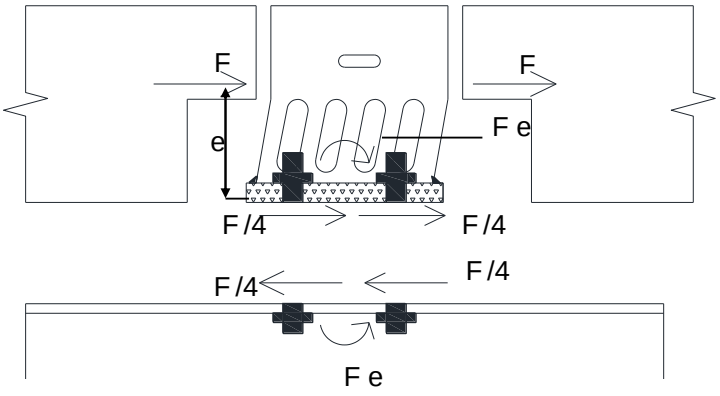

Figure 3.7 Forces and moments applied

3.4.1 Shear Strength of the Bolts

Four high strength bolts are used to connect the YP to the top flange of the steel section. The connection of the steel plate welded at the bottom of the YP to the steel section may be considered as bearing type. The threads of the bolts are outside the shear plane. Tight construction tolerances are considered up to 1 mm between the bolt diameter and the drilled holes of the top flange of the steel section. The shear resistance of the bolts is calculated according to Eurocode 3 [3.1] for bearing type steel connections. The shear strength is given by:

$$F_{v,Rd} = \frac{a_v \, f_{ub} \, \pi d^2}{\gamma_{M2} 4} m \, n \qquad (11)$$

, where f_{ub} is the ultimate strength of the bolts' material, d is the diameter of the bolts, m is the number of the bolts used equal to 4, n is the number of the shear planes equal to 2, α_v is a coefficient equal to 0.6 for 4.6, 5.6 and 8.8 steel grade and equal to 0.5 for 10.9 steel grade and γ_{M2} is safety factor equal to 1.25.

3.4.2 Bearing Resistance of the Connected Steel Plates

The bearing resistance of the connected steel plates at the bolt holes is checked following the procedure described in part 1-8 of Eurocode 3 [3.1]. Thus, the design bearing resistance is calculated herein. The connected steel plates are composed of the steel plate welded at the bottom of YP and the steel section's top flange. The thickness of the steel plate welded at the bottom of the YP is chosen thick enough, i.e. 20 mm, so as to prevent potential bearing failure. The thickness of the steel section's flange is normally less than 20 mm considering typical dimensions of steel concrete composite beams under usual dead and live loads. The bearing resistance of the connected plates at the bolt holes is given by:

$$F_{b,Rd} = \frac{2.5 \, a_b \, f_u \, d \, t_f}{\gamma_{M2}} \, m \qquad (12)$$

, where f_u is the minimum ultimate tensile strength between the two connected steel plates, t_f is the thickness of the steel section's flange, d is the diameter of the bolts, m is the number of the bolts used equal to 4, γ_{M2} is the safety factor equal to 1.25 and α_b is a

factor taking into account the influence of the edge distance and spacing between the bolts on the shear resistance, given by:

$$a_b = min\left(\frac{e_1}{3d_0}; \frac{p_1}{3d_0} - \frac{1}{4}; \frac{f_{ub}}{f_u}; 1\right) \quad (13)$$

, where e_1 and p_1 are the edge distance and spacing respectively in the direction of the load transfer, d_0 is the diameter of the drilled holes and f_{ub} is the ultimate tensile strength of the bolts. Figure 3.8 shows the plan view of the connection of the YP to the steel section.

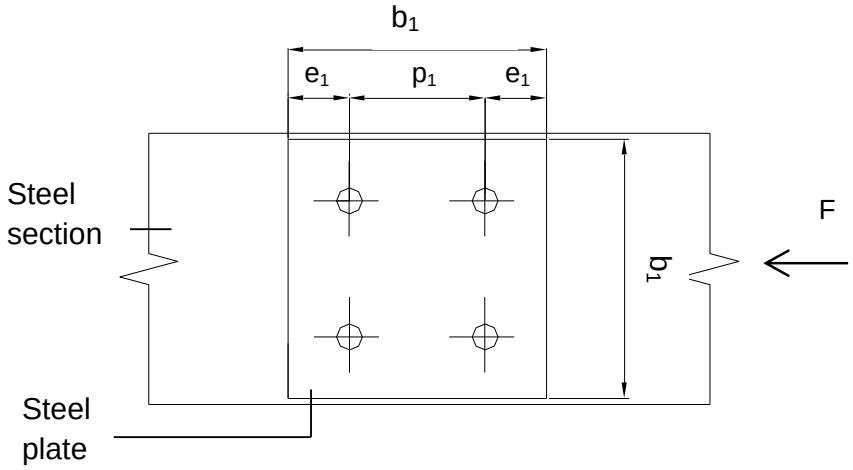

Figure 3.8 Plan view of the connected steel plates

3.4.3 Weld Size

The resistance of the weld is checked according to part 1-8 of Eurocode 3 [3.1]. The weld is subjected to combined shear and normal stresses due to the force F and due to the secondary bending moment equal to F e respectively as shown in Figure 3.7. Figure 3.9 shows the geometric characteristics needed to perform the resistance check. All around weld of 'α' throat thickness is used to connect the steel plate with the SHS tube of b width. The point 'Point 1' indicated in Figure 3.9 is checked under the combined action of shear and normal stresses positioned at a distance z_{max} from the gravity centre of the weld O.

The second moment of area of the weld about y-y axis is given by:

$$I_{y,w} = 2\frac{1}{12} a\, b^3 + 2\, b\, a\, \left(\frac{b}{2}\right)^2 \quad (14)$$

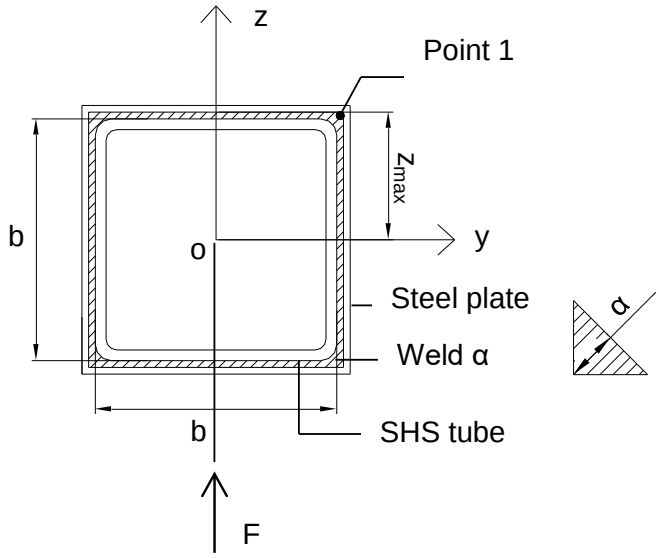

Figure 3.9 Weld resistance check

The area of the weld resisting the force F is given by:

$$A_w = 2\ a\ b \tag{15}$$

The shear stress parallel to the axis of the weld at the critical point 'Point 1' is given by:

$$\tau_2 = \frac{F_p}{A_w} \tag{16}$$

The normal stress perpendicular to the axis of the weld at the critical point 'Point 1' is given by:

$$\sigma_R = \frac{M}{I} z_{max} \tag{17}$$

, where M is the secondary bending moment equal to F e and z_{max} is the distance between the critical point and the centre O.

The normal stress perpendicular to the weld throat at the critical point 'Point 1' is given by:

$$\sigma_1 = \tau_1 = \frac{\sigma_R}{\sqrt{2}} \tag{18}$$

, where τ_1 is the shear stress perpendicular to the axis of the weld. Figure 3.10 shows the stresses applied on the weld. The vector of the shear stress τ_2 is on the plane of the paper thus is not shown in Figure 3.10.

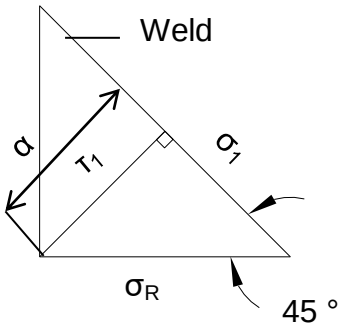

Figure 3.10 Stresses applied on the weld

The design resistance of the weld under the combined shear and normal stress at the critical point 'Point 1' is limited according to:

$$\sqrt{{\sigma_1}^2 + 3\,(\tau_1^2 + \tau_2^2)} \leq \frac{f_u}{\beta_w\,\gamma_{M2}} \tag{19}$$

,where f_u is taken equal to the ultimate strength of the weaker of the two connected steel plates, β_w is a correlation factor depending on the steel grade and γ_{M2} is safety factor equal to 1.25.

3.5 Strength Predictions of Concrete Component

Conventional welded headed studs are steel dowels embedded in concrete which transfer concentrated force into the concrete component and thus causing concrete damages [3.2]. Potential concrete damages of a steel dowel embedded in concrete caused by the dispersals of the concentrated force include transverse splitting, shear cracking and ripping. Ripping is considered to be of secondary importance since does not affect the shear transfer mechanism. Methods for predicting the ripping are covered in [3.3]. Figure 3.11 shows a plan view of a concrete slab indicating the potential failure modes of the DSC proposed in correspondence with the failure modes of steel dowels mentioned in [3.2]. The YP transfers distributed force, F_c, into the concrete component; the dispersals of the force, F_c, can cause concrete cracks as indicated in Figure 3.11. An additional potential failure mode is the crushing of the concrete tooth showing in Figure 3.12 under direct compression. The concrete slab of the DSC proposed is composite and consists of two concretes: the HCUs and the *in situ* concrete casted. The compressive and tensile strength of the weaker of the two concrete

components will be used in the numerical calculations for the prediction of the splitting and shear resistance.

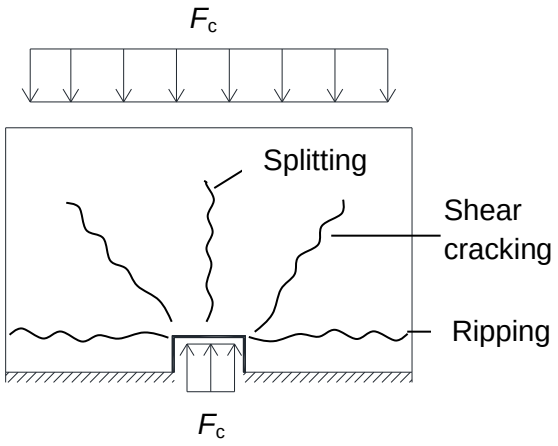

Figure 3.11 Potential failure modes of the DSC proposed (rebars not shown)

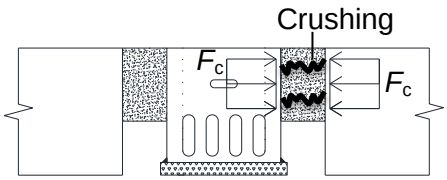

Figure 3.12 Potential crushing of the concrete tooth

3.5.1 Predictions for Splitting Resistance

The splitting resistance is estimated considering the strength of concrete prisms subjected to external patch and surface loads. It has been shown [3.3] that the bearing strength of concrete prisms (this is the load applied on the bearing area causing splitting of the prism) subjected to this type of loading is affected by a number of variables such as the size of the concrete prisms, the dimensions of the bearing area, the dimensions of the loaded area, the relative height of the prism defined as the ratio of the height to the width of the prism, the strength of the concrete, the area of reinforcement, if used, and the restraint conditions of the prism' base during the application of the load. Figure 3.13 a) shows the plan view of a concrete prism subjected to a concentric surface load. The loaded area is of width b_c and height h_c and the bearing area is of width b_α and height h_α. Figure 3.13 b) shows the side view of the concrete prism of height L.

Based on extensive experiments performed by Niyogi [3.4] on unreinforced and reinforced concrete prisms of medium concrete strength subjected to a number of variables, it was showed that in general the bearing resistance of the prisms decreases

when the height L of the prisms increases. This was partially attributed to the introduction of frictional restraints at the base of the short prisms which resulted in increase of their ultimate load.

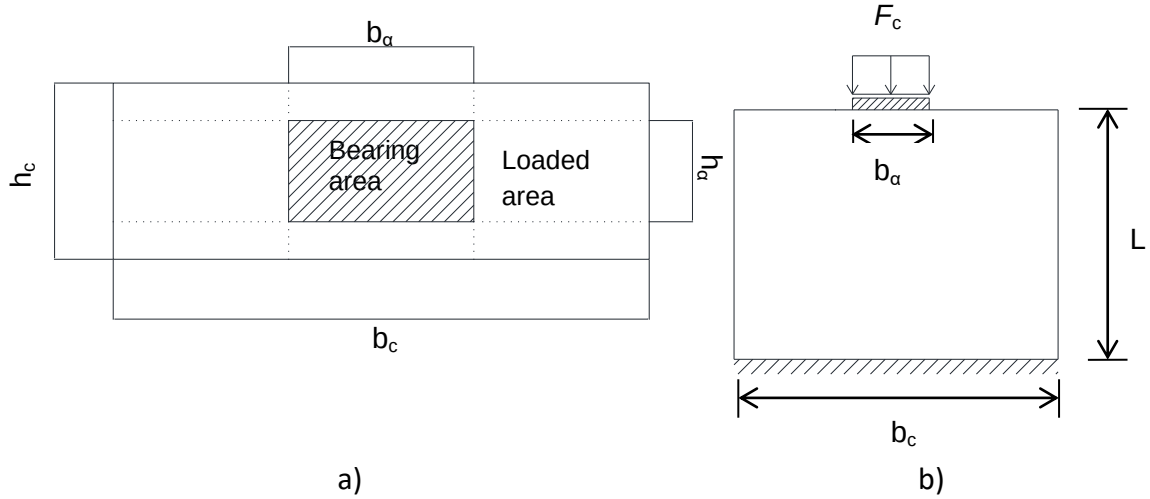

Figure 3.13 a) Plan; and b) side view of a concrete prism subjected to concentric rectangular surface load

The experimental results of Niyogi [3.4] were later verified by supplementary tests conducted by Williams [3.5] and regression analyses of the available experimental data taken from the previous two researchers by Oehlers and Johnson [3.6]. Indicatively, a short unreinforced concrete prism of L/b_c equal to 0.5 with b_c/b_α equal to 5 has an ultimate bearing resistance of around 1.8 f_c in terms of N/mm^2 or 1.8 f_c b_α h_α in terms of N, while a tall unreinforced concrete prism with L/b_c equal to 3 having an identical b_c/b_α ratio has an ultimate bearing resistance of around 1 f_c b_α h_α in terms of N. Therefore, the ultimate bearing resistance of the short concrete prism is equal to 1800 kN and the ultimate bearing resistance of the tall one is equal to 1000 kN taking into account a normal concrete strength of 25 N/mm^2 and size of bearing area 200x200 mm. The values given above for the bearing resistance of the concrete prisms were extracted from the diagram shown in Figure 3.14 [3.4]. The horizontal axis of the diagram shown in Figure 3.14 and denoted as $h/2\alpha$ corresponds to the height of the concrete prism divided to the width of the loaded area. The vertical axis of the diagram shown in Figure 3.14 corresponds to the ratio of the bearing resistance to the uniaxial compressive strength of the concrete. Each curve given in Figure 3.14 corresponds to the ratio of the width of the loaded area to the width of the bearing area. It is noted that this is the ultimate bearing resistance and not the force at which the first splitting crack appears in tests.

The bearing resistance of the two concrete prisms are given indicatively to show the order of magnitude. The results are given to illustrate why it is not expected to have a splitting failure in the push out specimens tested in the present thesis as will be proved in chapter 6. It is additionally noted that the adoption of this theory to control the splitting strength of the slabs of the push out specimens tested in the present study is limited to the specific geometry of specimens including an individual shear connector and does not cover the case of a potential 'global splitting' of specimens including two or more shear connectors in a row.

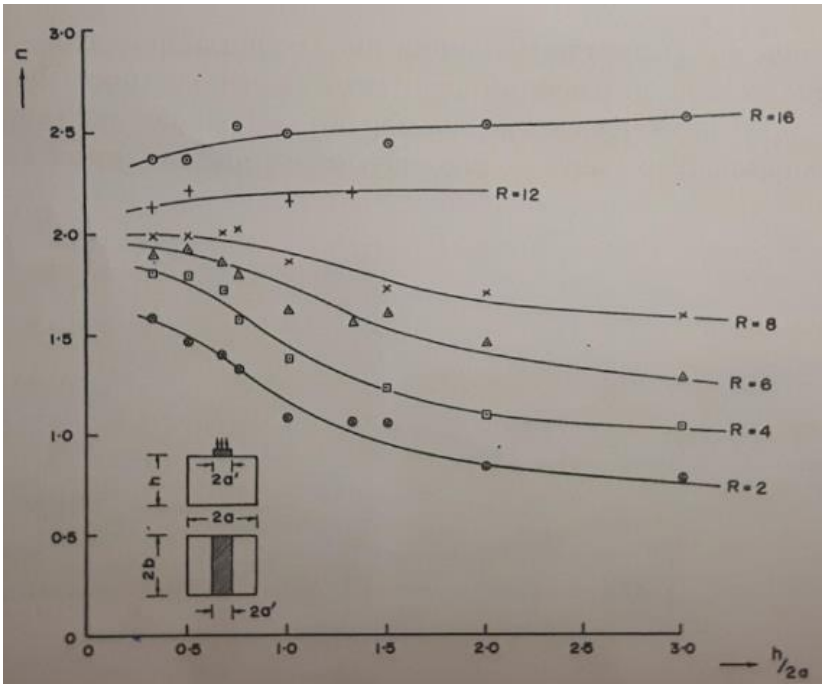

Figure 3.14 Diagram for the bearing resistance of concrete prisms [3.4]

The diagram shown in Figure 3.15 is an alternative to estimate the bearing resistance of concrete prisms subjected to surface loads. The diagram gives safe bearing pressures denoted as P_α associated with the compressive strength of the concrete. The diagram includes both cases of uncracked unreinforced concrete and reinforced cracked concrete using reinforcement ratios ω. To understand how the diagram works the simple case of a concrete prism with identical loaded and bearing area ($b_c=b_\alpha$) is first examined. It is b_c/b_α equal to 1 or b/α equal to 1, according to the notation of Figure 3.15, and this case can be considered equivalent to the uniaxial compression of a concrete cylinder resulting in bearing pressures equal to the uniaxial compressive strength of concrete. This practically means that there is no transverse tensile resultant to reduce the uniaxial compressive strength of the concrete prism. In all other cases and depending on the

geometric characteristics of the prism and the reinforcement ratio, if rebars are placed, the uniaxial compressive strength of the prism is reduced apart from the case that tri-axial conditions are developed (when relatively dense reinforcement lay out is placed). According to the diagram showing in Figure 3.15 and considering the material and geometric characteristics of the short concrete prism previously given as an example, the bearing resistance of the unreinforced prism considering uncracked concrete is 700 kN. If cracked concrete is assumed instead with a relatively low reinforcement ratio, i.e. ω equal to 0.04, the bearing strength is conservatively estimated around 520 kN. In conclusion, the short concrete prisms which are under concern in the present research work are considered to have adequate bearing resistance and therefore are not susceptible to splitting failure. The examples given above for the splitting resistance of the concrete prisms correspond to the geometric and material properties of the specimens' slabs used in the present study.

Neville [3.8] dealt with the subject of the influence of end restraints on the concrete strength of cylindrical and cubic concrete specimens. The same principles may be applied on concrete prisms. According to [3.8] frictional restrains developed at the ends of the concrete or cubic specimens emanated from the medium used to transfer the load during test or the surface of the tested specimens, e.g. rough. The friction developed at the ends of the concrete specimens during testing affects the concrete strength of the specimens by delaying the failure. Based on experimental results, the influence of the frictional restrains at the specimens' ends is higher when the ratio h/d decreases, where h is the height of the specimen and d its diameter, if cylindrical specimens are used.

This is the reason why the height of a standard cylinder subjected to compression should be two times its diameter in order to avoid the end restraints' effect. Oehlers and Johnson in [3.6] referring to concrete prisms came to a similar conclusion. They mentioned that the strength of the short concrete prisms tested by Niyogi [3.4] was influenced by the frictional restrains developed at the ends of the specimens and this is why the short specimens presented increased strength compared to the taller ones. They concluded that the end restraints' effect is avoided when the height of the concrete prism is three times its width.

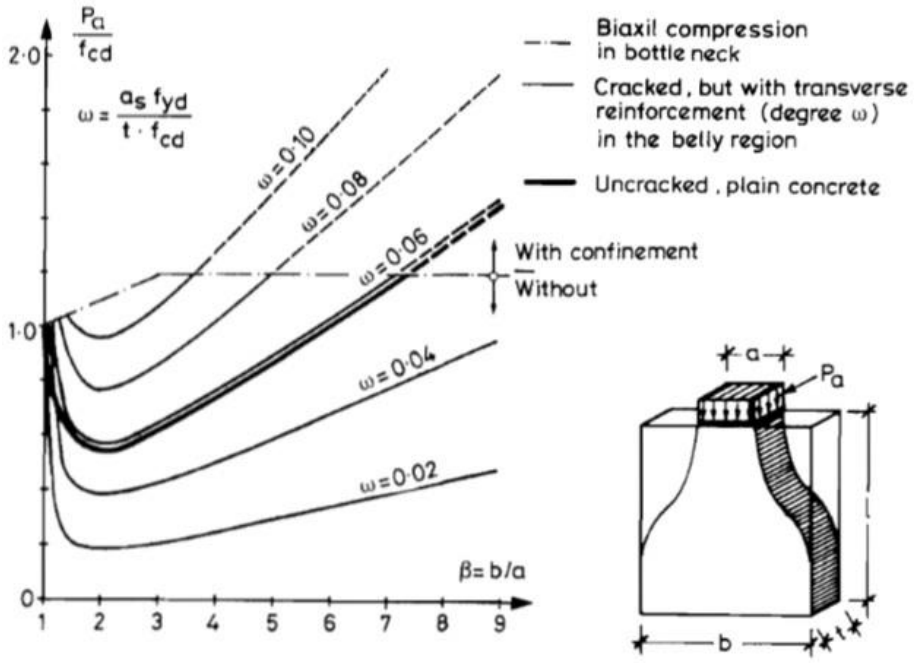

Figure 3.15 Safe bearing pressures of concrete prisms subjected to transverse stress field [3.7]

3.5.2 Predictions for Shear Resistance

The strength of the concrete component is predicted based on the well- established shear- friction theory applied across a crack firstly introduced by Birkeland and Birkeland [3.9]. The theory can describe the shear transfer mechanism across interfaces casted at different times and along cracked planes in reinforced concrete members. The mechanism is activated when sliding across the failure plane occurs. The roughness of the plane causes vertical separation which is resisted by the reinforcement crossing the interface. The widening of the crack is restrained by the axial stiffness of the rebars which stretch and develop tensile stresses. The tensile stresses developed in the rebars are balanced by compressive normal stresses acting on the failure plane. Therefore, the concrete elements found on either side of the failure plane are clamped together. The mechanism described is known as aggregate interlocking.

According to fib Model Code 2010 [3.10], the shear strength across a failure plane is emanated from the contribution of three components which are the adhesive bonding and mechanical interlocking, the shear friction and the bending resistance of the reinforcement crossing the plane, often known as dowel action. The adhesion and mechanical interlocking is often expressed in terms of the concrete tensile strength.

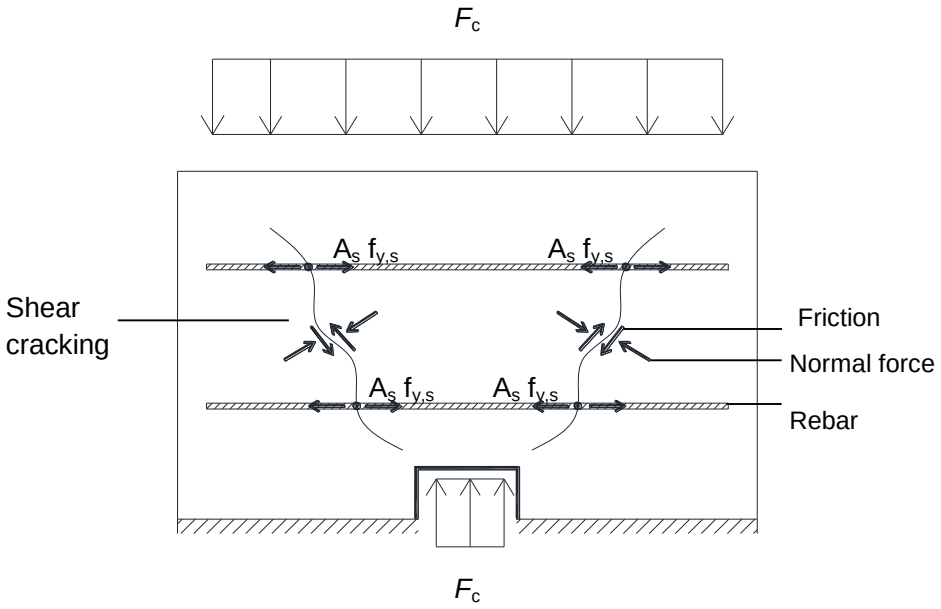

Figure 3.16 Mechanism of shear transfer across a crack

There are a number of shear friction models available in existing literature. A number of empirical equations have been developed and adopted by many national standards and codes in similar forms including the fib Model Code 2010 for concrete structures [3.10] and fib Model Code 2008 for structural connections for precast concrete buildings [3.11], Eurocode 2 [3.12], ACI 318 [3.13] and CAN/CSA A23.3 [3.14]. The theory of shear transfer across a cracked plane leads to a conservative design. The shear transfer through uncracked concrete is based on a truss system composed of compressive and tensile struts provided by the concrete and the rebars [3.15].

The conventional headed studs used in combination with *in situ* concrete slabs utilize the shear friction model proposed by Mattock and Hawkins [3.15] to describe the shear transfer across a cracked plane. However, this model is not suitable when slabs of larger than 200 mm total depth are used. This is because their research work was based on a specific range of compressive normal stresses to the failure plane which led to a lower bound limitation of the equations proposed in order the shear transfer mechanism to be activated. Since the reinforcement layout is fixed when HCUs are used, i.e. the spacing between adjacent rebars is around 240 mm placed in alternate cores, the theoretical normal pressure developed along the failure plane is less than the one required in [3.15]. Therefore, although the proposed shear–friction model is among the milestone ones in the historic development of those models, it is not suitable for the specimens tested in the present research work.

The shear–friction model proposed in fib Model Code for structural connections for precast concrete buildings [3.11] and in Eurocode 2 [3.12] is employed to describe the shear transfer through a hypothetical full depth cracked shear plane. The dowel action of the rebars is not taken into account, thus the shear strength across a crack is emanated from adhesion, mechanical interlocking and friction. Figure 3.16 shows the basic mechanism of shear-friction theory across a diagonal crack. The shear strength of a cracked shear plane is given in terms of N/mm^2 by:

$$v_u = c\, f_t \, + \, \mu\rho f_{y,s} k_r \leq 0.5 f_c \tag{20}$$

, or it is given in terms of kN by:

$$F_c = c\, f_t \, A_c + \, \mu A_s f_{y,s} k_r \leq 0.5 f_c A_c \tag{21}$$

, where f_t is the minimum concrete tensile strength between the HCU and the *in situ* concrete, A_c is the area of the assumed shear plane, A_s is the area of the reinforcement, $f_{y,s}$ is the yield stress of the rebars, ρ is the percentage steel ratio, k_r is a reduction factor to account for reduced anchorage or reduced stress development in rebars taken equal to 0.5 [3.10] and c and μ are cohesion and friction coefficients taken equal to 0.50 and 0.90 respectively according to [3.12].

The introduction of the factor k_r to account for the reduced stress development in the rebars represents more realistically the shear transfer mechanism because the rebars do not yield as will be shown in chapters 5 and 6 and therefore equation (21) produces a more conservative solution.

3.5.3 Direct Compression of Concrete Tooth

It is assumed that the concrete tooth is subjected to direct uniform compression. Therefore the strength of the tooth under uniform compression is given by:

$$F_{tooth} = 0.85 A_{c,tooth} f_c \tag{22}$$

, where $A_{c,tooth}$ is the area of the concrete tooth in contact with the transverse wall of the YP and f_c is the average uniaxial compressive strength of the concrete.

3.6 Example of Composite Floor Construction Including the Proposed DSC

An indicative example of a composite floor construction including the proposed DSC is shown in Figure 3.17. The floor system consists of simply supported steel concrete composite beams of 12 m length placed every 7.5 m. The HCUs are of 200 mm depth and 1200 mm nominal width including nine cores, the edge cut out is of 300x70 mm size and the self- weight of the unit is taken equal to 3 kN/m^2 according to standard tables provided by the manufacturing companies, e.g. by Bison Ltd. [3.16]. The length of the infill joints is considered 500 mm and the effective width of the slab is considered equal to the total length of the joints extended to both sides plus the gap between the HCUs, as recommended in [3.17]. The gap between the HCUs is 70 mm and the effective width is equal to 1.07 m. The strength of the HCU is 45 N/mm^2 at 28 days according to the manufacturing company and the one of *in situ* concrete is considered equal to 28 N/mm^2 at 28 days. The steel sections used to form the composite floor are of IPE 550 series and S355 steel grade.

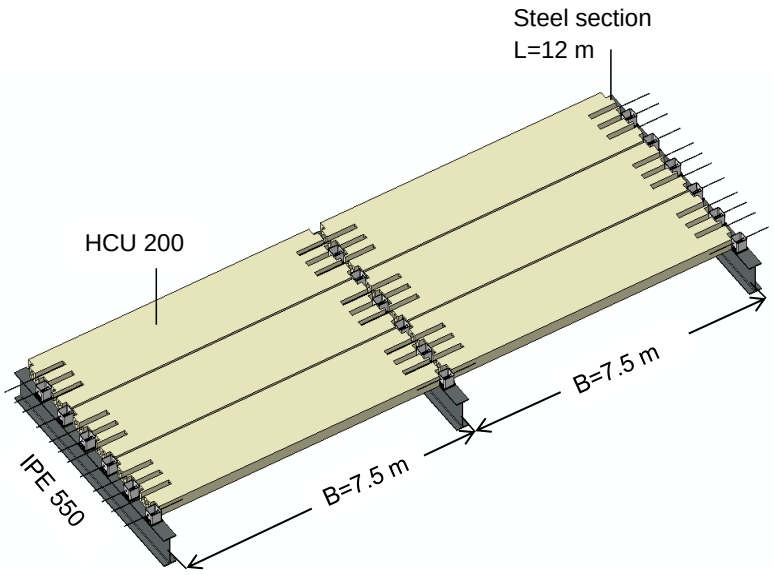

Figure 3.17 Indicative composite floor construction including the proposed DSC

The strength of each YP is considered equal to 300 kN. Table 3.1 gives the loads assumed for the ultimate design of the steel concrete composite section and the number of shear connectors required for full and partial shear connection. In case of full shear connection twenty four YP shear connectors are provided with a spacing of 600 mm. In case of partial shear connection and taking into account a degree of shear connection n=0.50, twelve shear connectors are provided with a spacing of 1000 mm. The spacings provided are only indicative.

Table 3.1 includes the number of welded headed studs required to achieve full and partial shear connection assuming the same design loads. Headed studs of 19 mm diameter are used and 120 mm long. The strength of each headed stud is 80 kN [3.17]. In case of full shear connection 42 headed studs are provided with a spacing of 145 mm. In case of partial shear connection 21 headed studs are provided with a spacing of 285 mm.

Loads		
Self- weight of HCUs w_{HCU}	(kN/m^2)	3.00
Self- weight of steel section w_{steel}	(kN/m)	1.06
Floor finishes q_{floor}	(kN/m^2)	1.00
Infill joints q_{joints}	(kN/m)	0.90
Live load q_{live}	(kN/m)	2.50
Ult. design of composite section		
Design load q_{sd}	(kN/m)	79
Design moment M_{sd}	(kN m)	1430
Tensile resistance of steel F_s	(kN)	4337
Compressive resistance of concrete F_c	(kN)	3355
Design for full shear connection		
Strength of connection F_{fsh}	(kN)	3355
Moment capacity $M_{Rd,fsc}$	(kN m)	1525
Strength of a YP shear connector F_{YP}	(kN)	300
Strength of a headed stud F_{stud}	(kN)	80
Total number of YP shear connectors $n_{YP,fsc}$		24
Total number of headed studs $n_{studs,fsc}$		42
Design for partial shear connection		
Degree of shear connection n		0.50
Strength of connection F_{psc}	(kN)	1680
Moment capacity $M_{Rd,psc}$	(kN m)	1171
Strength of a YP shear connector F_{YP}	(kN)	300
Strength of a headed stud F_{stud}	(kN)	80
Total number of YP shear connectors $n_{YP,psc}$		12
Total number of headed $n_{studs,psc}$		21

Table 3.1 Indicative example of composite floor construction

3.7 Reference List

[3.1] EN1993-1-8: Eurocode 3: Design of steel structures. Part 1-8: Design of joints. Brussels, Belgium: European Committee for Standardization (2005)

[3.2] D.J. Oehlers, M.A. Bradford, *Composite steel and concrete structural members: fundamental behaviour*, Elsevier Science Ltd, Oxford (1995)

[3.3] D.K. O'Brien, *Shear failure of diagonally cracked reinforced concrete beams by ripping of the concrete*, M.Sc. Thesis, University College, Cork, National University of Ireland (1986)

[3.4] S.K. Niyogi, *Bearing strength of concrete-geometric variations*, Proceedings of the American Society of Civil Engineers, 99(7), 1471-1490, July 1973

[3.5] A. Williams, *The bearing capacity of concrete loaded over a limited area*, Technical report 526 (Publication 42.526), Cement and Concrete Association, Wexham Springs, UK, 1979

[3.6] D.J. Oehlers, R.P. Johnson, *The splitting strength of concrete prisms subjected to surface strip or patch loads*, Magazine of Concrete Research, 33(116), 171-179 (1981)

[3.7] J. Schlaich, K. Schafer, M. Jennewein, *Toward a consistent design of structural concrete*, PCI Journal, 32 (3), 75-150, May-June 1987

[3.8] A.M. Neville, *Properties of concrete*, Pearson Educated Limited, Harlow (2002)

[3.9] P.W. Birkeland, H.W. Birkeland, *Connections in precast concrete construction*, ACI Struct. J., 63 (3), 345–68 (1966)

[3.10] fib Model Code 2010 for concrete structures, Comité Euro-International du Béton, Secretariat permanent, Case Postale 88, CH-1015 Lausanne, Switzerland, 180 (2010)

[3.11] fib Model Code 2008 Structural connections for precast concrete buildings. Comité Euro-International du Béton, Secretariat permanent, Case Postale 88, CH-1015 Lausanne, Switzerland, 255-256 (2008)

[3.12] EN 1992-1-1 - Eurocode 2 - Design of concrete structures - Part 1-1: General rules and rules for buildings, European Committee for Standardization (CEN), 92-93 (2004)

[3.13] ACI 318 - Building code requirements for structural concrete (ACI 318-08) and commentary, Committee 318, American Concrete Institute, PO Box 9094, Farmington Hills, MI 48333-9094, USA, 471 (2008)

[3.14] CAN/CSA A23.3. Design of concrete structures - Structures design. Canadian Standards Association, 178 Rexdale Boulevard, Rexdale, Ontario, M9W 1R3, Canada, 258 (2004)

[3.15] A.H. Mattock, N.M. Hawkins, *Shear transfer in reinforced concrete recent research*, Precast Concrete Institute Journal, March-April, 55-75 (1972)

[3.16] Retrieved from< http://www.bison.co.uk/pdf/bison-hollowcore-floors-load-span-table.pdf> (June 2018)

[3.17] G.H. Couchman, *Design of composite beams using precast concrete slabs in accordance with Eurocode 4*, SCI Publication P401 (2014)

Chapter 4-Experimental Program

4.1 Introduction

The experimental program consists of twelve push out tests performed using a horizontal test arrangement. The horizontal test arrangement, the testing procedure, the instrumentation, the geometric and material properties of the push out specimens and the test variables are described in the present chapter. The results of the strength predictions presented in chapter 3 including the yield strength of the DSC, the capacity calculations for the steel parts of the connection and the strength predictions for the concrete component are summarized.

4.2 Push out Specimens

A plan view and a longitudinal section of a typical push out specimen are shown in Figure 4.1 and Figure 4.2 respectively. The geometric dimensions of the specimens were selected based on the indicative steel concrete composite beam design presented in paragraph 3.6 of chapter 3. Each specimen consisted of two HCUs seated on a steel section of UB533x210x92 (equivalent to IPE550) and S355 steel grade using a single YP.

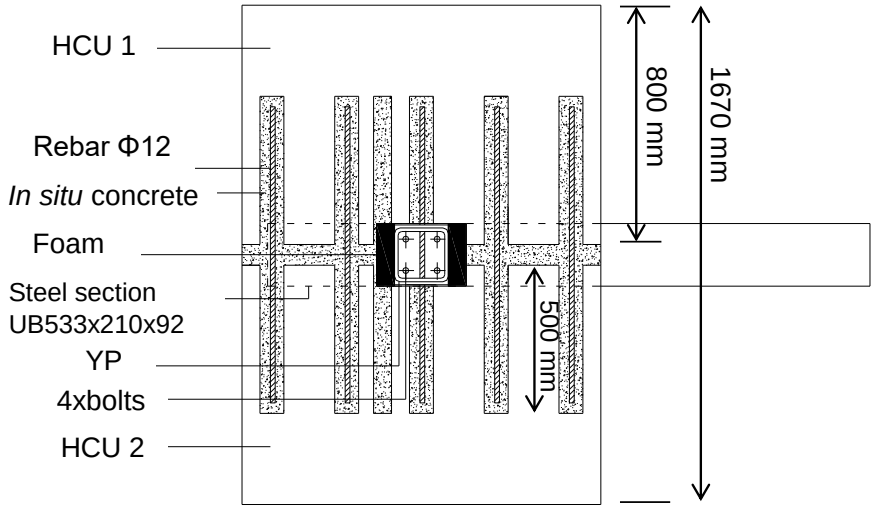

Figure 4.1 Plan view of a typical push out specimen

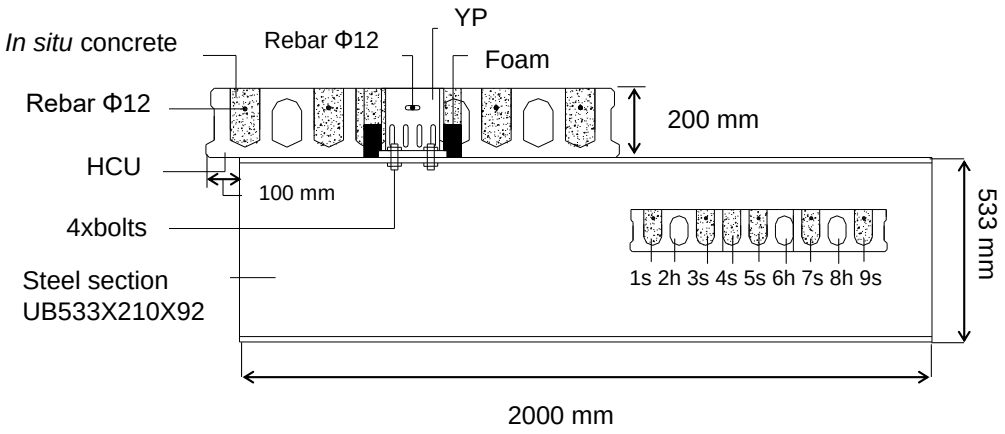

Figure 4.2 Longitudinal section of typical push out specimen

The HCUs used for all specimens were standard units of nine cores, 1200 mm nominal width, 800 mm length and 200 mm depth including an edge cut out which was placed in the middle position of the unit's width. The edge cut out was of 300 mm length in the direction parallel to the steel section's axis and 70 mm width in the direction perpendicular to the steel section's axis and it was cut through the depth of the slab. Each HCU included five open cores to serve the placement of transverse reinforcement, i.e. the cores 1, 3, 5, 7 and 9 shown in the inset of Figure 4.2. Polythene foam was placed in proper positions around the YP to form the concrete tooth before pouring the *in situ* concrete. The five open cores were filled with *in situ* concrete after the rebars of 12 mm diameter and S500 steel grade were placed in the cores.

The cores of the HCUs filled with *in situ* concrete and the ones remained hollow after casting are designated with the letter 's' and the letter 'h' respectively in the inset of Figure 4.2. Thus, the cores denoted as '1s', '3s', '4s', '5s', '7s' and '9s' were full of *in situ* concrete and the cores denoted as '2h', '6h' and '8h' remained hollow after casting for all the specimens apart from the first one tested. The 4^{th} core designated as '4s' was left open and was filled with *in situ* concrete to avoid premature shear cracking of the slab, based on the first test, in which the 4^{th} core of the HCUs was not casted with *in situ* concrete and remained hollow, and on equation (21) which requires the core located just before the YP in the direction of loading to be full of concrete for the transfer of shear stresses. Therefore, the concrete slabs of the first specimen tested differ from those of the subsequent ones in that the 4^{th} core of the first specimen remained hollow after casting. The HCUs were provided by Bison Precast Limited and the cube strength of the units at 28 days according to the manufacturing company was 55 N/mm^2. The data

sheet of the HCUs is available online in [4.1]. The tensile strength of each HCU at 28 days was estimated based on the prediction of BS EN 1992-1-1:2004 (p. 29) [4.2] and it is related to the characteristic compressive strength of the unit. The tensile strength of the HCUs was taken equal to 3.3 N/mm^2. Figures 4.3 and 4.4 show indicatively the open cores of the HCUs of the specimen SP2B and the polythene foams properly placed around the YPs before casting of the specimen SP3 respectively. Figure 4.5 shows indicatively the specimen SP3 after casting.

Figure 4.3 Open cores of HCUs (specimen SP2B)

Figure 4.4 Indicative position of foams around the YP (specimen SP3)

Figure 4.5 Specimen after casting (SP3)

Each YP was manufactured from structural hollow sections of SHS180x180x8 or SHS180x180x10 hollow tube of S355 J2H steel grade. The rectangular steel plate welded at the bottom of YP was of 200 mm width, 20 mm thickness and of S275 steel grade for all specimens. The weld size was 10 mm or the weld throat was 7 mm for all the YPs. The depth of the horizontal slotted hole of each YP was designed to allow the placement of a 12 mm diameter rebar with minimum tolerance. Figure 4.6 shows an indicative geometry of a YP including all the structural details.

Figure 4.6 An indicative geometry of a YP ready to be installed

Each YP was fixed on the top flange of the steel section using four high strength bolts. The initial concept included the use of innovative blind bolts offering the advantages of one side installation. The first two tests were designed to include the 'heavy duty' blind bolt shown in Figure 4.7 provided by the Blind Bolt Company. The blind bolts used were of M20X85 size and the ultimate shear strength of each bolt according to the manufacturing company was 128 kN. The data sheet of the blind bolts used is online available in [4.3]. The installation procedure of the blind bolts included the use of a

hammer to strike the pin at the head of the bolt until flush with the bold head, at which point the legs of the bolt were fully expanded and locked the connected steel elements together. Since the use of the blind bolts did not benefit the behaviour of the DSC proposed and led to premature failures of the concrete slab as will be shown in chapter 5, the initial concept was abandoned and high tensile strength allen bolts were used to fix the YP on the steel section in the following ten specimens.

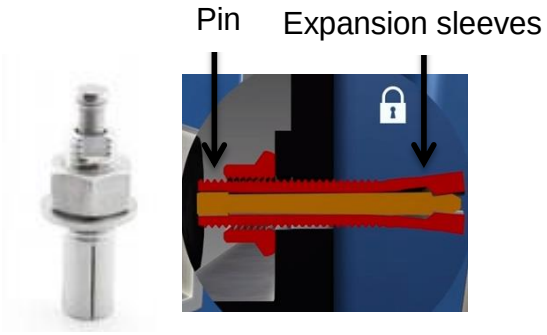

Figure 4.7 Initial concept using blind bolts to fix the YP on the steel section [4.4]

Each YP was fixed on the top flange of the steel section in the following ten specimens using four high tensile strength allen bolts of 20 mm nominal diameter and 12.9 steel grade. Washers and nuts were used. Figure 4.8 shows the allen bolts used. These bolts have hexagonal shaped head and were fastened using a proper allen wrench with hexagonal sockets. The bolts were tightened using the allen wrench to apply a 220 N m torque from the top side of the steel section where the nuts were placed, while a hex key was used at the same time from the bottom side of the steel section to resist the applied torque. Figure 4.9 shows the plan view of the connection of the YP to the top flange of the steel section. When it comes to deconstruct the system, the bolts can be easily disconnected from the steel section by working only from the top side; this includes untightening of the bolts with a wrench, removal of the washers and nuts and strike of the bolts using a hammer. The steel grade of the bolts was selected high enough to preclude any damage in the bolts.

Figure 4.8 Allen bolts used to fix the YP on the steel section

Figure 4.9 Plan view of the connection of the YP to the steel section (washers and nuts placed in the top side of the steel section)

4.3 Material Properties of the Push out Specimens

Concrete and steel material tests were performed. A number of concrete cubes and cylinders were casted and cured along the push out specimens at the day of testing to obtain the compressive and the splitting strength. A number of coupon specimens were taken from the SHS180x180x8 and SHS180x80x10 tubes and rebars to obtain various material properties.

4.3.1 Steel

The material properties of the YP were obtained from standard tensile coupon tests for sheet type according to ASTM E8/E8M specification [4.5]. Tensile coupon tests were taken from the flat and corner regions of the SHS180x180x8 and SHS180x180x10 tubes. Figure 4.10 shows the nominal dimensions of the coupon specimens extracted according to [4.5]. The gauge length of the flat and corner coupons were 50 mm. Figure 4.11 shows the specific regions from where the coupon specimens were extracted, denoted as 'F' and 'C' for the flat and corner coupons respectively. The tensile tests were performed using the 'Instron' tensile machine with a loading rate of 0.5 mm/min. The longitudinal strains were measured with pre-calibrated extensometers of 50 mm gauge length attached to the marked positions shown in Figure 4.10.

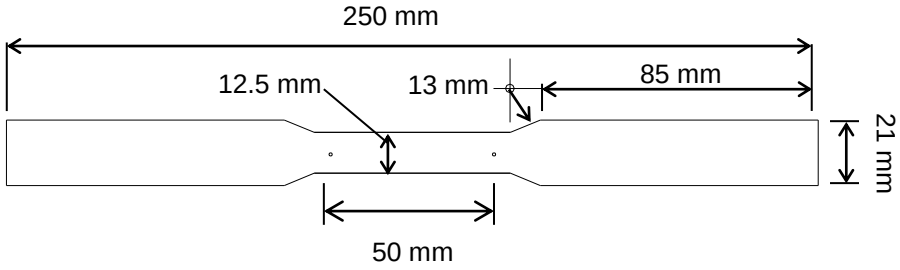

Figure 4.10 Standard nominal dimensions of coupon specimens according to ASTM [4.5]

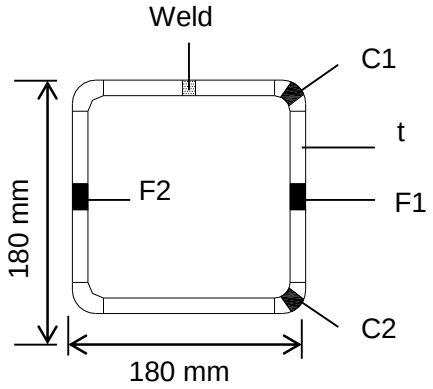

Figure 4.11 Regions of coupons extracted

The material properties obtained were the modulus of Elasticity, the 0.2 % proof stress, the ultimate strength and the tensile strain corresponding to the ultimate strength. Table 4.1 shows the material properties obtained from each coupon specimen and the average material properties per coupon specimen type ('F' or 'C'). The experimental force-displacement curves as automatically extracted from the tensile machine were converted to engineering stress-strain curves using the measured area of the cross section of the specimens. Figures 4.12 and 4.13 show the engineering stress-strain curves of the coupon specimens tested for the SHS180x180x8 and SHS180x180x10 hollow tube respectively.

The results showed that the corner coupons had higher modulus of Elasticity, yield and ultimate strength than the flat coupons, considering coupons taken from the same type of SHS tube. The strain at the ultimate strength was recorded much lower for the corner coupons compared to the flat ones. The reduced elongation recorded is a characteristic

of the behaviour of the corners of SHS and RHS tubes manufactured from cold formed steel [4.6].

Coupon specimen	Sample no.	Code	Cross section (mm^2)	Mod. of Elasticity (N/mm^2)	0.2% proof stress	Tensile strength (N/mm^2)	Strain at ult. strength
Flat region SHS 180x8	1	F1	97	187200	400	463	0.168
Flat region SHS 180x8	2	F2	95.6	200000	380	457	0.168
Flat region SHS180x8	Ave.		96.3	193600	390	460	0.168
Corner region SHS 180x8	1	C1	125	213000	410	450	0.023
Corner region SHS180x8	2	C1	112	221000	390	410	0.018
Corner region SHS180x8	3	C2	108	230000	380	410	0.017
Corner region SHS180x8	Ave.		115	221000	390	425	0.019
Flat region SHS180x10	1	F1	120.5	217800	490	563	0.080
Flat region SHS180 x10	2	F1	119.5	210000	510	573	0.089
Flat region SHS180x10	3	F2	122	180800	490	560	0.092
Flat region SHS180x10	Ave.		120.6	202850	500	565	0.087
Corner region SHS180x10	1	C1	145	226000	520	573	0.041
Corner region SHS180x10	2	C1	130	210000	550	630	0.024
Corner region SHS 180x10	3	C2	114	216000	520	575	0.024
Corner region SHS180x10	4	C2	107	224500	500	590	0.021
Corner region SHS180x10	Ave.		124	215500	525	590	0.028

Table 4.1 Material properties of SHS180x180 tubes

Initial longitudinal bending was observed after the extraction of the coupon specimens from the flat part of the tubes due to residual stresses related to the manufacture process of cold formed sections well documented in relevant literature review and investigated by a number of researchers, e.g. by Ingvarsson [4.6] and Weng and Pekoz [4.7]. However once the specimens were attached to the jaws of the testing machine and the jaws closed, the coupons flattened. Having observed this behaviour, Gardner and

Nethercot [4.8] concluded that the initial bending of the coupon specimens was re-introduced to the specimens when attached to the jaws and the residual stresses' influence can be considered as inherent property of the coupon specimens.

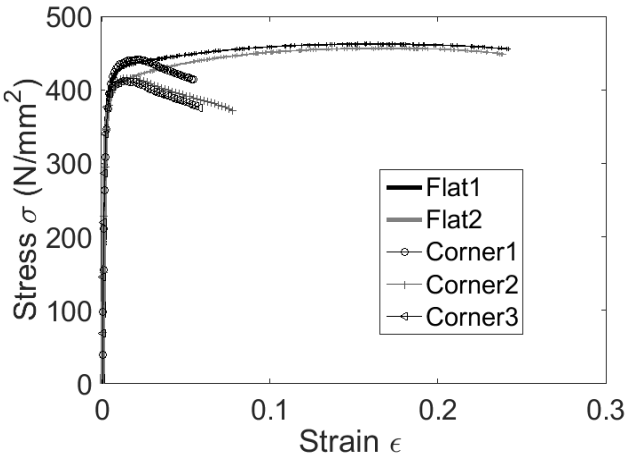

Figure 4.12 Stress-strain behaviour of coupons taken from SHS180x180x8 hollow section

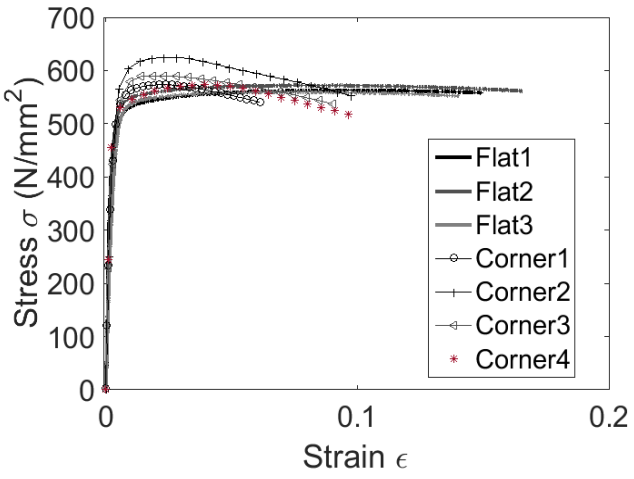

Figure 4.13 Stress-strain behaviour of coupons taken from SHS180x180x10 hollow section

Two round type coupon specimens were extracted from the rebars of 12 mm nominal diameter. The gauge length was 50 mm and proper pre-calibrated extensometers were attached to the specimens for the measurement of the longitudinal strains. The loading rate of the tests was 0.1 mm/min. The material properties obtained were the modulus of Elasticity and the tensile strength. Table 4.2 shows the material properties obtained for each coupon specimen and the averaged ones. The force-displacement curves which were automatically obtained from the tensile testing machine were converted to engineering stress-strain curves using the measured area of the cross section of the

rebars. The tensile test of rebar 2 stopped prematurely since only the modulus of Elasticity and the yield strength were required. Figure 4.14 shows the engineering stress-strain behaviour of rebar 1.

Coupon specimen	Cross section (mm^2)	Mod. of Elasticity (N/mm^2)	Tensile strength (N/mm^2)
1	10.23	207000	512
2	10.35	210000	490
Ave.	10.3	208500	500

Table 4.2 Material properties of the rebars

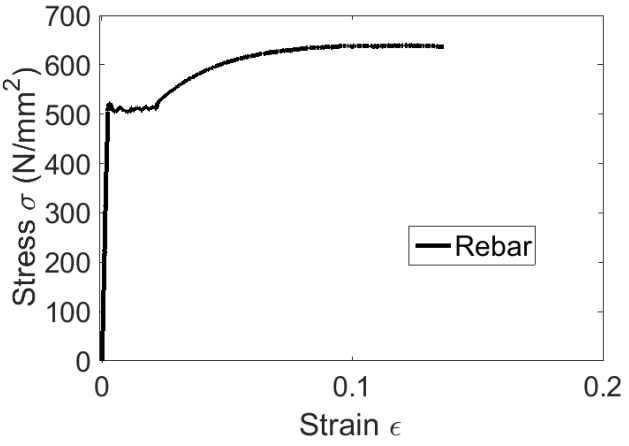

Figure 4.14 Stress-strain behaviour of rebar 1

4.3.2 Concrete

The *in situ* concrete used to fill the open cores of the HCUs and the gaps around the YP was prepared in the lab. High strength Portland cement of 52.5 strength (CEM I 52.5N) was used for the specimens requiring a compressive cube strength higher than 40 N/mm^2 at the testing day. Low strength Portland cement of 32.5 strength (CEM I 32.5 N) was used for the specimens requiring a compressive cube strength lower than 40 N/mm^2 at the testing day. The maximum aggregate size used in the concrete mix was 10 mm. Fine sand of less than 2 mm particles' size was used. The sand was always kept inside the lab for three days to control humidity. A polycarboxylate superplasticizer under the commercial name 'Master matrix 233' was used provided by BASF Company. A medium to high workability concrete was produced for each push out specimen around 70-100 mm slump. A number of slump tests were performed according to BS EN 12350-2:2009 [4.9] until a valid and optimum mix design was

achieved. Table 4.3 shows the final mix proportions for the *in situ* concrete poured in the push out specimens. Figure 4.15 shows the concrete cone after the removal of the steel cone for a slump test using the mix proportions indicated in Table 4.3. The compaction of the concrete was manual using a tamping steel rod of 16 mm and it was implemented in two layers of 100 mm depth for each layer.

Quantities in grams per 1lt	
Water	193.6
Cement	423
w/c	0.457
Fine sand	670
River aggregates	1095
Superplasticizer	5.5

Table 4.3 Mix proportions of in situ concrete used in specimens

Figure 4.15 Concrete cone after conducting slump test

The concrete cubes casted were of standard dimensions of 100x100x100 mm. The cubes were cured along the push out specimens to obtain the compressive strength of the concrete at the testing day. The compressive tests were performed according to BS EN 12390-3:2009 [4.10]. Three concrete compressive cube tests were performed for each push out specimen and the average value was determined. Standard cylinders of 100 mm diameter and 200 mm length were casted and cured along the push out specimens to obtain the splitting strength at the testing day.

The spitting tests were performed according to BS EN 12390-6:2009 [4.11]. Two splitting tests were performed for each push out specimen and the average value was determined. Table 4.4 summarizes the compressive and tensile splitting strength of the cubes and cylinders at the day of testing respectively. The push out specimens are designated with the prefix ‘SP’ followed by a number and a letter the meaning of those are explained in paragraph 4.4.

Specimen	Compressive cube strength (N/mm^2)					Splitting tensile strength (N/mm^2)		
	Test day	1	2	3	Ave.	1	2	Ave.
SP0A	38	67.8	70.2	68.8	69	4.3	5.1	4.7
SP0B	25	65.1	70	65.9	67	3.7	3.5	3.6
SP1A	27	62	63.4	58.5	61	4.1	4.5	4.3
SP1B	17	56.6	53	46.4	52	3.0	3.2	3.1
SP1C	14	53.10	48.6	50.8	50	2.8	3.0	2.9
SP2A	7	48.7	46.4	45	47	2.6	3.1	2.9
SP2B	17	59.5	55	53.5	56	3.5	3.7	3.6
SP3	12	38	37.2	37.8	38	2.4	2.7	2.5
SP4A	35	70.5	66	67.5	68	4.3	4.7	4.5
SP4B	14	45.9	49.3	45.8	47	2.5	3.10	2.8
SP5	10	34.4	34.6	35.7	35	1.9	2.3	2.1
SP6	12	27.5	31.5	31	30	2.2	1.6	1.9

Table 4.4 Material properties of *in situ* concrete

4.4 Design Parameters and Strength Predictions

The push out specimens are designated with the prefix 'SP' followed by a number which indicates a specific YP geometry group and a letter which indicates the number of tests performed with identical YP geometry. When there is no letter, only one test was conducted with the specific YP geometry. The parameters investigated in tests were the strength of the *in situ* concrete and the geometric characteristics of the YP. The test matrix summarizing the variables of the push out tests is given in Table 4.5 including the geometrical characteristics of the YPs tested and the equivalent cylindrical strength of the *in situ* concrete cubic samples tested, according to BS EN 1992-1-1:2004 [4.2]. This is taken approximately as 80% the strength of the concrete cubic samples. The aim of the first two tests designated as SP0A and SP0B in Table 4.6 was to collect useful information about the structural behaviour of the DSC proposed using innovative blind bolts. Since the use of these bolts was not beneficial in the structural response of the DSC proposed and they were not used in the following tests, the parameters investigated in tests and the strength predictions are primarily related to the specimens' group SP1 to SP6.

Table 4.5 shows the prediction of the yield strength of the YP, F_p, the shear resistance of the concrete component, F_c, and the resistance of the concrete tooth against crushing denoted as F_{tooth}.

The yield strength of the YP was calculated using equation (5) taking into account the measured material properties for the steel. The shear resistance of the concrete component was calculated using equation (21) taking into account a reinforcement ratio of 0.23% for all the specimens and cracked shear planes at both sides. Since equation (21) uses the tensile strength of the concrete, the splitting tensile strength of the *in situ* concrete obtained from the tests was converted to axial tensile strength using the relation proposed by BS EN 1992-1-1:2004 [4.2] taken as 0.9 $f_{t,split}$, where $f_{t,split}$ is the splitting tensile strength of the concrete. The crushing of the concrete tooth was calculated using equation (22) taking into account a contact area between the YP and the concrete tooth equal to 180 x (170-h) mm^2, where h is the height of the YP's steel strips. The splitting resistance of the push out specimens' slabs is not expected to be critical as it was explained in paragraph 3.4.1, where it was showed that a short concrete prism of 25 N/mm^2 concrete strength having identical geometric characteristics to the push out specimens' slabs used in the present tests conservatively have a splitting resistance of at least 520 kN.

According to the theoretical predictions, the level of yielding force expected in tests changes by altering the geometric characteristics of the YP. Six different YP geometries were tested. The specimens belonging to the groups SP1, SP2 and SP4 were designed to have *in situ* concrete strength of 38-54 N/mm^2 combined with a relatively low to medium yield strength YP between 150-263 kN. The specimen SP3 was designed to have normal *in situ* concrete strength of 30 N/mm^2 combined with medium yield strength YP of 215 kN. The specimen SP5 and SP6 were designed to have normal *in situ* concrete strength of 28 and 24 N/mm^2 respectively combined with high strength YP of 345 and 310 kN respectively. The ratio of the yield strength of YP to the shear strength of the concrete F_p/F_c is given in Table 4.5.

By inspection of the ratio values, it is reasonable to expect primarily failure due to YP yielding in specimens where the ratio is very low and involvement of concrete in the failure modes when the ratio increases above 1, as in specimens SP5 and SP6, taking into account the hardening behaviour of the YP. All the strength predictions for the concrete component need to be verified by the experimental results. Tables 4.6 and 4.7 summarize the results derived from the capacity calculations of the steel parts of the connection presented in paragraph 3.3 of chapter 3 which are identical for all tests.

Table 4.6 includes the ultimate design shear resistance of the bolts, $F_{v,Rd}$ and the design bearing resistance at the bolt holes, $F_{b,Rd}$, using equations (11) and (12) respectively. The design tensile yield and ultimate strengths related to the specific steel grade of each steel part provided by the manufacturing companies were used in equations (11) and (12).

Specimen	YP geometry			Eq. concrete cylinder strength (N/mm^2)	F_p (kN)	F_c (kN)	$\frac{F_p}{F_c}$	F_{tooth} (kN)
	t (mm)	w (mm)	h (mm)					
SP0A	10	14	65	55	310	530	0.58	883
SP0B	10	14	65	54	310	430	0.72	880
SP1A	8	17	75	49	150	440	0.34	712.2
SP1B	8	17	75	42	150	388	0.39	610.5
SP1C	8	17	75	40	150	370	0.41	581.4
SP2A	8	13	55	38	186	370	0.50	668.6
SP2B	8	13	55	45	186	434	0.43	791.8
SP3	8	17	55	30	215	333	0.65	527.9
SP4A	10	14	75	54	263	440	0.60	784.9
SP4B	10	14	75	38	263	360	0.73	552.3
SP5	10	18	65	28	345	295	1.17	449.8
SP6	10	14	65	24	310	280	1.11	385.6

Table 4.5 Test matrix

Bolts		
Number of bolts used m		4
Bolts' diameter d	(mm)	20
Bolts' material ult. strength f_{ub}		1200
Bolts' ult. resistance $F_{v,Rd}$	(kN)	1200
Bearing resistance		
Minimum ult. strength f_u		430
Steel section's flange thickness t_f	(mm)	15.6
Edge distance e_1	(mm)	40
Spacing p_1	(mm)	100
Factor α_b		0.63
Bearing resistance $F_{b,Rd}$	(kN)	681

Table 4.6 Bolts' strength and bearing resistance

A total shear resistance of 1200 kN was provided by the bolts which ensure that the bolts remain within elastic state of stress during the application of the loading. The total bearing resistance at the bolt holes was 680 kN. Table 4.7 includes the results derived

from the weld resistance checking using equation (19). The weld withstands a combination of shear force of 450 kN and secondary bending moment of 45 kN m, when the thickness of the weld throat is equal to 7 mm.

Maximum force F (kN)		450
Out of plane eccentricity e	(mm)	100
Secondary bending moment M	(kN m)	45
Width of the SHS tube b	(mm)	180
Thickness of the weld throat α	(mm)	7
Distance between point 1 and centre of gravity of weld	(mm)	90
Weld's area A_{weld}	(mm^2)	2520
Weld's second moment of area I_y	(mm^4)	27216 10^3
Normal stress σ_R	(N/mm^2)	148.8
Shear stress at point 1 τ_1	(N/mm^2)	105.4
Normal stress at point 1 σ_1	(N/mm^2)	105.4
Shear stress at point 1 τ_2	(N/mm^2)	178.6
Combined stress at point 1	(N/mm^2)	374
Correlation factor β_w		0.85
Weld resistance f_u	(N/mm^2)	430
Design weld resistance $f_u/ (\beta_w \gamma_{M2})$		405
Resistance of weld check		
$\sqrt{\sigma_1^2 + 3(\tau_1^2 + \tau_2^2)} \leq \frac{f_u}{\beta_w \gamma_{M2}}$		374≤405

Table 4.7 Resistance of weld

4.5 Horizontal Test Set up

The proposed demountable steel concrete composite connection was investigated by conducting a number of push out tests using a horizontal testing arrangement. The horizontal testing arrangement was selected instead of the vertical one proposed in BS EN 1994-1-1:2004 [4.12]. The reasons for this choice were presented in paragraph 2.3 of chapter 2, based on the research conducted by Lam [4.13]. Figures 4.16 and 4.17 show the plan and the side view of the horizontal test set up respectively. An hydraulic actuator of 1000 kN force capacity and 500 mm displacement capacity with attached

load cells was used to push the HCUs against the steel section through the spreader beam as indicated in Figure 4.1. The actuator was attached on a strong reaction frame which was bolted on the lab's strong floor using eight M28 high strength threaded rods. To ensure that the response of the reaction frame is elastic during the whole duration of

the loading a 3D FEM model was developed using the Abaqus Standard software and it is presented in paragraph 4.7. The steel section of each push out specimen was fixed on the lab's strong floor through four steel plates of 30 mm thickness welded on the bottom flange of the steel section and then bolted on the strong floor using M28 high strength threaded rods. The spreader beam was supported by two steel bases in both sides of the actuator, the top surface of which was greased to minimize the friction force during the sliding of the actuator, as shown in Figure 4.17. The slabs were protruding 100 mm from the steel section to allow the movement of the spreader beam against the steel section. The centroid of the actuator was in line with the mid-depth of the slabs. Two configurations were employed to transfer the load from the actuator to the specimens shown in Figure 4.17. The first configuration used wooden parts of high density and of rectangular cross section placed in the shear key formation between the HCUs and the flange of the spreader beam. The second configuration included the formation of a mortar tooth casted before starting the test between the HCUs and the flange of the steel section. All the push out specimens were tested employing the first configuration apart from tests SP1A and SP6 where the second configuration was employed. Figure 4.18 shows a 3D view of the test set up including one push out specimen ready for testing and employing the second set up configuration.

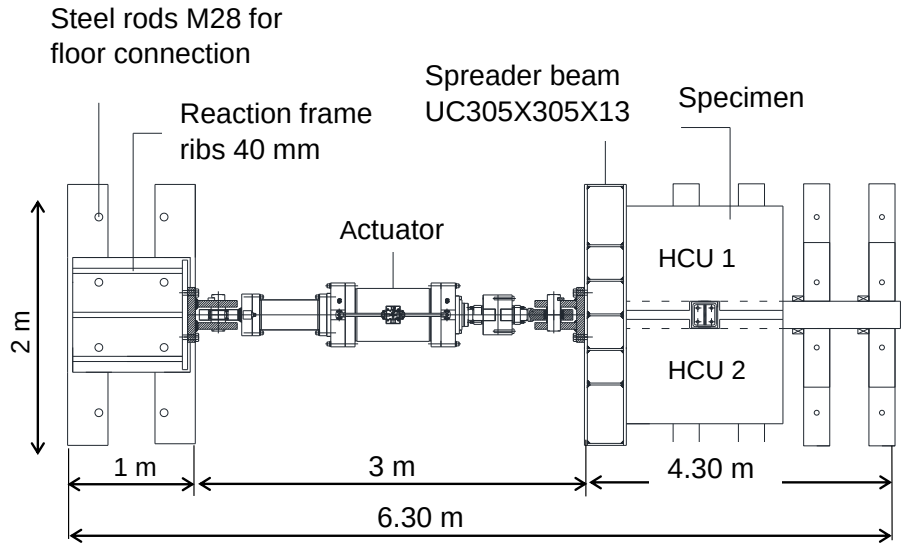

Figure 4.16 Plan view of the test set up

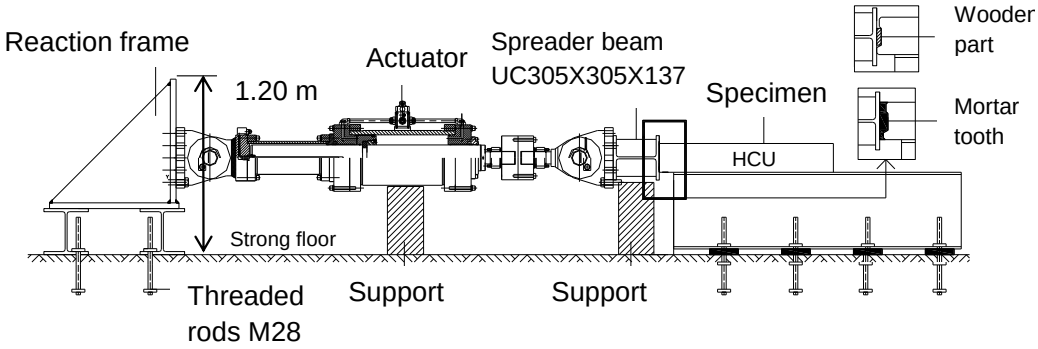

Figure 4.17 Side view of the test set up

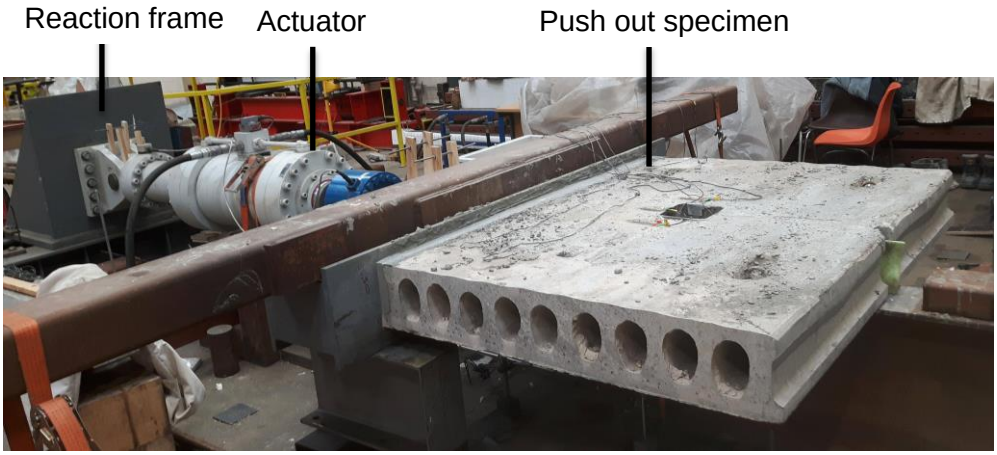

Figure 4.18 3D view of the horizontal test set up

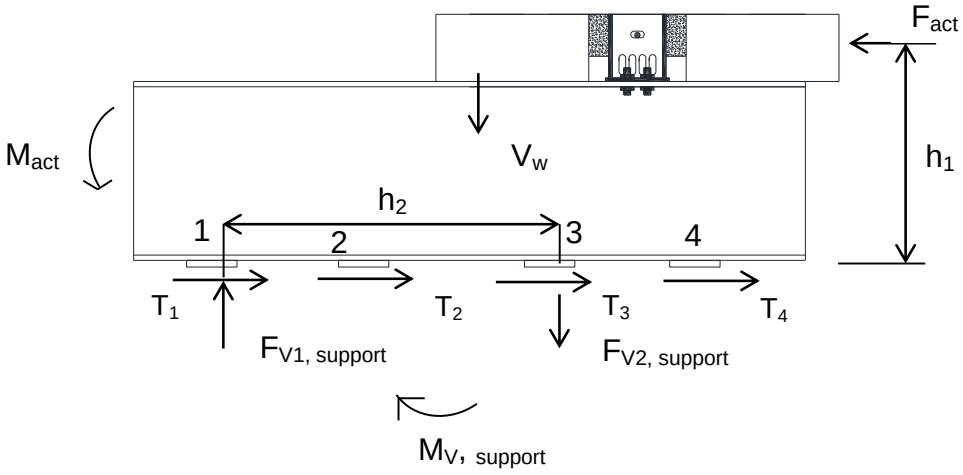

Figure 4.19 Mechanics using the horizontal test set up

Figure 4.19 shows the forces and the bending moments generated in push out specimens by the horizontal test arrangement used upon loading. The force F_{act} produced by the actuator generates the bending moment M_{act} which is balanced by the pair of forces

$F_{v1,support}$ and $F_{v2,\ support}$ with a small contribution of the self- weight of the push out specimen V_w. The push out specimens are supported vertically at points 1 and 3 and horizontally at points 1, 2, 3 and 4 as shown in Figure 4.19. If the mechanics are simplified so that the self-weight of the push out specimens is neglected, then $F_{V1,support}=F_{V2,support}$ and $M_{act}=F_{act}\ h_1=F_{V1,support}\ h_2=M_{V,support}$

4.6 Instrumentation and Testing Procedure

A number of instruments were used to monitor the behaviour of the concrete and steel components of the push out specimens during the application of the loading. Linear variable differential transducers, concrete and steel strain gauges were used and calibrated properly according to the calibration sheets provided by the corresponding manufacturing companies. Figure 4.20 shows an indicative position of the instruments installed on the push out specimens.

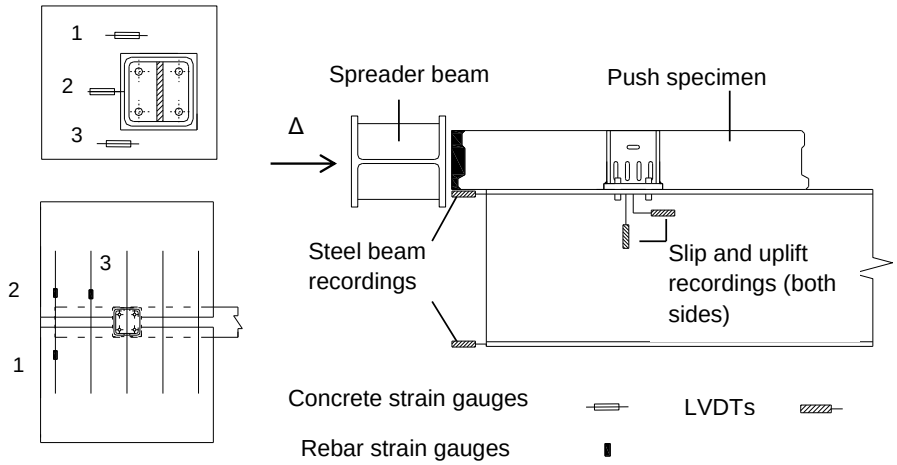

Figure 4.20 Indicative position of instruments installed on the specimens

4.6.1 Linear Variable Differential Transducers (LVDTs)

Two LVDTs were used to measure the longitudinal slip between the HCUs and the steel section placed on each side of the specimen. One end of each LVDT was attached to the bottom side of the HCU and the other one to the top flange of the steel section as closely as it is possible to the connection with the aid of magnetic gauge bases, as shown in Figure 4.21. Two LVDTs were used to measure the uplift placed on each side of the specimen, as shown in Figure 4.21 for the specimens SP1A and SP6. One end of each LVDT was attached to the bottom flange of the steel section and the other one was attached to the bottom side of the HCUs.

Figure 4.21 Indicative placements of LVDTs for slip and uplift measurement

Two additional LVDTs were used to measure any potential differential horizontal movement between the top and bottom flange of the steel section for the specimens SP1A and SP6.

4.6.2 Strain Gauges

A number of strain gauges were installed on the concrete and steel component of the specimens. Figure 4.22 shows an indicative installation of the strain gauges on the concrete and YP. Before the placement of the strain gauges on the concrete and steel, special treatments of the surfaces were made. A coarse sand paper was used to sand the steel surface until the virgin material was seen. A number of sand papers of different sizes were used to sand the surface of the concrete and the gauges installation was implemented according to the instructions mentioned in [4.14]. Adhesive tape was used to isolate the wires connected to the strain gauges from the steel surface of YP and between the two wires used for each gauge connection as shown in Figure 4.22.

Quarter Wheatstone bridge configuration was employed and proper resistors were used at the Beckhoff modules integrated to the MOOG system to monitor the development of strains of the concrete and steel. The Wheatstone bridge configuration is used to measure very small variations in resistance corresponding to changes in the length of the strain gauges which are described by the linear equation:

$$\varepsilon = \frac{-4V_r}{GF\ (1 + 2V_r)} \qquad (23)$$

, where ε is the strain, V_r is the difference in the voltage ratio V_{out}/V_{in} from unrestrained to restrained state, V_{out} is the bridge output voltage, V_{in} is the bridge excitation voltage and GF is the gauge factor provided by the strain gauges manufacturer. The results obtained from equation (23) were used to calibrate the strain gauges by introducing the maximum expected strain taking into account an output voltage of 10 V and 2.5 mV/V sensitivity. The maximum expected strain is calculated equal to 4694.8 με and 4878 με for the concrete and steel gauges respectively. Linear strain gauges of 60 mm gauge length, 120 ohms resistance and 2.13 gauge factor supplied by TML were installed on the concrete slabs. Standard strain gauges of Y series of 350 ohms resistance and 2.05 gauge factor supplied by HBM were installed on the steel strips and walls of the YP.

The concrete strain gauges were placed in various patterns around the YP which are different from specimen to specimen. Concrete strain gauges were placed in specimens SP1A, SP1C, SP4B, SP5 and SP6. Steel strain gauges were installed on the steel strips and one vertical wall of the YP, i.e. the one being closer in the loading surface. Steel strain gauges were installed on the YP of specimens SP1A, SP2B, SP3, SP4B and SP5. Steel strain gauges were installed on the steel rebars of specimen SP6.

Figure 4.22 Indicative installations of strain gauges (specimen SP1A)

The strain gauges were installed on the steel strips of YP close to the upper end of the steel strips, where plastic deformation was expected to develop. The normal strains recorded from the steel strain gauges are represented schematically in Figure 4.23. Figure 4.23 shows a part of a steel strip having width, w, and thickness, t, and the normal strains of the cross section developed under the imposed displacement 'Δ'. The strain gauges were installed on the steel strips' width instead of thickness to facilitate the installation procedure.

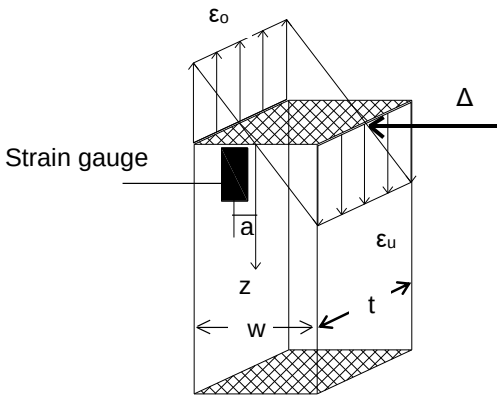

Figure 4.23 Strains' measurement of gauges installed on a YP's steel strip

The majority of the gauges installed on steel strips were positioned in a distance 'a' from the central axis z to avoid zero recordings around the neutral axis as shown in Figure 4.23. Strain gauges were installed on the interior side of the wall of YP to monitor the development of strains. The normal strains recorded from the steel strain gauges are represented schematically in Figure 4.24. Figure 4.24 shows a part of the wall of the YP, having thickness, t, the position of the gauge in the internal side of the wall and the normal strains developed under the imposed displacement 'Δ'. The 'In' and 'Out' designation showing in drawing indicates the internal and the external side of the YP. Since the results taken from the strain gauges are not directly usable by hand calculations, they will be verified by FEM analyses in chapter 6.

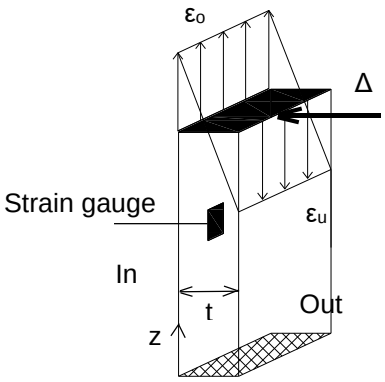

Figure 4.24 Strains' measurement of gauges installed on the YP's internal wall

4.6.3 Testing Procedure and Data Acquisition

Force control load was initially applied up to 40% of the expected failure load and then cycled 25 times between 5-40% of the expected failure load. The rate of cyclic loading was around 3 kN/s. After the cyclic loading, displacement control load was applied up

to failure with a constant rate of 0.2 mm/min. The cyclic loading was applied only to the group specimens SP2 and to the specimen SP3. Cracks and damages observed during the tests were seen by naked eye and recorded manually. All the measurements were available for monitoring on the screen of the computer during the application of the loading. The data acquired from the load cells, the LVDTs and the strain gauges was automatically recorded at a frequency of 5 Hz. The horizontal load was measured by the built-in load cell of the hydraulic actuator. The data was extracted from the system in CSV format in predefined units and the results were later processed.

4.7 Numerical analysis of the reaction frame

Abaqus Standard software was used to develop a numerical model for the reaction frame. The geometric characteristics of the reaction frame are shown in Figure 4.25. Three identical steel isosceles right angle triangles of 40 mm thickness were welded on one horizontal and one vertical steel plate of 40 mm thickness, as shown in Figure 4.25. The steel grade of the structure was S355 according to the manufacturer company. The reaction frame was bolted on the actuator's flange using ten high strength bolts. Figure 4.26 shows the numerical model for the reaction frame. Fully fixed boundary conditions were applied at the horizontal plate of the structure to represent the vertical support. The load was simulated as uniform pressure applied on a rectangular area of 420 x 420 mm around the gravity centre of the reaction frame. The steel material was taken into account considering yield stress of 350 N/mm^2 and taken into account the hardening part according to the prediction proposed by Gattesco [4.15]. Three dimensional 8-node linear brick elements with reduced integration (C3D8R) were used for the horizontal and vertical plate. Three dimensional 6-node linear triangular prisms (C3D6) were used for the steel triangles. An overall mesh of 20-30 mm was chosen for the component parts of the structure. Figure 4.27 shows the mesh utilized for the reaction frame. Tie constraints were enforced between the horizontal plate and the triangles as well as between the vertical plate and the triangles. Figure 4.28 shows the contour plot of the Von –Mises stress of the reaction frame. The results showed that the reaction frame is capable of withstanding the applied load without exhibiting plastic deformations and therefore it is safe to use it in tests.

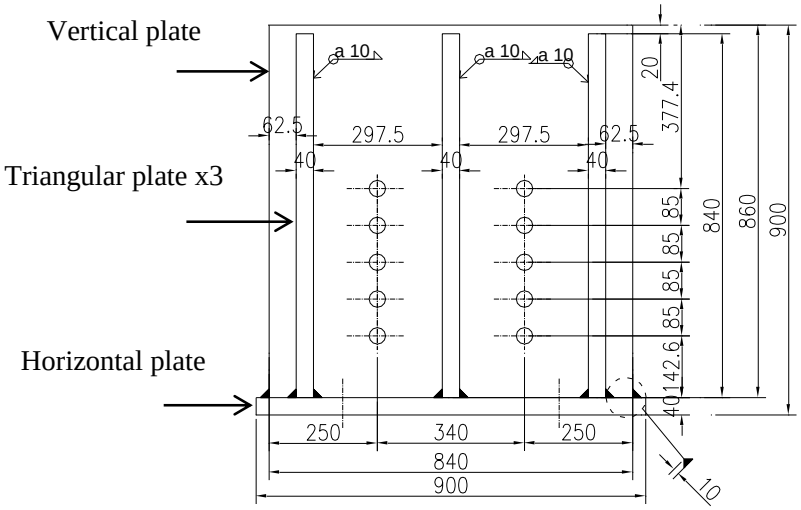

Figure 4.25 Geometric characteristics of the reaction frame

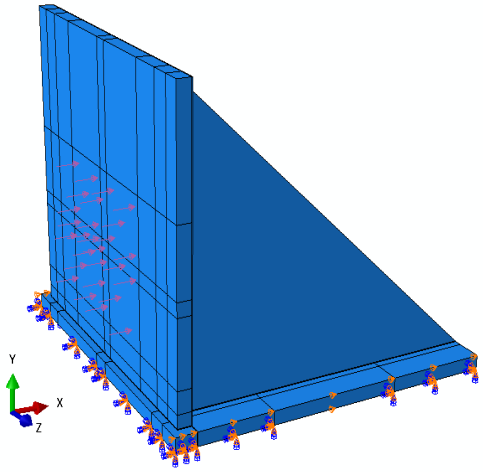

Figure 4.26 Numerical model for the reaction frame

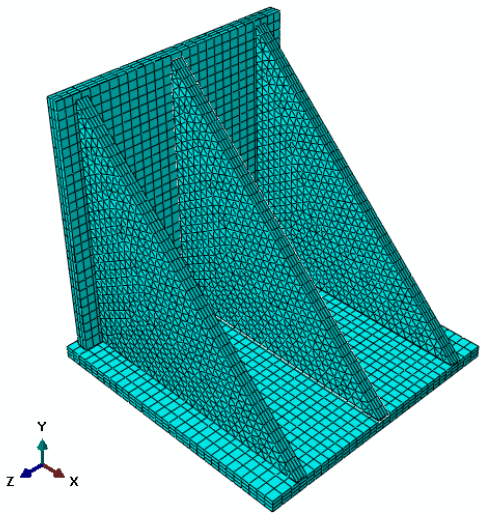

Figure 4.27 Mesh of the reaction frame

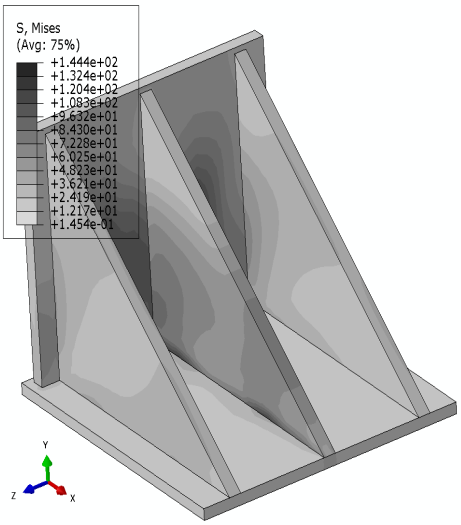

Figure 4.28 Von-Mises stress contour plot of the reaction frame

4.8 Reference List

[4.1] Bison Precast Floor Specification. <http://www.bison.co.uk/pdf/Bison-Hollowcore-Floors-Bearing-Details.pdf> (June 2018)

[4.2] BSI (British Standard Institution). BS EN 1992-1-1:2004, Design of concrete structures, Part 1-1: General rules and rules for buildings, London, UK (2004)

[4.3] Blind Bolt Product Specification. <https://www.blindbolt.co.uk/assets/data-docs/bb/bb-metric-tech-data.pdf>. (June 2018)

[4.4] Heavy Duty Bolt Installation. <https:// www.youtube.com watch?v= ehj0LLUMFG4> (June 2018)

[4.5] ASTM Standards, E8/E8M – 11, Standard Test Methods for Tension Testing of Metallic Materials (2011)

[4.6] L. Ingvarsson, *Cold-forming residual stresses in thin-walled structures*, Proc. 1st Int. Conf. on Thin-Walled Structures, Univ. of Strathclyde, Glasgow, United Kingdom, 575-587 (1979)

[4.7] C.C. Weng, T. Pekoz, *Residual stresses in cold-formed steel members*, Proc. 9th Int. Speciality Conf. on Cold-Formed Steel Structures, St. Louis, Montreal 1988, 167-189

[4.8] L. Gardner, D. A. Nethercot, *Numerical Modelling of Stainless Steel Structural Components-A consistent approach*, J. Struct. Eng.,130 (10), 1586-1601 (2004)

[4.9] BSI (British Standard Institution). BS EN 12350-2:2009. Testing fresh concrete, Part2: Slump tests, London, UK (2009)

[4.10] BSI (British Standard Institution). BS EN 12390-3:2009. Testing hardened concrete, Part 3: Compressive strength of test specimens, London, UK (2009)

[4.11] BSI (British Standard Institution). BS EN123906:2009. Testing hardened concrete, Part6: Tensile splitting strength of test specimens, London, UK (2009)

[4.12] BSI (British Standard Institution). BS EN 1991-1-1:2004. Deign of composite steel and concrete structures, Part 1.1: General rules and rules for buildings, London , UK (2004)

[4.13] D. Lam, *Capacities of headed stud shear connectors in composite steel beams with precast hollow core slabs*, J. Constr. Steel Res 63, 1160-1174 (2007)

[4.14] Instruction Bulletin B-127. Strain Gauges Installations with M-Bond 200 Adhesive. Retrieved from <http://www.vishaypg.com/docs/11127/11127B127.pdf> (June 2018)

[4.15] N. Gattesco, *Analytical modelling of nonlinear behaviour of composite beams with deformable connection*, J. Constr. Steel Res., 52(2), 195-218 (1999)

Chapter 5-Experimental Results and Discussion

5.1 Introduction

The push out test results are presented and discussed in this chapter. The structural behaviour of the proposed system was investigated by identifying the failure modes, the force-slip and uplift-slip behaviour and by summarizing the strain gauges' results. The strength obtained from the experiments was compared to the strength predictions presented in the previous chapter. The force-slip behaviour was qualitatively compared to the one of a welded headed stud used in conjunction with HCUs published elsewhere. The construction-deconstruction procedure of the proposed demountable connection and the feasibility of reusing the structural components were evaluated within the lab environment.

5.2 Failure Modes

5.2.1 Specimens' Group SP0

The initial concept included the use of innovative blind bolts to fix the YP on the top flange of the steel section. The 4th core of the specimen SP0A located just before the YP in the direction of loading (as shown in Figure 4.2 of chapter 4) remained hollow after casting of the specimen. The specimen SP0A failed suddenly and prematurely at a load of 100 kN almost immediately after the application of the loading. Figure 5.1 shows the diagonal cracking of the slab. Figure 5.2 shows the blind bolts after dismantling the specimen SP0A. The deformed shape of the blind bolts which was slightly bent and the damage region of the bolts close to the legs of the bolts indicated that the specific type of bolt initially chosen to be used in tests was not capable of locking together the two connected steel plates, i.e. the steel base of the YP and the steel section's top flange, under the combination of shear force and secondary bending moment introduced. At that time of the first test, it was not clear whether the diagonal cracking of the slabs was related to the use of blind bolts or to a combination of factors, e.g. the use of blind bolts and the non-filled with *in situ* concrete 4th core of the HCUs.

Therefore the following test included the blind bolts and was designed with the 4th core of the HCUs full of *in situ* concrete. The specimen SP0B failed prematurely in transverse cracking at a load of 125 kN and corresponding slip of 2.3 mm. Figure 5.3

shows the transverse cracking of the slab. Figure 5.4 shows the blind bolts after dismantling the specimen SP0B. The deformed shape and the damage region close to the legs of the bolts was very similar to the one of the bolts of the previously tested specimen and indicated once more the disconnection of the YP from the steel section. Figure 5.5 clearly shows this disconnection. The transverse crack was formed due to the development of secondary negative bending moments along the transverse direction of the steel section where the connection of the YP to the steel section was and where the crack was formed. Based on the experimental results, the diagonal cracking of the slabs of specimen SP0A was related to the non-filled with *in situ* concrete 4th core of the HCUs. Since no useful results were produced from the first two tests including the blind bolts, the initial concept was abandoned and all the following ten tests SP1-SP6 included high strength allen bolts with washers and nuts. The 4th of the HCUs was filled with *in situ* concrete in the following tests to avoid early diagonal cracking of the slabs.

Figure 5.1 Shear cracking of slabs' specimen SP0A

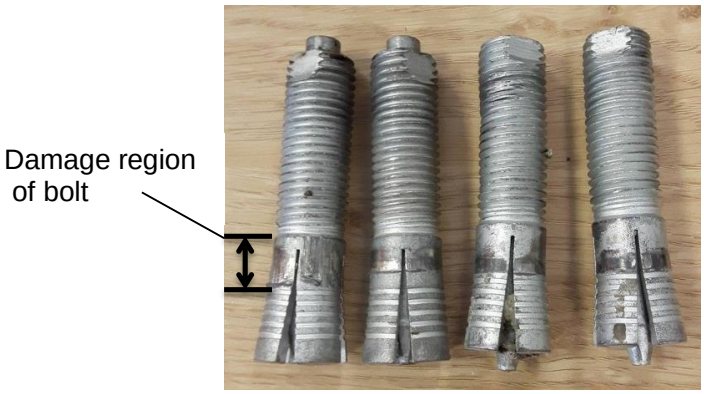

Figure 5.2 Blind bolts after dismantling the specimen SP0A

Figure 5.3 Concrete failure of slabs' specimen SP0B

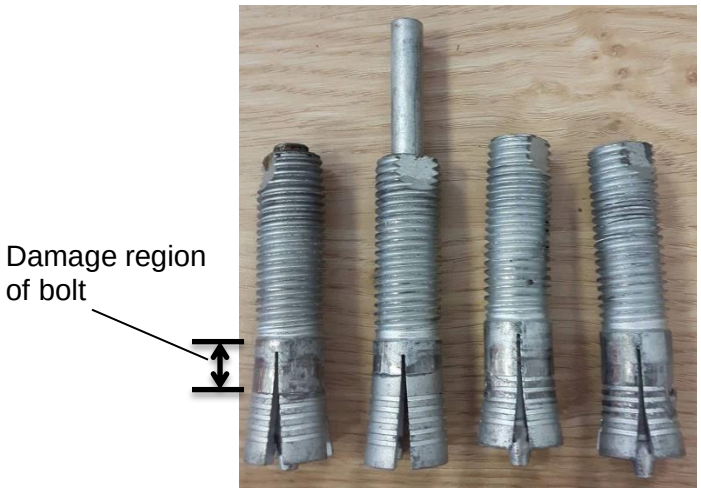

Figure 5.4 Blind bolts after dismantling the specimen SP0B

Figure 5.5 Disconnection of the YP from the steel section

5.2.2 Specimens' Group SP1-SP6

The push out specimens belonging to the group SP1-SP4 failed in a ductile mode showing plastic deformations in the YP due to plastic bending. The specimens were

constructed having a low to medium YP strength combined with normal to high concrete strength. No concrete cracking was observed during these tests after considerable amount of slip was reached. The specimen SP1A was tested until all the possible failure modes were met. The following tests belonging to this group were tested up to the slip of around 30-35 mm considering that it is impractical to meet higher slips in steel concrete composite beams. Indicatively mentioned, slips of more than 24 mm are not practical when considering in steel concrete composite beams even in the case of partial shear connection as shown by Zona and Ranzi [5.1], who performed parametric numerical studies in steel concrete composite beams taking into account a number of parameters as propped and un-propped construction, the degree of shear connection and variable span lengths. An additional reason for this decision is that the YPs should not be excessively deformed so that the push out specimens can be easily deconstructed.

The test SP1A was brought to complete failure. The structural response was characterised by the bending of the YP up to the force of 357 kN and corresponding slip of 47 mm. Plastic deformations were concentrated at the ends of the YP's steel strips and vertical walls. No evidence of concrete cracks were seen up to this point. At a slip of 47 mm the first row of bolts in the direction of loading started bearing at the YP's wall. Upon further increase of the loading the slabs started riding over the YP due to large deformation of the YP's walls. This new deformed state introduced secondary hogging moments within the slab which finally led to the flexural cracking of the slab exhibited by the formation of a large crack across the width of the composite cross section and located just before the YP in the direction of the loading. The sudden crack was formed at 500 kN with corresponding relative slip 50 mm. Figure 5.6 shows the deformed shape of the YP at the end of test. Due to large plastic deformations, the steel at the points of maximum concentrate plastic strain was torn, as shown in Figure 5.6. Figure 5.7 shows the bearing of the first row of the bolts at the wall of the YP. Figure 5.8 shows the ultimate failure of the slab. Although the final failure of the slab was brittle due to concrete cracking, the structural behaviour of the specimen is primarily characterized by the ductile behaviour of the YP up to the excessive relative slip of 50 mm.

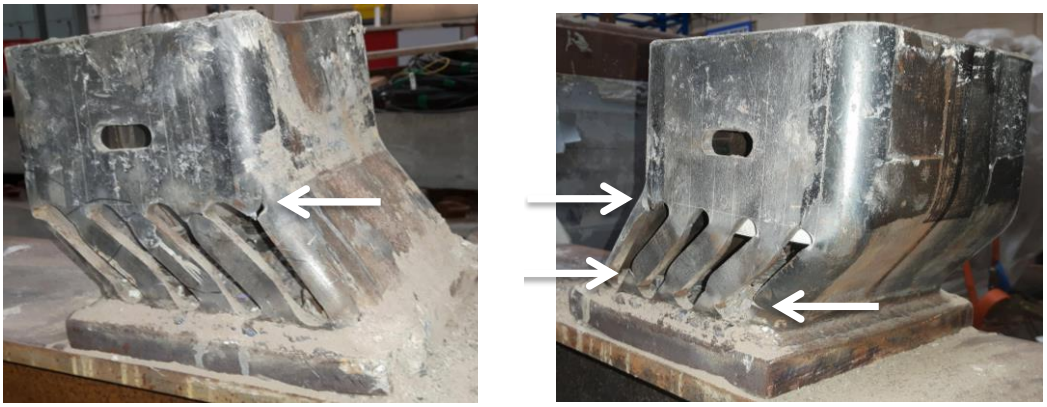

a) b)

Figure 5.6 Deformed shape of YP of push out specimen SP1A-View a); and view b)

Figure 5.7 Bolts bearing at the YP's wall

Figure 5.8 Ultimate failure mode of slab of push out specimen SP1A

The specimen SP1C was the only one constructed having insufficient amount of concrete around the corners of YP. This was implemented by placing polythene foams of adequate length only at the sides of YP in the transverse direction of the steel section's axis. The inadequate amount of concrete around the corners of the YP

resulted in out of bending deformation of the YP, as shown in Figures 5.9 and 5.10. Figure 5.10 shows the deformed shape of the YP after dismantling the specimen. By placing considerable amount of concrete around the corners of YP proper boundary conditions are created restraining the opening of the corners during the application of the load.

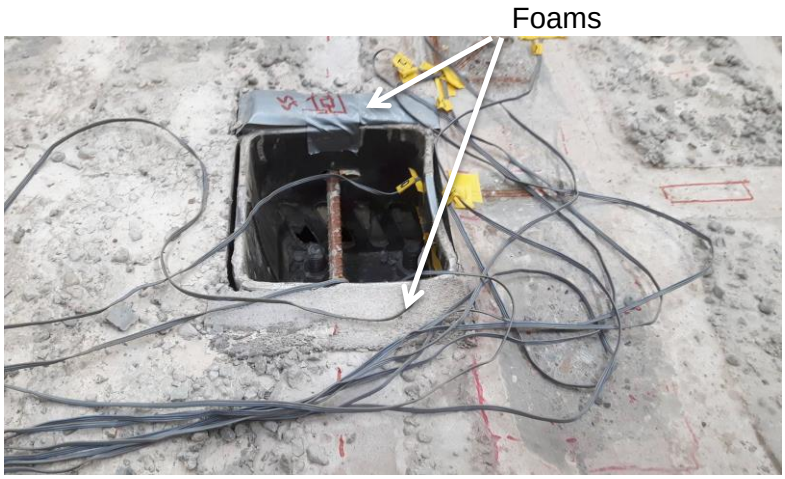

Figure 5.9 Push out specimen SP1C at the end of the test

Figure 5.10 Deformed shape of YP of push out specimen SP1C

The specimen SP5 was designed to have a high strength YP combined with normal concrete strength. A transverse crack was seen in the surface of the specimen at 130 kN and corresponding slip 0.9 mm. The crack was formed in the interface between the 4th core of the HCU and the *in situ* concrete and was seen in one side of the specimen. A second transverse crack was seen in the surface of the specimen between the 5th core of the HCU and the *in situ* concrete, where the middle rebar of the slab was placed, at a load of 200 kN and corresponding relative slip of 2.2 mm. Shear cracks were seen in the surface of the specimen when the load was 314 kN and corresponding slip 7.2 mm at one side of the specimen. The shear cracks became wider with further increase of the

force and extensive shear cracking was seen at 321 kN and corresponding slip 8.5 mm, followed by a sudden drop in the load at 286 kN where the test was stopped. The formation of the transverse cracks was unexpected and was attributed to out of plane eccentricities introduced to the specimen due to improper application of the loading related to imperfections of the specific HCUs used. The imperfections were located at the edge of the units which were in contact with the spreader beam and were not perceivable before starting the test. Although the shear cracking of the slabs was predicted by equation (21) and the ratio F_p / F_c given in Table 4.5 was equal to 1.17, the failure of the slabs might be accelerated because of the improper application of the load. The non-symmetric formation of the shear cracks was attributed to secondary torsional effects. Figure 5.11 shows the cracks formed in the specimen SP5 at the end of the test. After dismantling of the specimen, very little deformation was seen in the YP. Figure 5.12 shows the deformed shape of YP at the end of the test after dismantling the specimen.

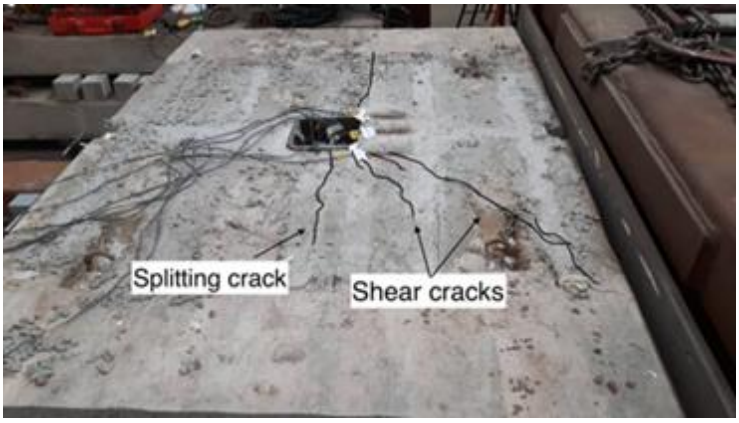

Figure 5.11 Push out specimen SP5 at the end of test

Figure 5.12 Deformed shape of YP of push out specimen SP5

The specimen SP6 was designed to have a high strength YP combined with normal concrete strength. The specimen failed in a mixed mode derived from the plastic

bending of the YP and the brittle cracking of concrete exhibited at a later stage during the application of the load. The response was ductile up to 427 kN and corresponding relative slip of 19 mm. Up to this point, no concrete cracking was observed. Diagonal cracks were seen in the top surface of the slabs at 19.5 mm and continued propagating up to 20.7 mm slip resulting in slightly reduction of the force from 427 kN to 423 kN. The specimen ultimately failed in extensive shear cracking at 423 kN and corresponding slip 23.7 mm. Figures 5.13 and 5.14 show the specimen SP6 at the end of the test. Figure 5.15 shows the deformed shape of the YP at the end of the test after dismantling the specimen.

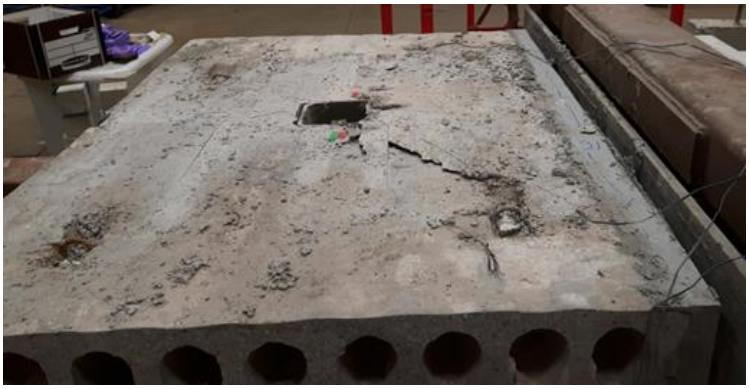

Figure 5.13 Push out specimen SP6 at the end of test

Figure 5.14 Push out specimen SP6 at the end of test (closer view)

Figure 5.15 Deformed shape of YP of push out specimen SP6

A secondary failure mode common to all tests and not involving with the longitudinal shear resisting mechanism was the concrete crushing of the corner of the concrete tooth. Figure 5.16 a) shows the mechanism under which the corner of the concrete tooth is crushed in compression due to the bending of the YP. Figure 5.16 b) shows indicatively the crushing of the corner of the concrete tooth for the specimen SP6.

Therefore, there is only a small amount of concrete near the corner of the concrete tooth being under compression and not all the surface of the concrete tooth as it was initially assumed. Upon the bending of the YP, the concrete tooth is detached from the YP apart from the small region near the concrete corner which is in continuous contact during testing. Thus, equation (22) presented in chapter 3 for the strength of the concrete tooth under direct compressions is never critical.

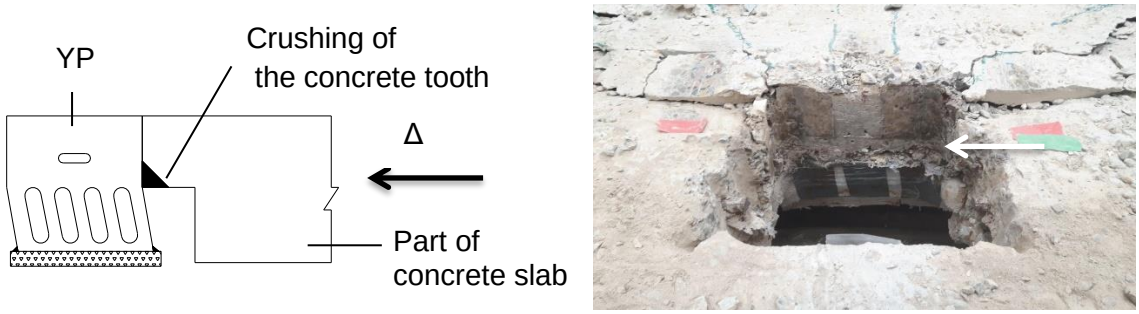

a) b)

Figure 5.16 a) Mechanism causing the crushing of the concrete tooth; and b) crushing of the concrete tooth of specimen SP6

5.3 Force-slip Behaviour

The force-slip curve given for each push out specimen represents the average force-slip

curve according to the slip recordings taken from the two LVDTs placed on either side of each push out specimen. Figure 5.17 shows the force-slip behaviour of the specimens belonging to the group SP1. The sudden increase of the force in specimen SP1A indicates the initiation of the bearing of the bolts on the YP's wall at a slip of 47 mm and corresponding force 357 kN. The bolts continued bearing on the YP's wall until the slip of 50 mm and corresponding force 500 kN. The structural response after this point is characterized by the gradual decrease of the force due to the formation of the transverse crack until the complete failure of the slab. The force-slip response of the push out specimen SP1B is identical to the specimen SP1A up to 34 mm of slip. The push out specimen SP1C exhibited reduced strength and stiffness compared to the ones of specimens SP1A and SP1B. The specimen SP1C was constructed with reduced amount of concrete around the corners of YP resulting in out of bending deformation.

Figure 5.18 shows the force-slip curves of specimens' group SP2 and Figure 5.19 shows the force-slip curves of specimens' group SP4 and of specimen SP3. The behaviour between the specimens SP2A and SP2B is similar while the strength of specimen SP2A is slightly higher compared to the one of specimen SP2B by 10 kN. The behaviour between the specimens SP4A and SP4B is identical. Figures 5.20 and 5.21 show the force-slip response of specimens SP2A and SP3 up to 2 mm of slip respectively. Twenty five cycles were initially applied between 5-40% of the expected yielding force for these specimens. There is some friction involving in the structural response of the specimens during the application of the cyclic loading emanated from the inevitable contact between the spreader beam and the HCUs.

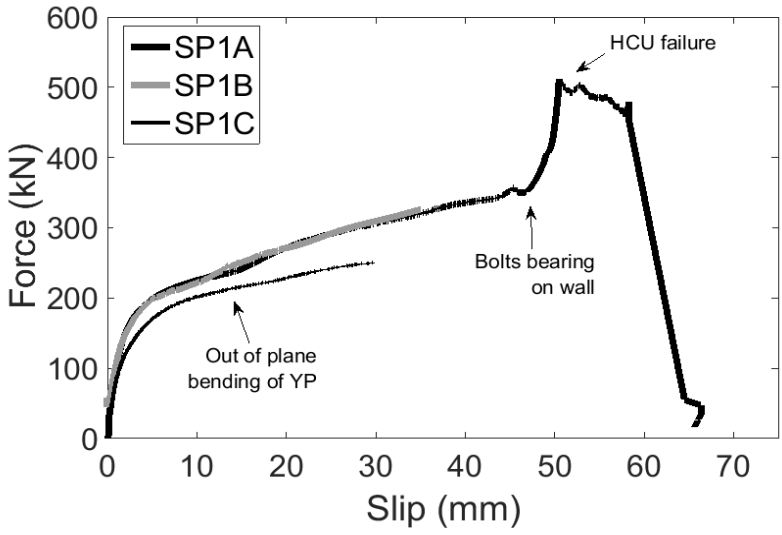

Figure 5.17 Force-slip behaviour of specimens' group SP1

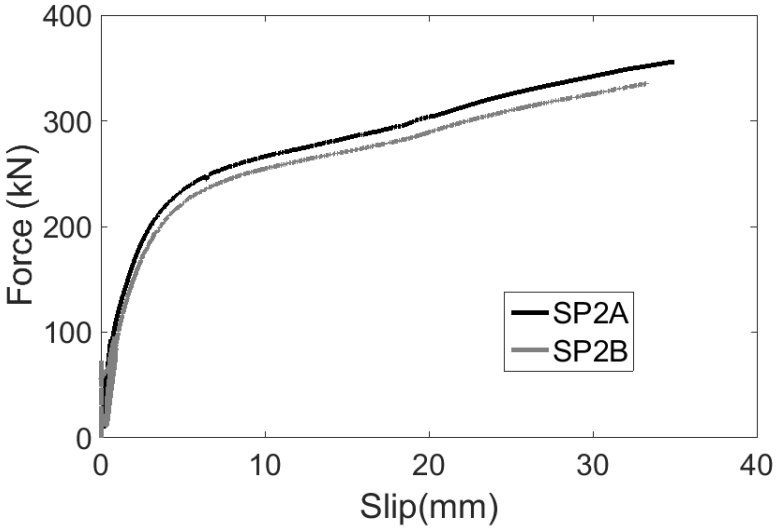

Figure 5.18 Force-slip behaviour of specimens' group SP2

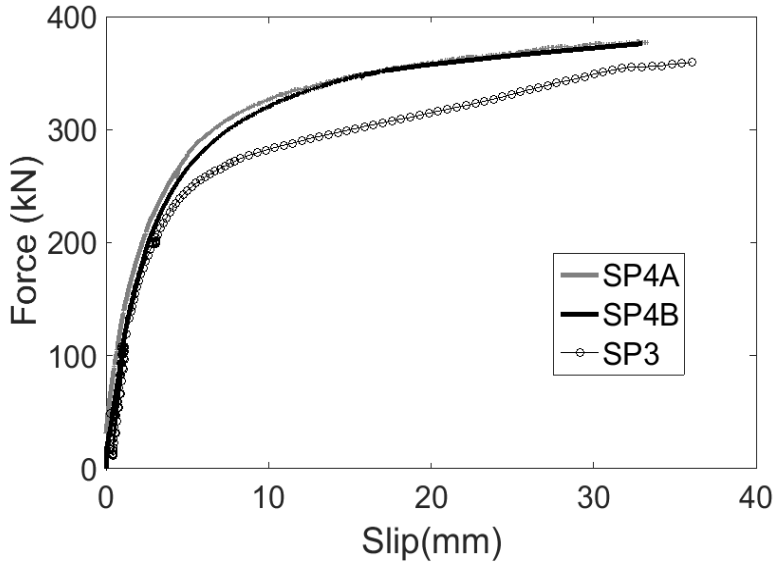

Figure 5.19 Force-slip behaviour of specimens' group SP4 and specimen SP3

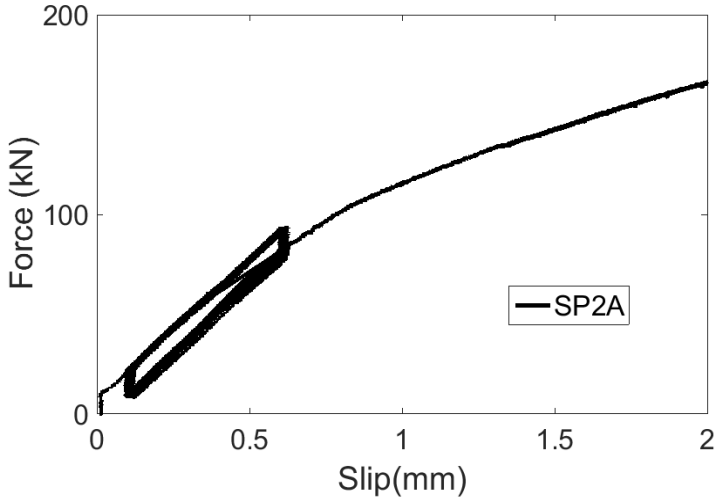

Figure 5.20 Force –slip behaviour up to 2 mm of specimen SP2A

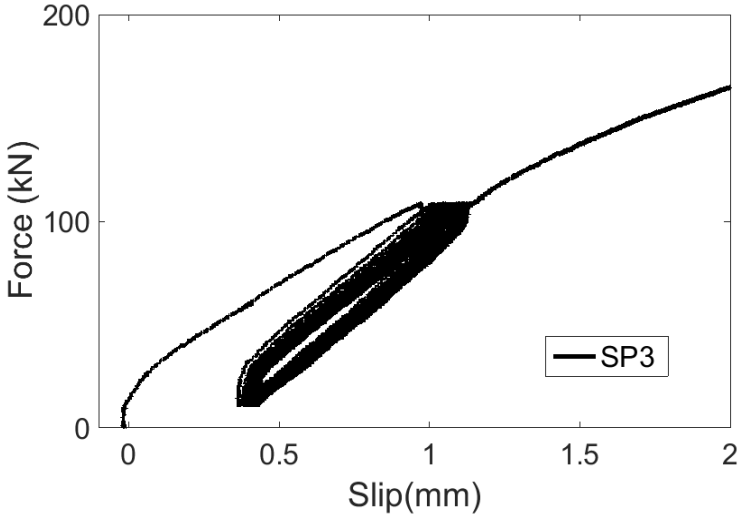

Figure 5.21 Force-slip behaviour up to 2 mm of specimen SP3

Figure 5.22 shows the force-slip behaviour of specimens SP5 and SP6 involving concrete damages. The YP of the specimen SP5 was stronger to the one of specimen SP6, nevertheless the latter achieved higher stiffness and strength. This is attributed to the premature concrete failure of the slab of specimen SP5 which occurred before fully yielding of YP. Although the specimen SP5 exhibited the lowest slip capacity among all the specimens tested, i.e. 8.3 mm, it is still higher than the one required by Eurocode 4 [5.2] for ductile shear connectors, i.e. 6 mm. The shear capacity of the slab of specimen SP6 was lost when the force was 423 kN and corresponding slip 20.7 mm as indicated by the decrease of the force shown in Figure 5.22. After this point, the force was stabilized and ultimately failed at 423 kN and 23.7 mm slip.

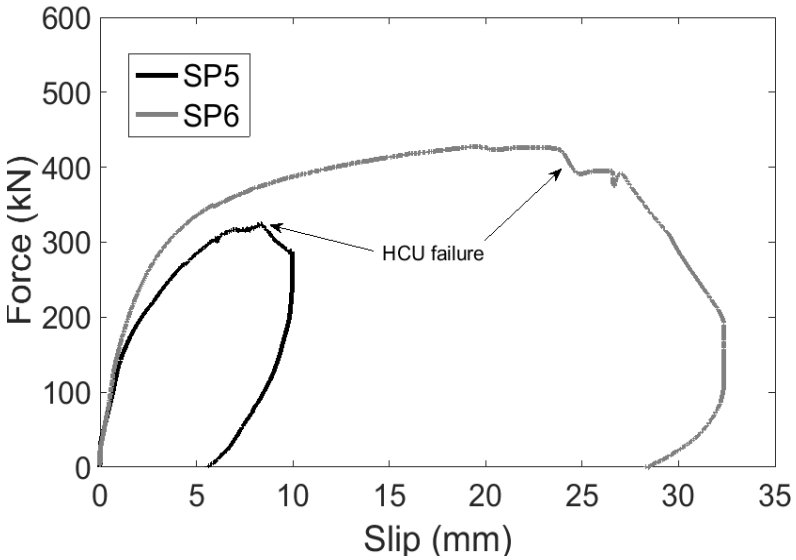

Figure 5.22 Force-slip behaviour of specimens SP5 and SP6

Figures 5.23 and 5.24 summarize the force-slip curves of the specimens tested and the force-slip curves up to 2 mm of relative slip including one push out specimen for each specimens' group. The specimens SP1-SP4 designed to have the ductile mode of failure achieved very high slips up to 30-35 mm while the force was continuously increasing due to the hardening of the YP. For the specimens SP1-SP4 and SP6, showing the ductile and the mixed failure mode respectively, increased strength and stiffness was achieved by altering the geometric properties of the YP. The stiffness of the specimens SP2A, SP3 and SP6 was higher than the stiffness of the specimens SP1B and SP4A, as shown in Figure 5.24. Although the strength obtained from the specimen SP4A was higher than the one obtained from the specimen SP1B, the stiffness between those two specimens was very similar. It is noted that the height of the YP's steel strips of the specimens' group SP2 and of specimen SP3 was the shortest one tested in the present research work and it was equal to 55 mm, while the height of the YP's steel strips of the specimens' group SP1 and SP4 was the longest one tested and equal to 75 mm. A reasonable assumption is that the stiffness of the YP is related to the stiffness of the connection; if the former increases the latter also increases. Between two specimens including YPs with identical geometric characteristics apart from their steel strips' height, e.g. SP1A and SP3, the one including the YP with the shortest strips had higher stiffness, as shown in Fig. 5.24 and Table 5.1. Therefore, the stiffness of the YP could be maximized by minimizing the steel strips' height, considering that the stiffness of each strip is related to its height according to equation $k=12\ E\ I/\ h^3$ for fully fixed boundary conditions at both ends (where h is the height of each steel strip).

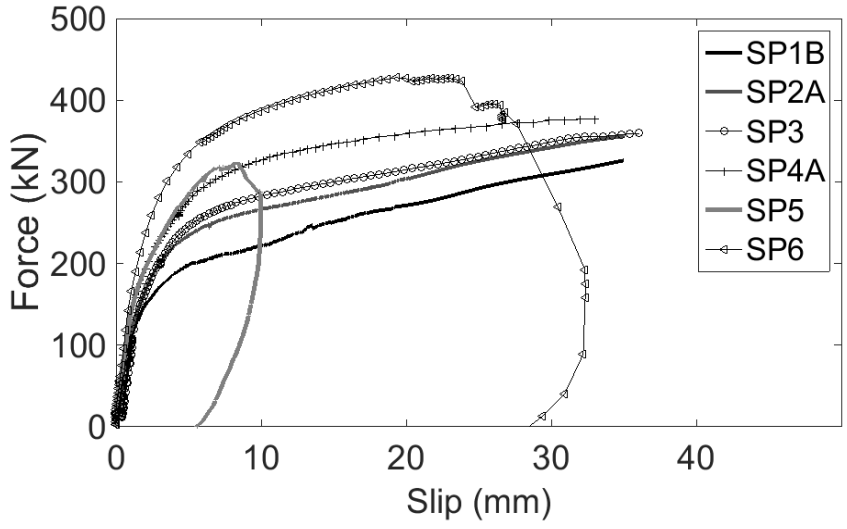

Figure 5.23 Force-slip behaviour of specimens (one specimen per group)

Since the geometry of the YP is complex, more parametric analyses are needed to identify the influence of the height among the other geometric parameters of the YP, i.e. the width, the height and the thickness of the YP's steel strips, on the stiffness of the proposed connection.

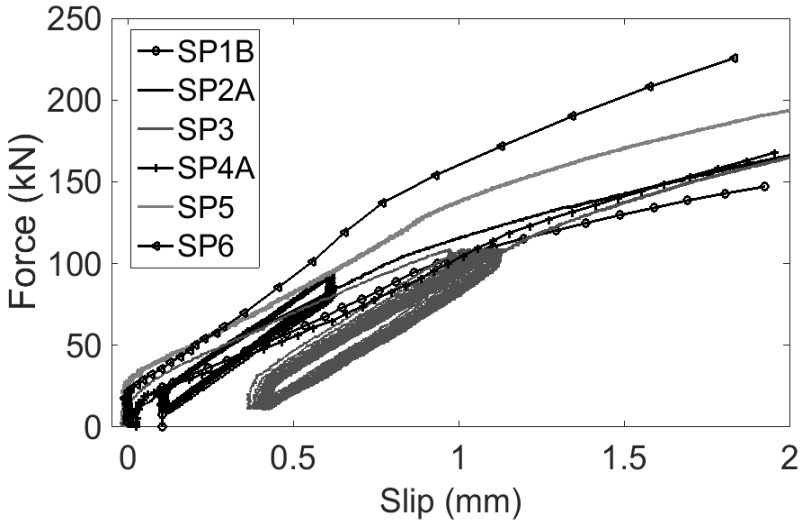

Figure 5.24 Force-slip behaviour of specimens (one specimen per group) up to 2 mm

5.4 Comparisons with Strength Predictions

Table 5.1 gives the test results including the experimental yield strength, $F_{y,exp}$, the maximum force obtained from tests, $F_{max,exp}$, the slip at the maximum force, and the ratios between the experimental yielding force to the predicted one using equation (5) indicated as $F_{y,exp}/F_p$, the maximum force obtained from tests to the predicted shear resistance according to equation (21), indicated as $F_{max,exp}/F_c$ and the maximum force obtained from tests to the experimental yield strength indicated as $F_{max,exp}/F_{y,exp}$. The stiffness, K_i, measured for each specimen is additionally given. The maximum force obtained from tests and the corresponding slip for specimen SP1A are the ones determined just before the bearing of the first row of bolts on the YP's wall, i.e. 357 kN and 47 mm respectively. The yield force of the specimen SP5 is not defined since the YP exhibited very little deformation and did not fully yield.

Based on the results shown in Table 5.1, the ratio $F_{y,exp}/F_p$ has a mean value of 1.06 with standard deviation 0.05, which indicates that equation (21) based on simple mechanics can predict accurately the yield force of the YP when there is no early failure of the concrete slab. The ratio $F_{max,exp}/F_c$ is less than one in specimens SP1A to SP2B and in specimen SP4A. The same ratio is equal to 1.09 and 1.53 for the specimens SP5 and

SP6 respectively which failed in shear cracking. The ratio of the yielding force to the shear resistance of the slab, F_p/F_c, used in Table 4.6 of chapter 4 for the initial design of the specimens predicted the shear cracking of the two specimens and also the integrity of the concrete for the rest. However, the ratio $F_{max,exp}/F_c$ could be used for an indicative prediction of the concrete failure in shear on the safety side; the specimens SP3 and SP4B having a ratio more than one did not fail in shear cracking.

The hardening of the YP is estimated by the ratio $F_{max,exp}/F_{y,exp}$ which has a value of around 2, 1.8 and 1.4 for the specimens' group SP1, SP2 and SP4 respectively and 1.56 and 1.33 for the specimens SP3 and SP6 respectively. Thus, the above ratio reduces as the YP is stronger relative to the concrete slab. This hardening behaviour of the proposed shear connector is different to the typical behaviour of a ductile welded headed stud embedded in HCUs which exhibits a plastic plateau before ultimate failure [5.3]. The lowest stiffness was measured for the specimens belonging to the group SP1 followed by the specimens belonging to the group SP4. The specimen SP1C which exhibited out of bending deformation has the lowest stiffness measured among the other specimens belonging to this group. The maximum stiffness was measured for the specimens SP3 and SP6. The mean value of the stiffness that can be achieved using the proposed shear connection and given the specific geometries of YP used in the present research work is 110 kN/mm with standard deviation 20.

Specimen	$F_{y,exp}$ (kN)	$F_{max,exp}$ (kN)	Slip at max.force (mm)	K_i	$\frac{F_{y,exp}}{F_p}$	$\frac{F_{max,exp}}{F_c}$	$\frac{F_{max,exp}}{F_{y,exp}}$
SP1A	170	357	47	95	1.13	0.81	2.10
SP1B	170	325	34	98	1.13	0.84	1.91
SP1C	160	250	30	75	1.07	0.68	2.23
SP2A	200	356	35	130	1.08	0.96	1.78
SP2B	200	339	33	123	1.08	0.78	1.79
SP3	230	359	36	135	1.07	1.08	1.56
SP4A	260	378	33	110	0.99	0.86	1.37
SP4B	260	375	33	105	0.99	1.04	1.44
SP5	N.A.	321	8.3	110	N.A.	1.09	N.A.
SP6	320	427	19.6	138	1.03	1.53	1.33

Table 5.1 Test results

5.5 Qualitative Comparison with Welded Headed Studs

Figure 5.25 shows the force-slip curves of specimens SP2A, SP3 and SP4A plotted together with the force-slip curve of a conventional headed stud of 19 mm diameter used in conjunction with HCUs tested in push out tests by Lam [5.3]. The comparison is drawn only to highlight the potential of a new DSC compared to the conventional steel concrete composite connection using welded studs. Therefore, the comparison drawn is only qualitative. Based on Figure 5.25, the proposed connection can achieve increased strength and maintain the force at high slips of more than 30-35 mm. Figure 5.26 shows the force-slip behaviour of the specimen SP3 plotted together with the conventional welded headed stud up to 2 mm of slip. The stiffness achieved by the proposed connection is comparable to the one of the welded stud mentioned.

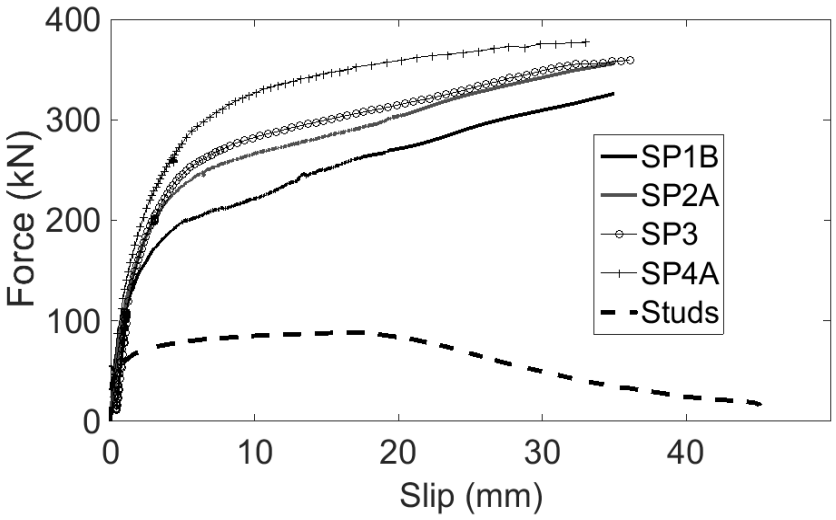

Figure 5.25 Comparison with welded studs taken from [5.3]

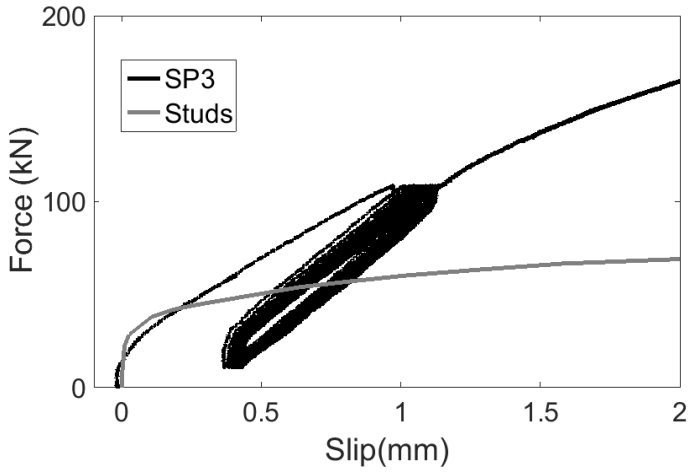

Figure 5.26 Stiffness comparison with welded studs taken from [5.3]

5.6 Uplift –slip Behaviour

Figure 5.27 shows the development of uplift with increasing relative slip during the tests SP1A and SP6. The plots represent average values taken from the recordings of the two LVDTs used to measure the uplift. The uplift for the specimen SP1A was linearly increasing up to 2 mm of relative slip, at which point it was equal to 1.4 mm. The uplift reached the value of 3.3 mm at 47 mm of slip, just before the bearing of the bolts on the YP's wall. After this point the uplift increased suddenly as the YP was excessively deformed and the slab moved upwards until complete failure occurred at 50 mm of relative slip and corresponding uplift 6.3 mm.

The uplift of the specimen SP6 was recorded 5.5 mm, following a continuously increasing trend. According to Eurocode 4 [5.2], the transverse separation of the slab should be limited so as to be equal to half of the longitudinal relative slip when the shear connectors are subjected to 80% of their ultimate load. The uplift is acceptable for the specimens and equal to 1.98 mm and 2.48 mm at 80% of the ultimate load with corresponding longitudinal slips 22 and 5.24 mm for the specimens SP1A and SP6 respectively.

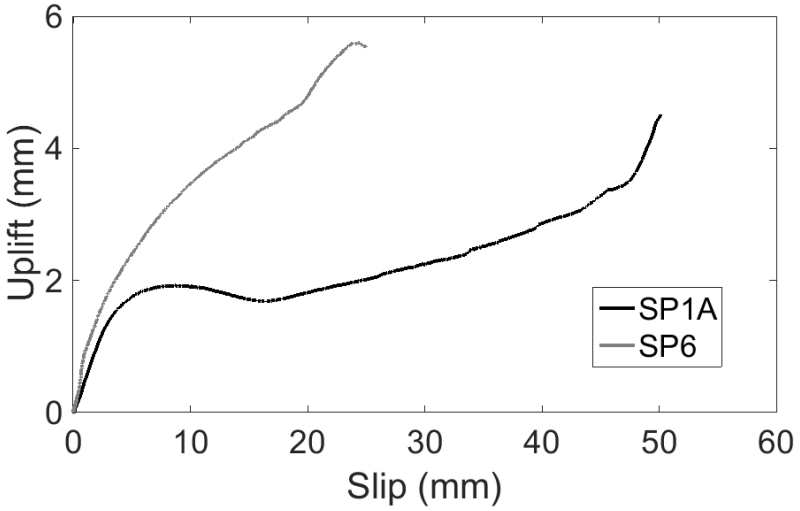

Figure 5.27 Uplift-slip behaviour

5.7 Strain Gauges Results

The results obtained from the strain gauges are represented in force-microstrain graph, where force is the total force produced by the actuator. Figures 5.28-5.33 show the results of the strain gauges installed on the concrete slab of the specimens SP1A, SP1C, SP2B, SP4B, SP5 and SP6.

The exact position of each strain gauge is shown in the inset of each figure. The strain gauges placed at the mid width of the concrete tooth recorded almost zero strains, i.e. gauges 3 and 1 of specimens SP1A and SP1C respectively, gauge 1 of specimen SP4B and gauge 2 of specimen SP6. This indicates that the compressive stress on the face of the YP is not significant and can be explained considering the fact that the YP deforms in such a way that the top side of the YP and the top fibres of the concrete tooth disconnect from each other. The compressive stress increases towards the bottom fibres of the concrete tooth, which is shown by the local concrete crushing of the bottom part of the concrete tooth, as explained in the failure modes and shown in Figure 5.16.

The strain gauges placed closer to the corners of YP recorded small compressive strains of maximum 500 με, i.e. gauge 4 of specimen SP1A, and of maximum 200 με, i.e. gauges 3 and 4 of specimen SP1C, gauges 3 and 4 of specimen SP2B and gauges 2, 3 and 4 of specimen SP4B. The recordings of the strain gauges installed approximately on the mid width of the YP in the transverse direction, i.e. gauges 1 and 5 of specimen SP1A and 1 and 3 of specimen SP6, indicated large tensile strains up to 3000 με approximately. These tensile strains which were recorded are very high; it is possible that the presence of microcracks invisible to the naked eye were formed prematurely and caused detachment of the gauges from the concrete. Gauge 1 of specimen SP5 recorded very small tensile strains while gauge 2 installed on the side where the shear cracks were formed recorded initially compressive strains which turned gradually to tensile until the sudden detachment of the gauge at 270 kN approximately due to the shear crack.

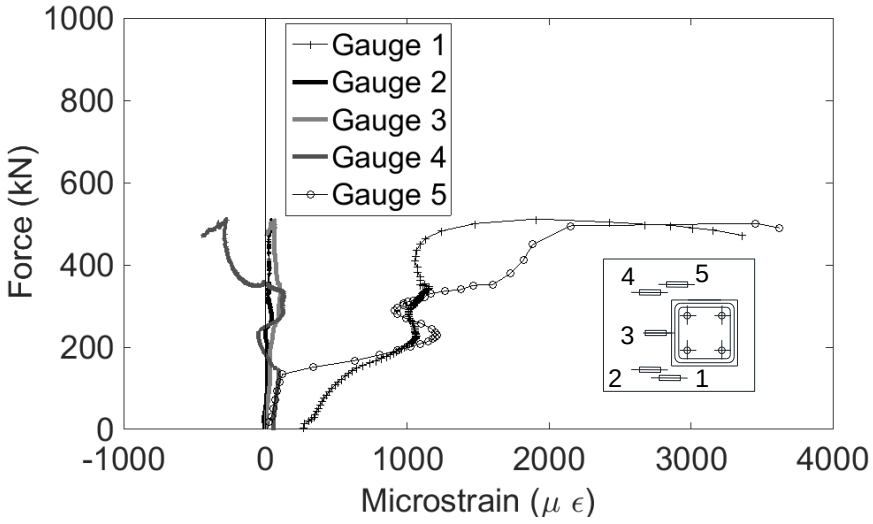

Figure 5.28 Concrete gauges results of specimen SP1A

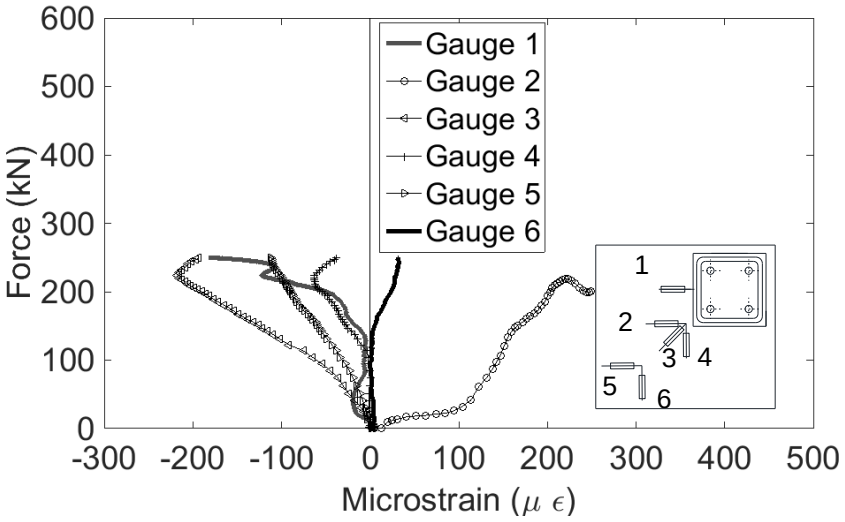

Figure 5.29 Concrete gauges results of specimen SP1C

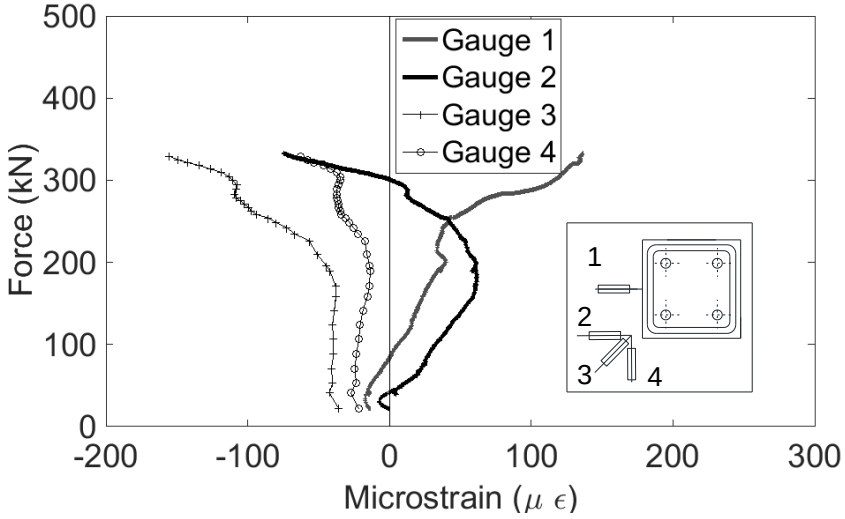

Figure 5.30 Concrete gauges results of specimen SP2B

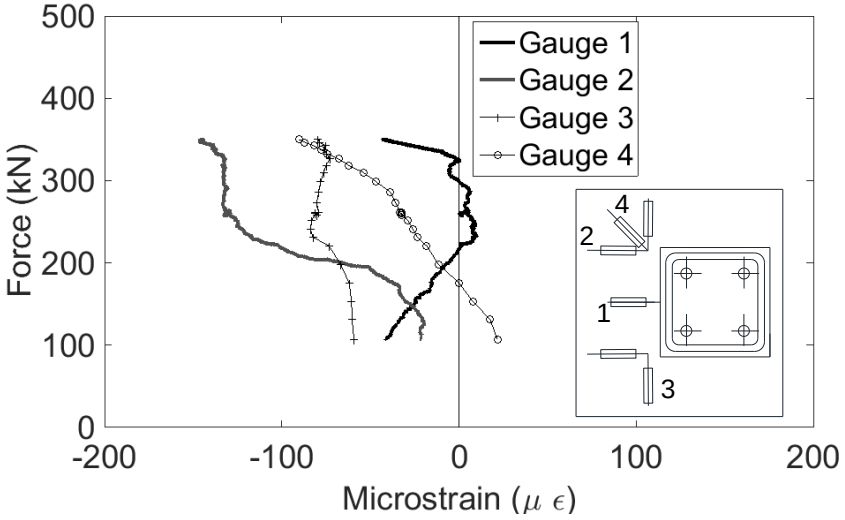

Figure 5.31 Concrete gauges results of specimen SP4B

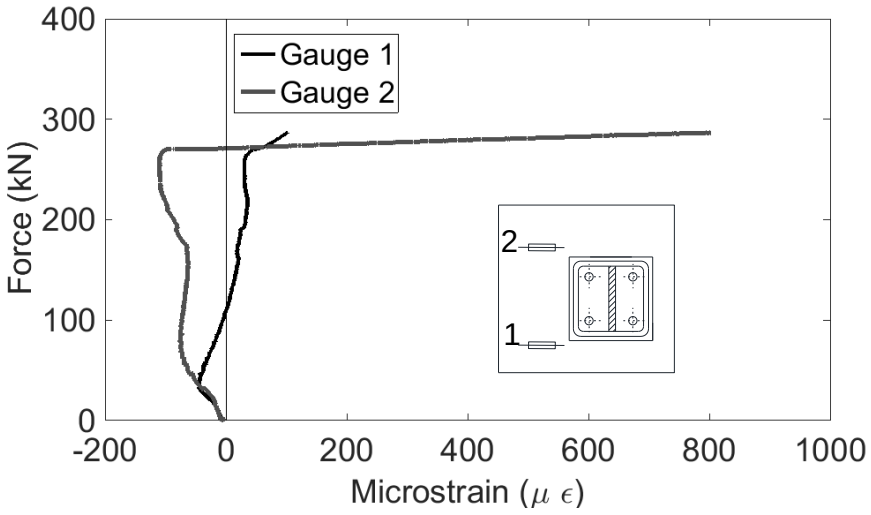

Figure 5.32 Concrete gauges results of specimen SP5

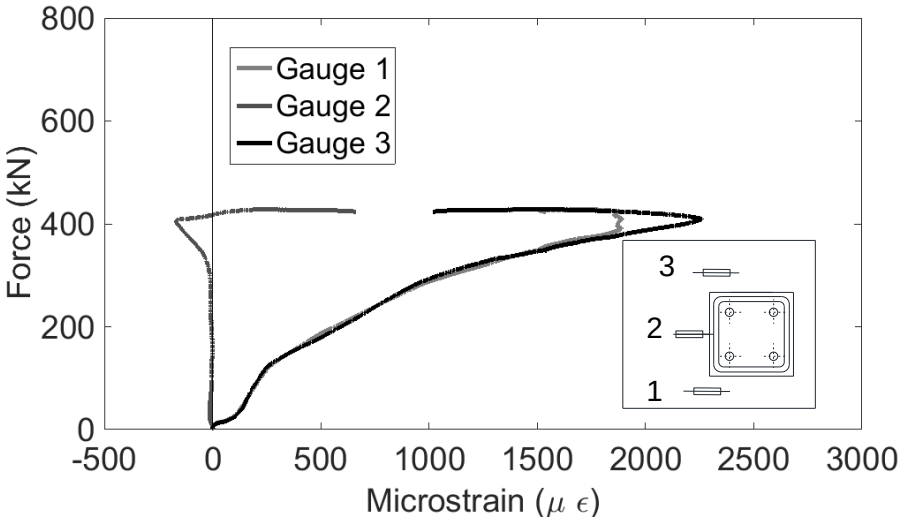

Figure 5.33 Concrete gauges results of specimen SP6

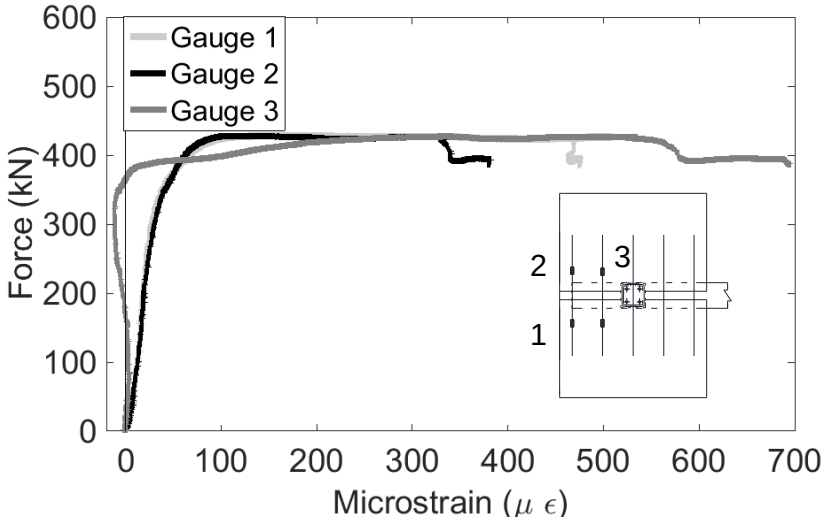

Figure 5.34 Steel gauges results of rebars of specimen SP6

Figure 5.34 show the recordings from the strain gauges installed on the steel rebars of the specimen SP6. The results showed that the strain rate of the rebars started increasing after the load reached 350 kN approximately and corresponding relative slip of 6.5 mm. The recorded strains increased rapidly from below 100 to more than 400 με as the load approached the failure load of the slab in shear cracking at 400 kN approximately. The stress developed in rebars was around 100 N/mm^2 while the yield strength of rebars was 500 N/mm^2. The result indicates that the transverse rebars contributed to the shear transfer mechanism, although they did not yield.

The results from the strain gauges installed on the YP's steel strips and walls were recorded until excessive deformation occurred which resulted in their removal. Figures 5.35-5.39 show the results of the strain gauges installed on the YP for the specimens SP1A, SP2B, SP3, SP4B and SP5 respectively. The exact position of each strain gauge is shown in the inset of each figure. Based on fundamental mechanics and taking into account modulus of Elasticity and yield strength obtained from the flat coupon tests, the theoretical yield strain is equal to 1900 με and 2500 με for the YP manufactured from the SHS tubes of 8 and 10 mm thickness respectively. Excessive strains developed up to 5000-5500 με at the top of the YP's steel strips and walls for all specimens apart from SP5. Gauge 1 of specimen SP2B installed on the top side of the steel strip was placed close to the neutral axis of the steel cross section and thus recorded almost zero strain. The YP of the specimen SP5 showed very little deformation at the end of the test. The recordings of the strain gauges installed on the YP indicated onset of yielding in the region where the gauge 1 was installed reaching strains of 2500 με.

The theoretical yield strain mentioned above cannot be obtained directly from the plots given since: 1) the strain gauges installed along the width of the steel strips instead of thickness and thus the recording strains will be lower than the values mentioned above, as shown in Figure 4.22 of chapter 4; and 2) the position of the strain gauges at the top of the steel strips and placed below the curved part of the steel strips does not necessarily correspond to the real position where the maximum strains should be recorded. The results are sensitive to the precise position of the gauge along the width of the steel strip and their primary installation is for FEM verification.

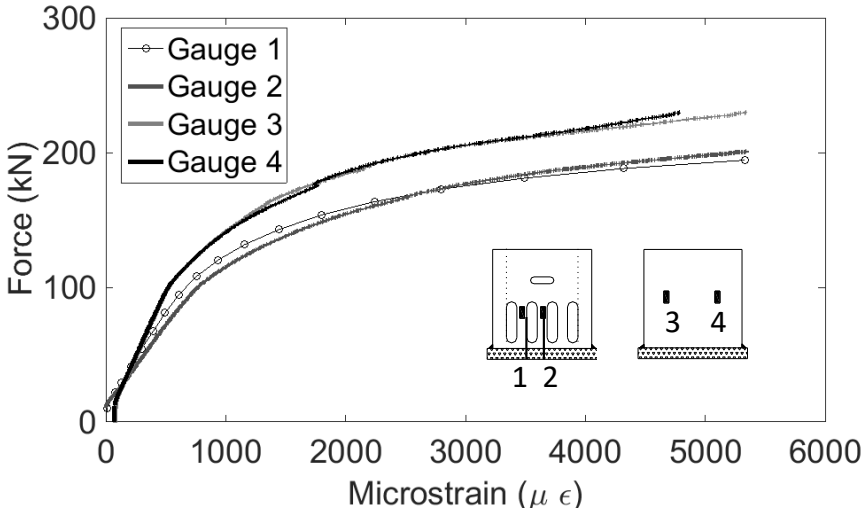

Figure 5.35 Steel gauges results of the YP of specimen SP1A

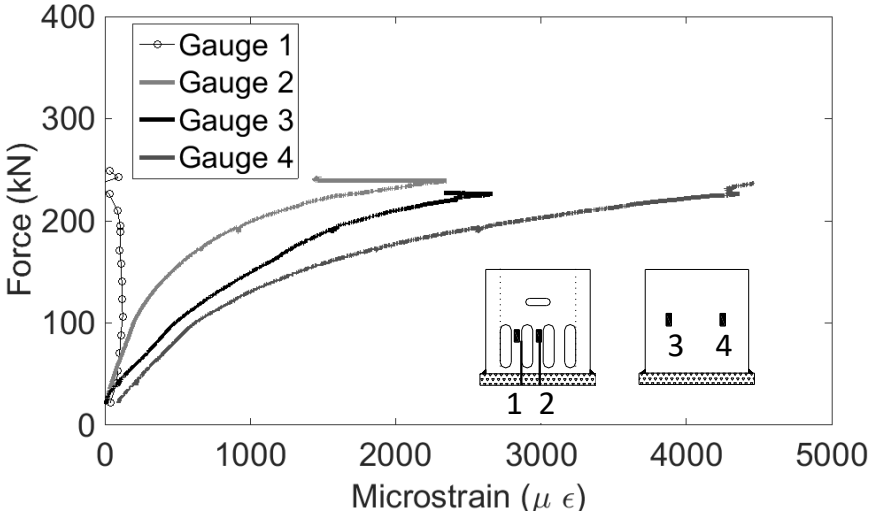

Figure 5.36 Steel gauges results of the YP of specimen SP2B

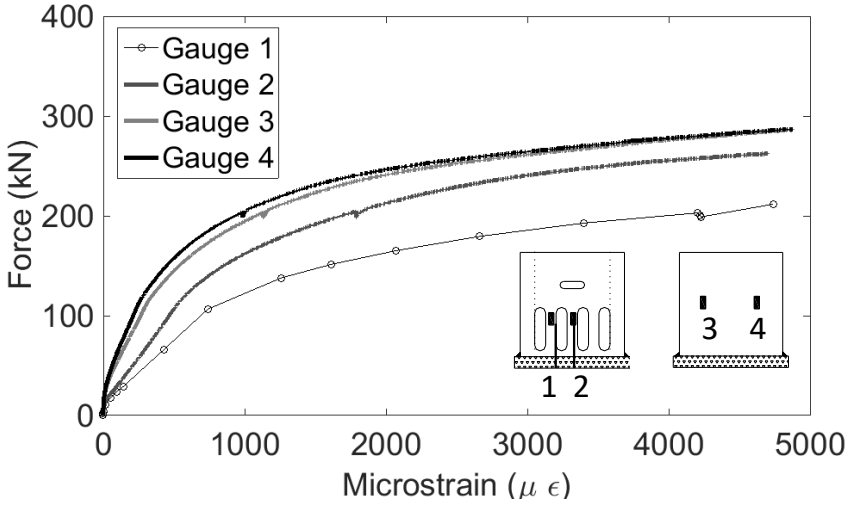

Figure 5.37 Steel gauges results of the YP of specimen SP3

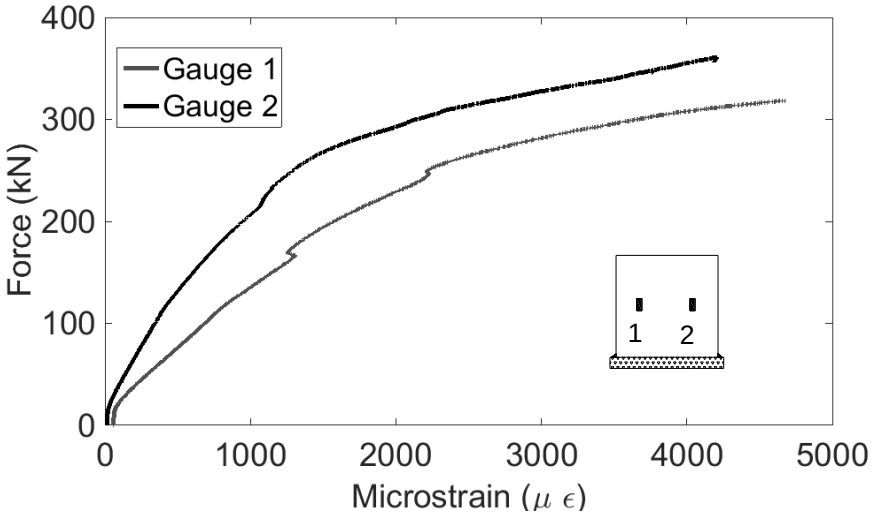

Figure 5.38 Steel gauges results of the YP of specimen SP4B

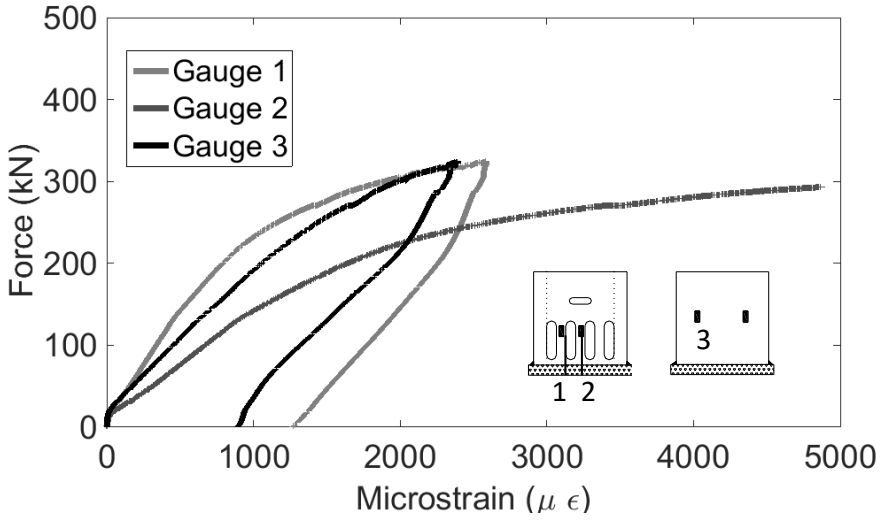

Figure 5.39 Steel gauges results of the YP of specimen SP5

5.8 Evaluation of Deconstruction and Reuse of Structural Components

The construction and deconstruction procedures of the proposed DSC were evaluated within the lab environment. The YPs were manufactured in the structural lab and all the other structural components, i.e. the steel section, the bolts and the HCUs, were delivered ready to be used. The cores of the HCUs located just before the YP in the direction of the loading was opened in the lab using concrete cutting blades. Once all the component parts of the proposed connection were ready to be used the assembly of the DSC was straightforward and fast. The construction was implemented by fixing the YP on the steel section using the four high strength bolts, placing the HCUs on the steel section and all the rebars in proper positions, placing the polythene foams to form the

concrete tooth and pouring *in situ* concrete to cover the open cores and the gaps around the YP.

The undamaged steel parts of the connection, i.e. the steel section and the bolts, were reused over and over again in all tests and no damage was seen in any test. The specimen SP1B was deconstructed after the end of the test and all the structural components including the slabs were reused in a new specimen, i.e. the specimen SP2A. The disassembly of the push out specimen SP1B was implemented by removing the concrete around the YP in two symmetrical rectangular regions of 13 by 45-cm through the depth of the slab. Concrete was removed from the region around the middle rebar. The concrete regions removed are shown in Figure 5.40. Cutting blades and conventional hammer were used to cut out and remove the concrete. After the concrete removal, the YP and the middle rebar were removed and a new YP and a middle rebar were placed at position. *In situ* concrete was poured to fill the regions shown in Figure 5.40a). It is noted that the deconstruction was implemented using the plain means provided by the lab, e.g. a smaller concrete region around the YP could be removed having proper means.

a) b)

Figure 5.40 Specimen SP2A a) before casting; and b) after casting

The deconstruction of one specimen and the reusability of all the undamaged structural components in a new test attempt to demonstrate the feasibility of additionally reusing the slabs (apart from the steel parts of the connection) without affection of the structural behaviour of the DSC; no damage in the slabs were seen during the second testing until the excessive slip of 35 mm.

Since a limited number of researchers dealt with the deconstruction procedure, a brief review is herein reported in order to compare the various methods for deconstruction. Moynihan and Allwood [5.6] used modified threaded studs with washers and nuts which were placed at the bottom and top flange of the steel section. The bolts were embedded in *in situ* concrete slabs formed in profiled steel decking. Oversized holes of 24 mm were drilled in the top flange of the steel section in order to facilitate the deconstruction procedure. The researchers tested the concept of deconstruction by loading up to service, unloosening the nuts which were placed at the bottom side of the steel section and thus removing the slab as a whole part with the bolts inside, and then re-attaching the slab to the steel section. The concrete slab including the bolts was lifted 10 mm above the steel section upon the deconstruction of the composite beam. Ataei et al. [5.7] used tensioned friction grip bolts with washers and nuts placed at the bottom side of the steel section in conjunction with geopolymer precast slab units. The bolts were not embedded in the concrete slabs and thus the deconstruction procedure was facilitated by working only from the top side of the beam. They tested the concept of deconstruction by loading up to service, removing one precast slab unit with the aid of cranes and then reattaching the slab unit to the steel section and further loading up to failure. They did not observe any damage to the bolts during service loading. They concluded that the steel concrete composite connection can be successfully deconstructed. Suwaed and Karavasilis in [5.8] designed an innovative deconstructable connection for use in rapid disassembly precast bridges. This demountable connection compared to those previously presented includes special locking nuts and conical precast plugs so that the slab can be separated from the steel section in different ways. Upon deconstructing the system, the bolts can be either removed together with the concrete slab or remained tightened on the steel section and thus removing the slab only. The connection is versatile since the substitution of the bolts is easily allowed in case that replacement of the shear connectors is needed. The latter is achieved by removing the bolts together with a small part of grout that has been previously poured onto the connection to fill the gaps during the construction stage. Therefore the deconstruction of the composite connection is further simplified since there is no need of lifting up the deck of the bridge.

5.9 Summary

The performance of the YP shear connectors used in combination with HCUs was investigated through twelve full scale horizontal push out tests. The use of innovative blind bolts to fix the YP on the top flange of the steel section did not benefit the structural behaviour of the proposed connection based on the first two tests belonging to the group SP0. Therefore, high strength allen bolts were used in the subsequent ten tests belonging to the group SP1-SP4. The 4^{th} of the HCUs located just before the YP in the direction of the loading applied, was full of *in situ* concrete to ensure the transfer of the shear stresses from the YP to the concrete and to avoid early shear cracking of the slabs. The results showed that the YP can provide high shear resistance and very high slip capacity, if properly designed. The yield strength of the YP achieved in tests was in the range of 170-320 kN and the maximum force obtained was 250-427 kN. The slip capacity achieved in tests was at least 30 mm for the specimens designed to have the ductile failure mode. The slip capacity of the two specimens exhibited shear cracking in tests, i.e. SP5 and SP6, was 8.3 and 19.6 mm respectively, which is higher than 6 mm specified by Eurocode 4 for ductile shear connectors. In terms of stiffness the YP achieved 75-135 kN/mm, depending on the selected geometric properties of the YP. To avoid reduction of the shear resistance and stiffness resulted by the out of bending deformation of the YP, adequate amount of *in situ* concrete should be placed around the corners of the YP. The simplified equations proposed based on plastic beam analysis accurately predicted the yield strength of the YP. Among other potential failures of the concrete slab (i.e. ripping, splitting and shear cracking), the shear cracking was found to be critical for the slabs of the push out specimens tested in the present research work. The shear resistance of the concrete component was reasonably predicted by the shear friction model recommended in Eurocode 2 [5.4]. The uplift measured for the specimens SP1A and SP6 was found to be within the specified limits imposed by Eurocode 4 [5.5]. The deconstruction procedure and the feasibility of reusing the structural components were evaluated within the lab environment. All the steel structural components apart from the YP were fully reusable at the end of the test. The steel structural components were reused over and over again. The slabs of one specimen tested were additionally reused in a new specimen designed to have the ductile failure mode and no concrete failure of the slabs was observed after the second testing. The means and the method of deconstruction could be optimized so as to

remove the minimum area of concrete around the YP upon deconstruction of the structural system.

5.10 Reference List

[5.1] A. Zona, G. Ranzi, *Shear connection slip demand in composite steel-concrete beams with solid slabs*, J. Constr. Steel Res., 102, 266-281 (2014)

[5.2] British Standard Institution (BSI). BS EN 1994-1-1: 2004. Design of composite steel and concrete structures, Part 1.1: General rules and rules for buildings, London , UK (2004)

[5.3] D. Lam, K.S. Elliot, D.A. Nethercot, *Push-off Tests on Shear Studs with Hollow-cored Floor Slabs*, The Structural Engineer, 76(9), 167-174 (1998)

[5.4] British Standard Institution (BSI). BS EN 1992-1-1 - Eurocode 2 - Design of concrete structures - Part 1-1: General rules and rules for buildings, London, UK (1992)

[5.5] British Standard Institution (BSI). BS EN 1991-1-1:2004. Design of composite steel and concrete structures, Part 1.1: General rules and rules for buildings, London, UK (2004)

[5.6] C. Moynihan, J.M. Allwood, *Viability and performance of demountable composite connectors*, J. Constr. Steel Res., 88, 47-56 (2014)

[5.7] A. Ataei, M.A. Bradford, X. Liu, *Experimental study of composite beams having a precast geopolymer concrete slab and deconstructable bolted shear connectors*, J. Eng. Struct., 114, 1–13 (2016)

[5.8] Ahmed S.H. Suwaed, Theodore L. Karavasilis, *Novel Demountable Shear Connector for Accelerated Disassembly, Repair, or Replacement of Precast Steel-Concrete Composite Bridges*, J. Bridge Eng., 22(9), 04017052 (2017)

Chapter 6-FEM Analyses

6.1 Introduction

Three dimensional non-linear numerical models for six push out specimens were developed to verify the experimental results using the Abaqus Standard software (v.14). The numerical models were developed for the specimens SP1A, SP2B, SP3, SP4B, SP5 and SP6. The numerical models for the push out specimens involved a number of non-linearities including material, geometric and contact ones. The FEM models aimed at predicting the force-slip behaviour of the push out specimens and the development of strains recorded by the strain gauges installed on the steel parts. The maximum and minimum principal stress vectors for the concrete component were extracted and presented. The maximum tensile stresses developed in the rebars were extracted and presented.

6.2 Model Definition

6.2.1 Geometry, Boundary Conditions and Mesh Type

The FEM models included all the structural components, i.e. the slabs composed of the HCUs, the *in situ* concrete cores, the concrete tooth, the steel section, the YP, the bolts and the rebars. Each structural part included a number of partitions to avoid concentrations of multiple constraints in joined interacting edges or surfaces. Figure 6.1 shows the model of a typical push out specimen. One half of the steel section was modelled due to symmetry. Fully fixed boundary conditions were assigned to the right end of the steel section at the side 'A', as shown in Figure 6.1. Symmetric boundary conditions were assigned to the web of the half steel section. The slabs were restrained along the XX' axis. Uniform distributed displacement as horizontal shear was applied at the side 'B' showing in Figure 6.1.

Three dimensional 8-node linear brick elements with reduced integration (C3D8R) were used for the HCUs, the *in situ* concrete cores, the concrete tooth, the steel section, the bolts and the YP apart from some small regions located close to the corners of YP where three dimensional 6-node linear triangular prisms were used (C3D6). An overall mesh of 30 mm was adopted for the steel section with mesh refinement between 7-15 mm in the regions close to the drilled holes of the steel section where the bolts were

placed. A refine overall mesh of 5-7 mm and 3.5 mm was adopted for the YP and the bolts respectively. Figure 6.2 shows the typical mesh of the concrete components of the numerical models. Figure 6.3 shows the typical mesh of the steel section, the YP and the bolts of the numerical models. A mesh of 15-20 mm was utilized for the *in situ* concrete cores, the concrete tooth and the HCUs. A coarse mesh of 100 mm was adopted for the region of the HCUs away from the YP Three dimensional two node truss elements (T3D2) were used to simulate the rebars and the mesh was 15 mm. Figure 6.4 show the typical mesh of the rebars.

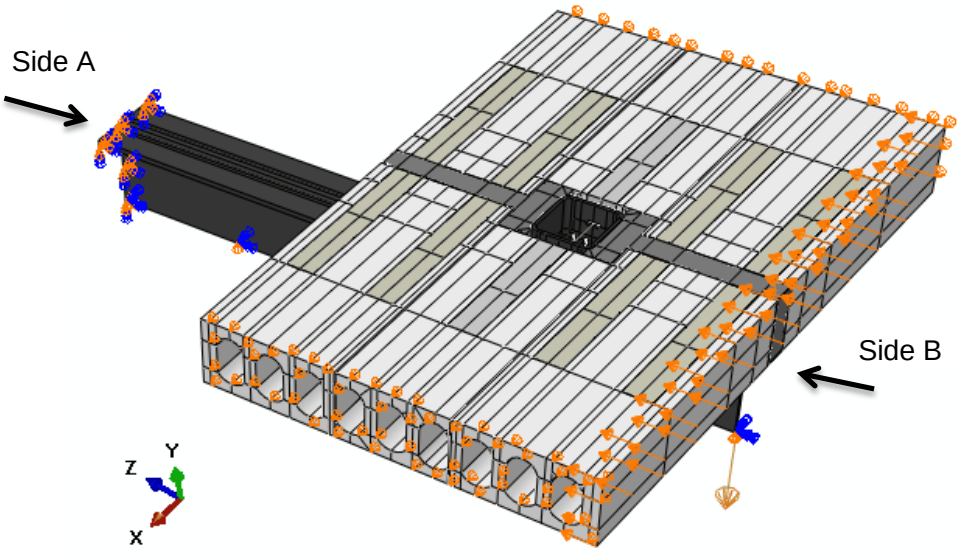

Figure 6.1 Typical model definition of a numerical push out specimen

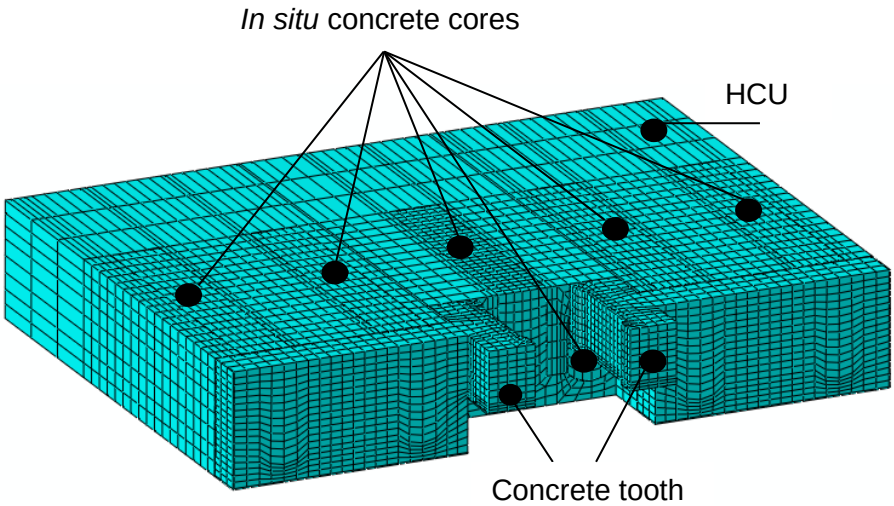

Figure 6.2 Typical mesh of concrete structural components of a numerical model

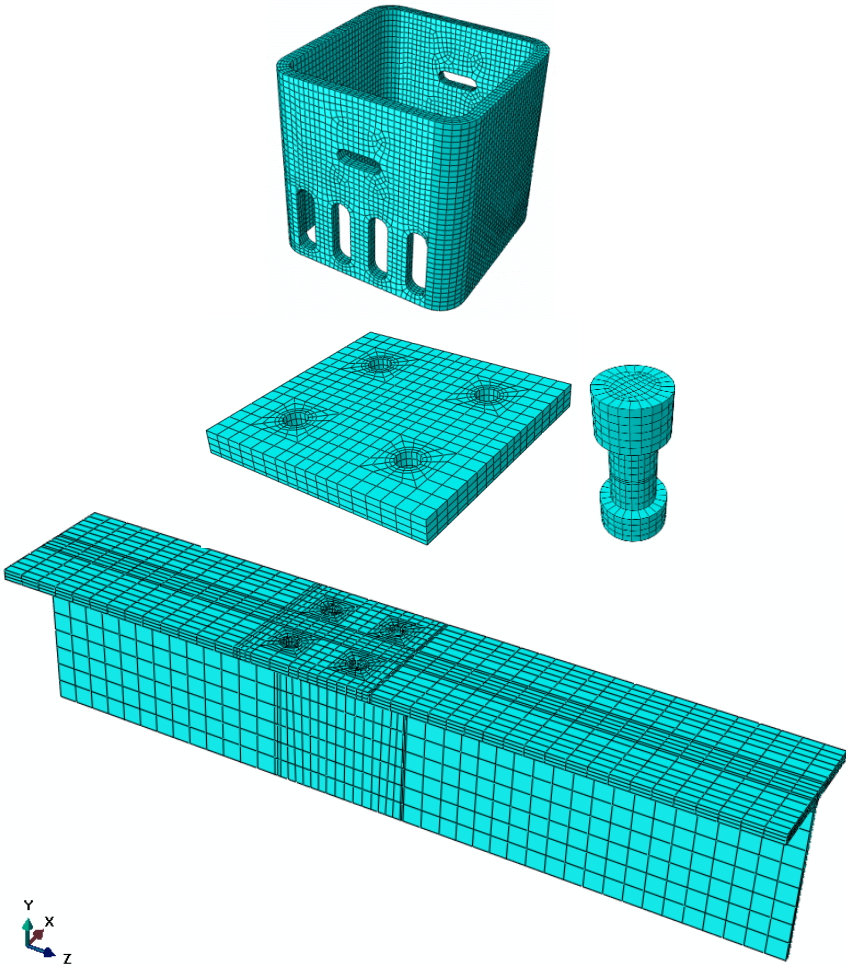

Figure 6.3 Typical mesh of steel structural components of a numerical model

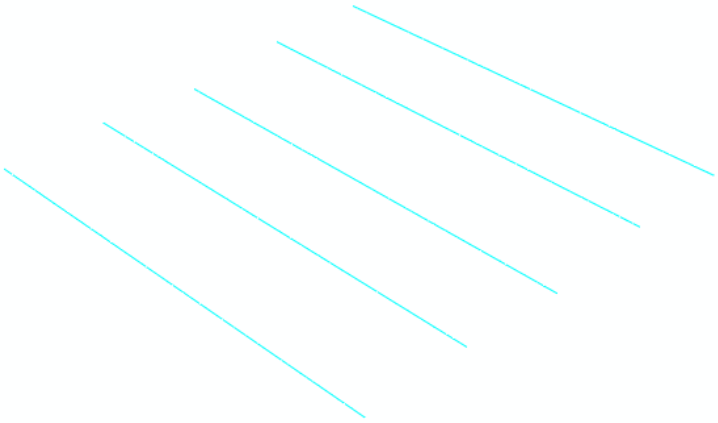

Figure 6.4 Reinforcement bars using T3D2 elements

6.2.2 Interaction

A number of contact pairs were defined between steel and steel, concrete and concrete and steel and concrete surfaces interacting with each other. Hard contact and penalty friction formulation were used to describe the normal and the tangential behaviour of each contact pair. The friction coefficient was considered 0.30 for the steel to steel and concrete to steel interacting interfaces and 0.5 for the concrete to concrete interacting interfaces according to [6.1, 6.2] and [6.3] respectively. Similar coefficients of friction have been used by other researchers working on numerical models in demountable steel concrete composite connections [6.4, 6.5]. The finite sliding formulation with surface to surface discretization was applied for all the contact pairs apart from the contact surface between the concrete slab and the steel section, where the node-to-surface discretization was employed. The surface smoothing technique was used for the circular contact surfaces between the drilled holes of the steel section and the steel base of the YP in contact with the bolts to facilitate analysis convergence. Tie constrains were enforced between the steel base of the YP placed at the bottom and the YP, simulating the welding. Tie constraints were enforced between the *in situ* concrete cores of the HCUs and the HCUs. Embedment constraint was enforced between the rebars and the *in situ* concrete cores.

6.3 Materials

6.3.1 Steel

The poisons' ratio for all the steel members was typically considered equal to 0.3. The density for all the steel materials was typically considered equal to 7.85×10^{-9} tn/mm^3. The elastic and plastic behaviour of the YP's material were defined according to the results taken from the flat part of the coupon tests. The modulus of Elasticity E_s was taken equal to 193600 N/mm^2 and 202850 N/mm^2 for the tube of 8 and 10 mm respectively. The engineering stress-strain curves of the coupon specimens taken from the SHS tubes of 8 and 10 mm thickness were averaged. The average true stress-strain curve was obtained from the average engineering one using equations (24) and (25) for the SHS tubes of 8 and 10 mm thickness. The true stresses and strains were determined by:

$$\sigma_{true} = \sigma * (1 + \epsilon_p) \quad (24)$$

$$\varepsilon_{pl,true} = \ln(1 + \epsilon_p) - \frac{\sigma_{true}}{E_s} \quad (25)$$

, where σ is the engineering stress, ϵ_p is the engineering plastic strain and E_s is the initial modulus of Elasticity of the tubes' material.

Equations (24) and (25) are valid provided that the deformation along the gauge length is uniform. The engineering stress is defined as the force taken from the tensile testing machine divided by the nominal (original) cross section area of the coupon specimen. The true stress is defined as the force taken from the tensile testing machine divided by the instantaneous cross section area of the coupon specimen which changes during the experiment. The formulation of equation (24) is based on the assumption that the volume along the gauge length remains constant during the plastic deformation of the specimen. Therefore, it is assumed that $A\ L = A_0\ L_0$, where A and L are the instantaneous cross section area and gauge length respectively and A_0 and L_0 are the nominal cross section area and gauge length respectively of the coupon specimen [6.6]. The true strains can be found by integrating the incremental change in length dL divided by the length L. At low strains, the engineering stress-strain curve and the true one shows no significant difference between them. At high strains, a neck starts to form, the area along the gauge length is not uniform anymore and the force taken from the tensile testing machine starts decreasing. Thus, the equations (24) and (25) can be used up to the onset of the necking. Beyond this point, the true stress may be defined using the measured area of the cross section at the base of the neck and the strains should be accordingly calculated. The average plastic engineering stress-strain curves and the true ones for the SHS tubes of 8 mm and 10 mm thickness are shown in Figures 6.5 and 6.6 respectively.

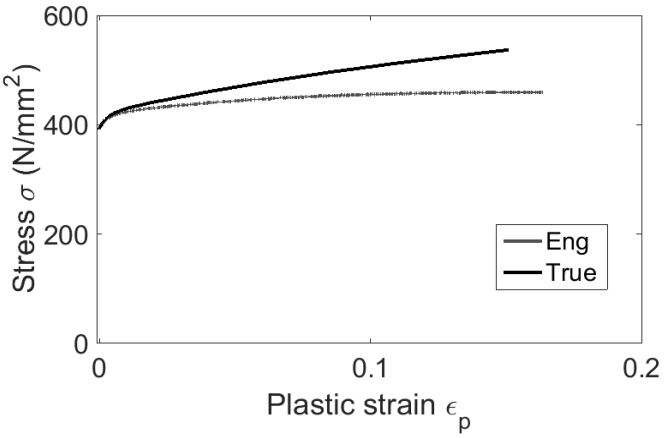

Figure 6.5 Plastic engineering and true stress-strain curve of SHS180x180x8 tube

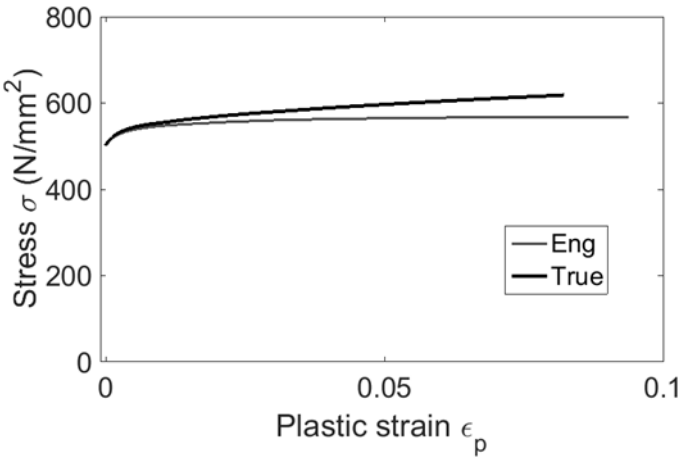

Figure 6.6 Plastic engineering and true stress-strain curve of SHS180x180x10 tube

The yield strength of the materials of the other steel structural parts of the connection was taken into account based on the structural grade of each. Thus, the yield strength of the steel plate welded at the bottom of the YP was assumed equal to 275 N/mm^2 and the one of the steel section was assumed equal to 355 N/mm^2, while the yield strength of the bolts was taken equal to 1100 N/mm^2.

The stress-strain behaviour of the rebars' material was taken into account as a bilinear curve based on the results obtained from the uniaxial tensile tests presented in paragraph 4.3.1. The stress-strain relationship is linear up to the yielding point followed by the plastic plateau stage. The behaviour of the steel material in tension was considered identical to the behaviour of the steel material in compression.

6.3.2 Concrete

The behaviour of the concrete component was simulated using the concrete damage plasticity model provided by the Abaqus software [6.7]. A typical plasticity model requires the definition of the yield surfaces that bound the elastic domain, the flow rules that define the evolution of a number of internal variables and the hardening function which determine the evolution of the yield surfaces. The plasticity model used by the Abaqus is designed for reinforced concrete and it can be used for plain concrete too. The model considers isotropic stiffness degradation and isotropic compressive and tensile plasticity to capture the response of the concrete. The input is given in terms of uniaxial compression and tension.

The yield surface or the yield criterion requires the definition of two parameters, i.e. the coefficient K_c, and the ratio $f_{b'}/f_c$. The former is the tensile to the compressive meridian ratio and controls the shape of the yield surface in the deviatoric plane and the latter is the compressive strength of the concrete under biaxial loading divided by the compressive strength of the concrete under uniaxial loading. Abaqus software utilizes the failure criterion defined by Lubliner et al. [6.8] and modified by Lee and Fenves [6.9]. The yield criterion is defined by:

$$F = \frac{1}{1-a}\left(\bar{q} - 3a\bar{p} + \beta\left(\overline{\varepsilon^{pl}}\right)\langle\overline{\hat{\sigma}_{max}}\rangle - \gamma\langle\overline{\hat{\sigma}_{max}}\rangle\right) - \bar{\sigma}_c\left(\overline{\varepsilon_c^{pl}}\right) = 0 \tag{26}$$

, where:

$$a = \frac{\left(\frac{f_{b'}}{f_c}\right) - 1}{2\left(\frac{f_{b'}}{f_c}\right) - 1};\ 0 \le a \le 0.5 \tag{27}$$

$$\beta = \frac{\bar{\sigma}_c\left(\overline{\varepsilon_c^{pl}}\right)}{\bar{\sigma}_t\left(\overline{\varepsilon_t^{pl}}\right)}(1-a) - (1+a) \tag{28}$$

$$\gamma = \frac{3(1-K_c)}{2K_c - 1} \tag{29}$$

, where $\overline{\hat{\sigma}_{max}}$ is the maximum principle effective stress, $\bar{\sigma}_t(\overline{\varepsilon_t^{pl}})$ is the effective cohesion stress and $\bar{\sigma}_c(\overline{\varepsilon_c^{pl}})$ is the effective compressive cohesion stress.

The flow potential function, G, requires the identification of two parameters, i.e. the eccentricity, ϵ, and the dilation angle, ψ. The flow rules define the material state through a set of internal variables the most important of those is the plastic strain rate which determine the orientation of the plastic strain. Non-associated plastic flow is considered and the potential hyperbolic function of the Drucker-Prager criterion is utilized found in [6.7]. The term non-associated means that the plastic strain vector is normal to the plastic potential function. The potential function is given by:

$$G = \sqrt{(\epsilon f_t \tan\psi)^2 + \overline{q^2}} - \bar{p}\tan\psi \quad (30)$$

, where f_t is the uniaxial tensile stress at failure and $\bar{p}$ and $\bar{q}$ are the hydrostatic and the Mises equivalent effective stress respectively [6.7].

Figure 6.7 shows typical yield surfaces on the deviatoric plane considering various shapes (image taken from [6.7]). The vector of the plastic strain rate, $d\epsilon_p$, is vertical to the yield surface. Figure 6.8 shows the eccentricity and the dilation angle in p-q plane (image taken from [6.10]).

The identification of the four plasticity parameters as previously defined requires a number of lab tests including uniaxial compression tests, uniaxial tension tests, biaxial compression tests and triaxial tests. Since the performance of these experiments is out of the scope of the present research thesis, the plasticity parameters used in the numerical models are justified by available experimental and numerical results found in literature review. Jankowiak and Lodygowski [6.11] identified the plasticity parameters for a concrete cylindrical strength of 50 N/mm^2. The researchers did not identify the parameter K_c since they did not have results from full triaxial tests. The researchers discussed the procedures needed to identify the plasticity parameters using experimental stress-strain curves taken for uniaxial compression tests, uniaxial tension tests, triaxial compression tests including hydrostatic pressures of 6.9 and 13.8 N/mm^2 and the Kupfer's curve [6.12] for biaxial plane stress. They measured the dilation angle equal to 38° in p-q plane. Their results were used to model the plastic behaviour of the concrete material in beams subjected to three and four point bending and good correlation was found between experimental and numerical results. This value for the dilation angle is in good correlation with the one used by Sümer and Aktaş [6.13] who conducted sensitivity analysis in concrete beams subjected to two point loading of 33 N/mm^2 concrete cylindrical strength. Similar value for the dilation angle was used by Pavlovic et al. [6.14] and Prakash et al. [6.15].

The dilation angle was taken equal to 38 according to [6.11, 6.13] for all the push out numerical models. The eccentricity was taken equal to 0.10 according to [6.7]. The ratios K_c and $f_{b'}/f_c$ were determined according to the prediction proposed by Lim et al. [6.16] which associated the above ratios with the unconfined uniaxial compressive strength f_c of concrete defining by:

$$K_c = 0.71 f_c^{-0.025} \tag{31}$$

$$\frac{f_{b\prime}}{f_c} = 1.57 f_c^{-0.09} \tag{32}$$

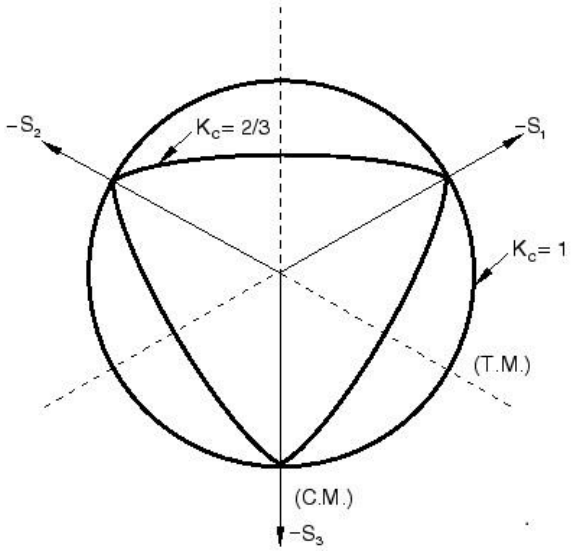

Figure 6.7 Typical yield surfaces [6.7]

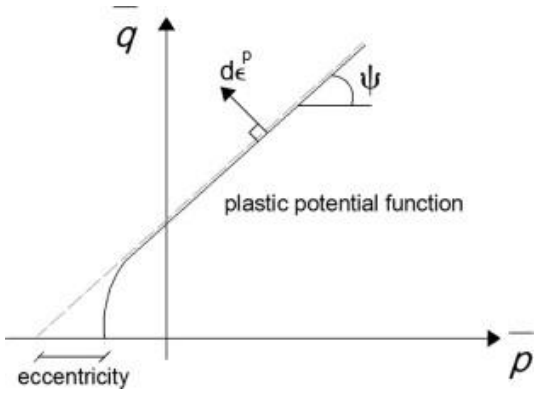

Figure 6.8 Dilation angle and eccentricity in meridian plane [6.10]

The uniaxial compressive stress-strain behaviour of concrete was determined according to the prediction of Eurocode 2 [6.17]. The stress-strain behaviour is given by:

$$\frac{\sigma_c}{f_c} = \frac{k n_1 - {n_1}^2}{1 + (k-2) n_1} \tag{33}$$

, where n is equal to $n_1 = \epsilon_c / \epsilon_{c1}$, k is equal to 1.05 E_{cm} $|\epsilon_{c1}|/f_c$, E_{cm} is the modulus of Elasticity and ϵ_{c1} is the strain at peak stress according to Table 3.1 of Eurocode 2 [6.17].

The ultimate strain of the concrete, ϵ_{cu}, is taken equal to 0.0035. Figure 6.9 shows the uniaxial stress-strain compressive behaviour of the concrete according to [6.17]. The modulus of Elasticity is associated with the uniaxial compressive strength of concrete in N/mm^2 and it is given by:

$$E_{cm} = 22[f_c/10]^{0.3} \tag{34}$$

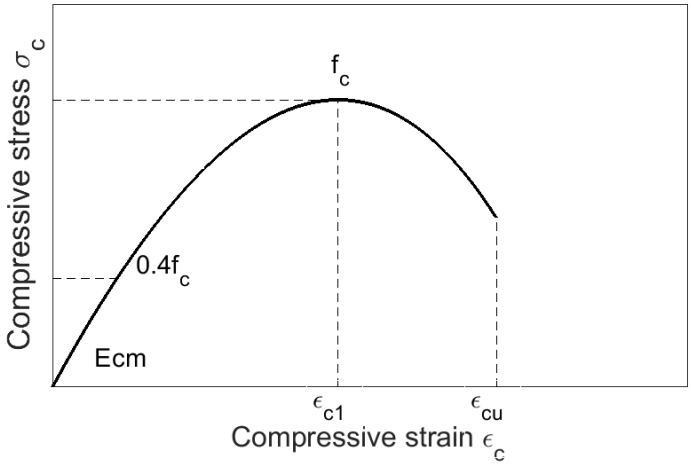

Figure 6.9 Uniaxial compressive behaviour of concrete according to [6.17]

The uniaxial tensile stress-strain behaviour of concrete was simulated as linear stress-strain behaviour. After cracking of concrete the stress reduces linearly to zero. The value of the strain, ϵ_{tu}, when the stress is equal to zero is taken 10 times the strain at cracking, ϵ_{tp}, as recommended by the Abaqus manual [6.7]. The modulus of Elasticity in tension is taken equal to the modulus of Elasticity in compression. Figure 6.10 shows the uniaxial tensile behaviour of the concrete assumed.

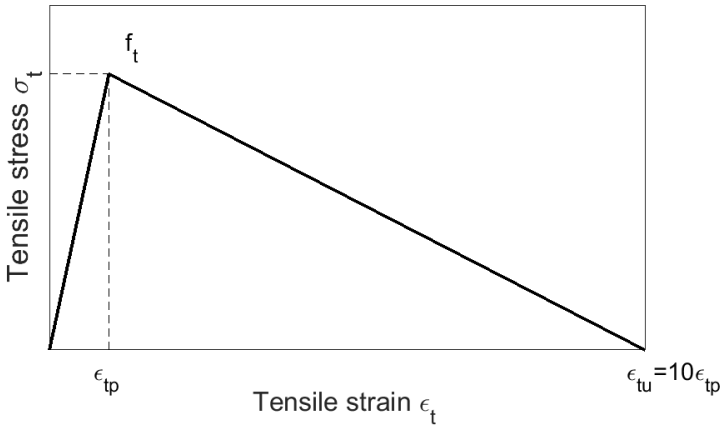

Figure 6.10 Uniaxial tensile behaviour of concrete

6.4 Steps and Analysis Type

The analysis is divided in three steps. The first step included the contact interaction to avoid numerical problems. The second step included the gravity loads. The displacement was applied during the third step of the analysis. Automatic stabilization technique with constant damping factor was utilized in the third step of the analysis to deal with unstable non- linear behaviour during the first increment of the analysis. The damping factor was found using trial and error procedure so as to be small enough in order to minimize the influence of viscous forces introduced to the global equilibrium equations on the results. The damping factor was found to be equal to 10^{-6}, after comparing the ratio of energy dissipated by viscous damping (ALLSD) to the total strain energy (ALLIE). This ratio should be smaller than 5% to ensure accuracy of solution as suggested by Abaqus manual [6.7]. Static general procedure was utilized for all the steps. The minimum incremental step was chosen equal to 0.05 and the maximum equal to 1. The maximum increments were set equal to 300 for the third step of the analysis.

6.5 FEM Results and Discussion

The numerical results extracted by the Abaqus software are the force-slip behaviour, the maximum and minimum principal stress vectors of the concrete slabs, the development of strains in the positions where the steel gauges were installed on the steel parts and are presented in force-microstrain graphs, and the tensile stresses developed in the two rebars located just before the YP in the direction of the loading at the end of each analysis. The numerical results were extracted from the Abaqus output file for the specimens SP1A, SP2B, SP3, SP4B, SP5 and SP6.

6.5.1 Discussion about the Failure Modes

Since the numerical models involved a number of materials and complex contact non – linearities the Standard solver was proved too slow to obtain numerical solutions and frequently the solution was diverged. For this reason the behaviour of the numerical models designed to have the ductile failure mode was investigated up to the slip of 30-35 mm which corresponds to the maximum experimental slip achieved in all tests apart from the test SP1A. The numerical solution for the test SP5 was obtained up to 5.4 mm of slip for the same reason. The stress condition of the concrete slabs was investigated

by extracting the minimum and maximum principal stress vectors and the equivalent plastic strains. The stress vectors are plotted for one of the two sides of the concrete slab due to the longitudinal symmetry of the specimens and for the concrete part found between the YP and the ends of the slabs on which the displacement was applied, as shown in Figure 6.11.

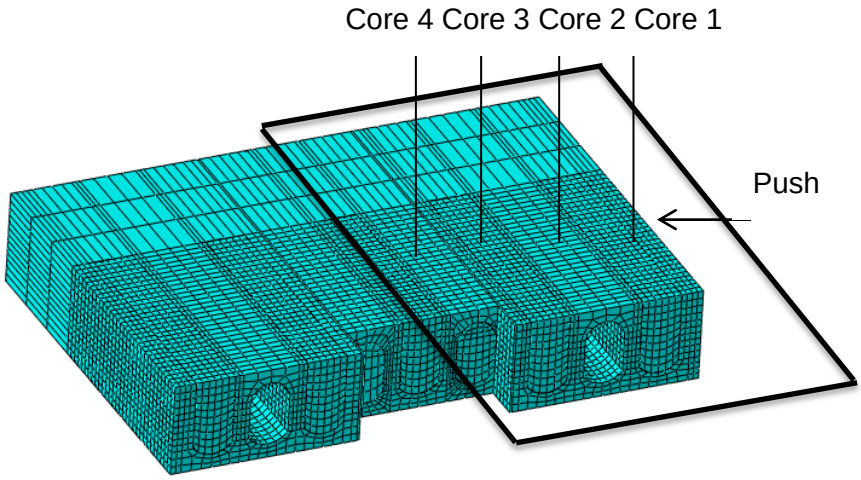

Figure 6.11 Part of concrete slab where the stress vectors were extracted

Plastic strains were concentrated at the ends of the steel strips and vertical walls of the YPs of the numerical models developed for the push out specimens SP1A, SP2B, SP3 and SP4B. Figure 6.12 shows indicatively the contour plot of the equivalent plastic strain (PEEQ) of the YP for the numerical model SP3 at the end of the analysis at 35 mm of relative slip. The excessive deformation of the YPs of the numerical models verifies the ductile failure mode obtained from the tests.

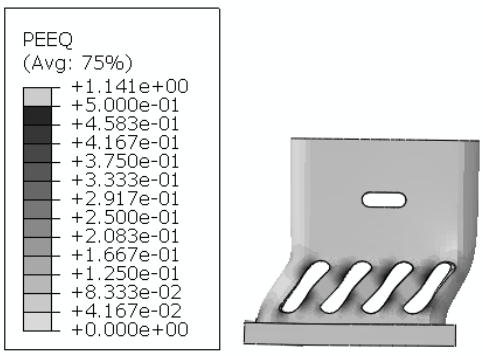

Figure 6.12 Contour plot of YP (PEEQ) for the numerical model SP3

Figures 6.13-6.16 show the minimum principal stress vectors developed in the part of the concrete slab shown in Figure 6.11 for the specimens SP1A, SP2B, SP3 and SP4B respectively. The diagonally developed compressive stress field shown in Figures 6.13-

6.16 reaches maximum values of around 10 N/mm^2 in the region close to the YP and gradually reduces its values till the ends of the slab up to 1 N/mm^2. Although slightly different values of compressive stresses are obtained from specimen to specimen, the compressive stress field developed in the slabs of each numerical model is small. The maximum compressive stress values shown in the legends of Figures 6.13-6.16 belong only to individual finite elements found close to the corner of the slab. The maximum principal compressive stresses developed out of the region of the fully filled cores of the HCU with *in situ* concrete are equal to 1-2 N/mm^2 indicating that the width of the maximum principal compressive stress field taking into account both sides of the slabs is around 1000 mm.

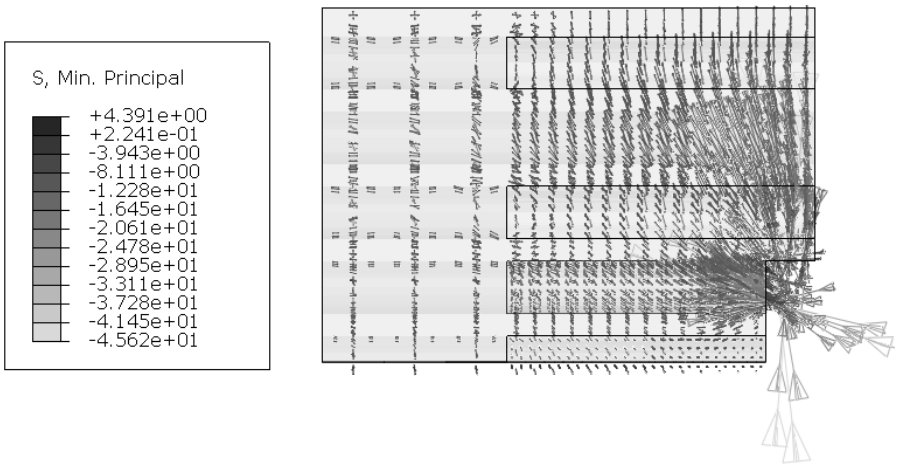

Figure 6.13 Minimum principal stress vectors for the slab of the model SP1A

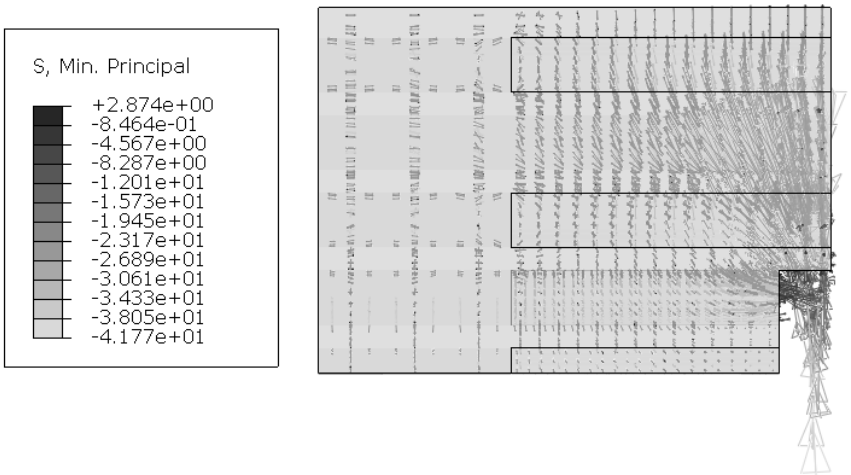

Figure 6.14 Minimum principal stress vectors for the slab of the model SP2B

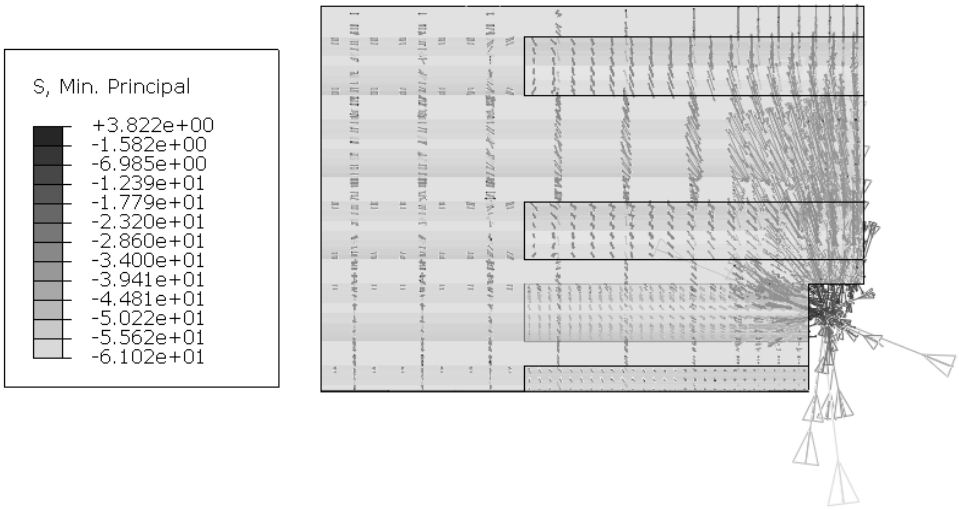

Figure 6.15 Minimum principal stress vectors for the slab of the model SP3

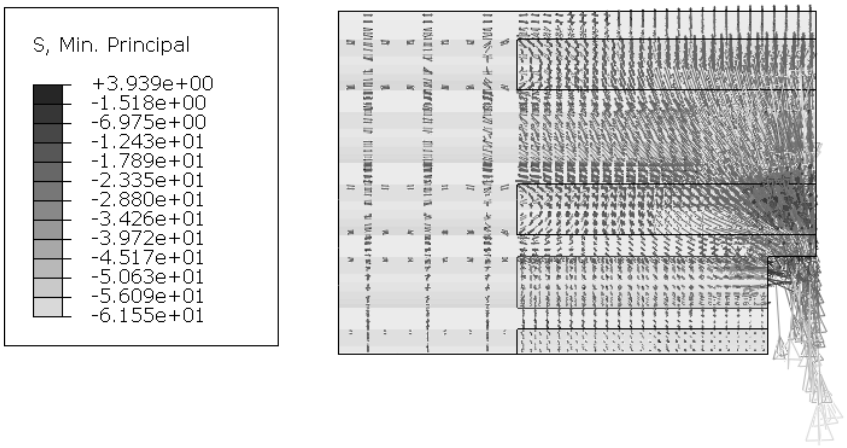

Figure 6.16 Minimum principal stress vectors for the slab of the model SP4B

Figures 6.17-6.20 show the maximum principal stress vectors developed in the part of the concrete slab shown in Figure 6.11 for the specimens SP1A, SP2B, SP3 and SP4B respectively. The direction of the maximum principal tensile stresses between the 3rd and the 4th core of the HCU is diagonal, as shown in Figures 6.17-6.20. The maximum principal tensile stresses developed between the 3rd and the 4th core of the HCU are within the range of 1.5-2 N/mm^2 in these specimens. The principal tensile stresses developed in the other regions of the slab are smaller apart from few elements close to the corner of the slabs at which the tensile stresses are maximized. The equivalent uniaxial tensile strength of the *in situ* concrete used in specimens SP1A, SP2B, SP3 and SP4B is 3.9, 3.2, 2.3 and 2.5 respectively which indicates that the tensile stresses developed in the slabs do not exceed the tensile strength of the *in situ* concrete. The maximum principle tensile stresses developed in these specimens are not high enough

and are not extended enough in adjacent regions to cause tensile failures.

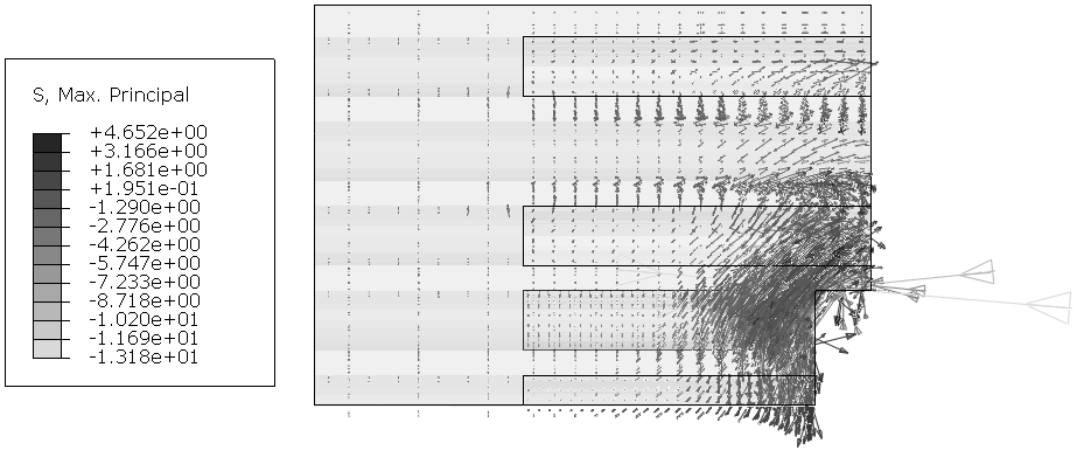

Figure 6.17 Maximum principal stress vectors for the slab of the model SP1A

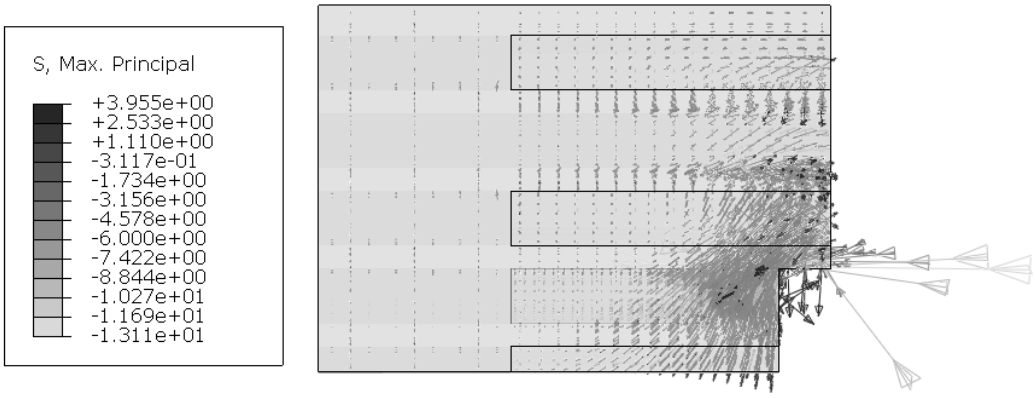

Figure 6.18 Maximum principal stress vectors for the slab of the model SP2B

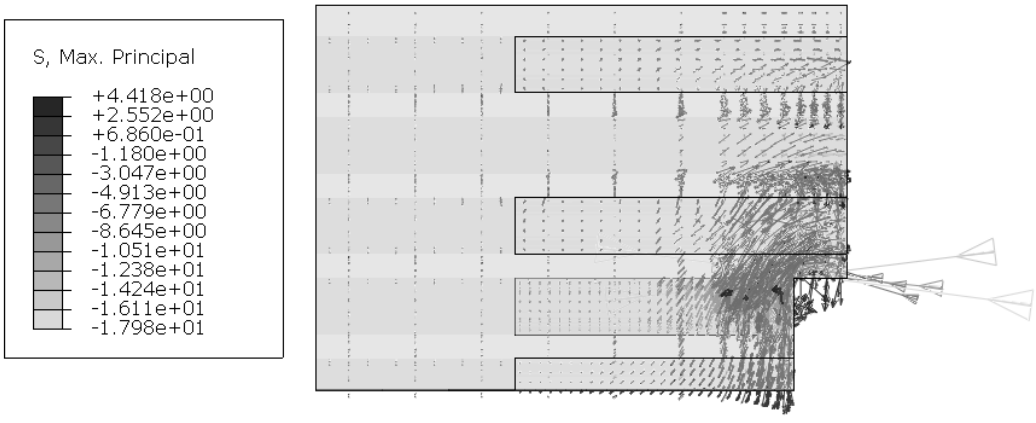

Figure 6.19 Maximum principal stress vectors for the slab of the model SP3

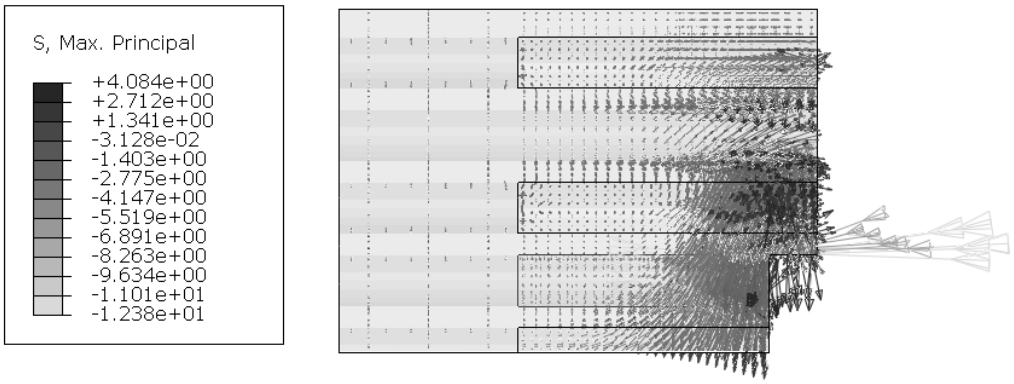

Figure 6.20 Maximum principal stress vectors for the slab of the model SP4B

Figure 6.21 shows the contour plot of the equivalent plastic strain (PEEQ) of the YP for the numerical model SP5 at the end of the analysis corresponding to 5.4 mm of relative slip. The contour plot indicates onset of yielding at the ends of the steel strips. Figures 6.22 and 6.23 show the minimum and maximum principal stress vectors respectively for the slab of the numerical model SP5. Similarly to the other specimens, the principal compressive stress field developed is small and the stresses developed in the slab are within the range of 3-15 N/mm^2. The maximum principal tensile stresses developed between the 3rd and the 4th core of the HCU are around 1.7-2 N/mm^2 which are very close to the tensile strength of the *in situ* concrete used equal to 1.9 N/mm^2. Figure 6.24 shows the contour plot of the equivalent plastic strain (PEEQ) of the slab of the numerical model SP5. The maximum plastic strains are concentrated between the third and the fourth core of the HCUs in the direction of the loading. The maximum plastic strain developed is equal to 1.87 10^{-3}. The numerical model developed for the specimen SP5 indicates damage initiation in the region between the third and the fourth core of the HCU as shown in Figure 6.24 at a slip of 5.4 mm.

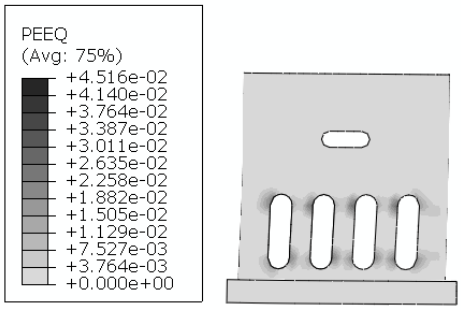

Figure 6.21 Contour plot of YP (PEEQ) for the numerical model SP5

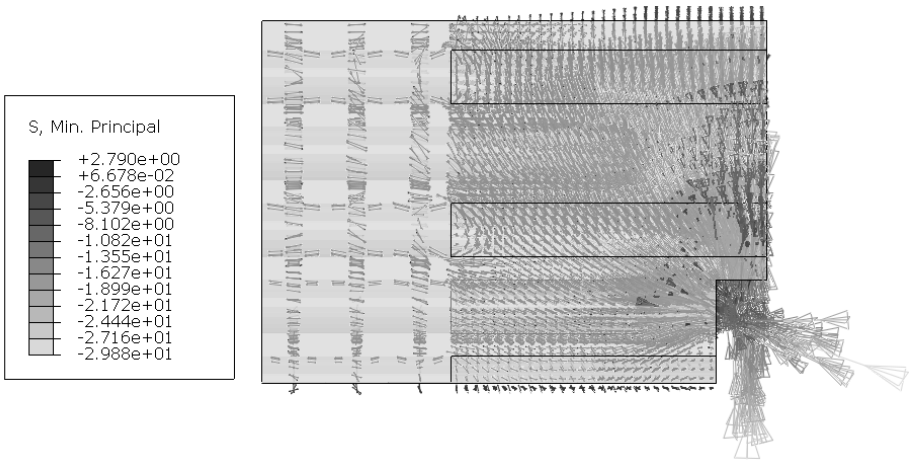

Figure 6.22 Minimum principal stress vectors for the slab of the model SP5

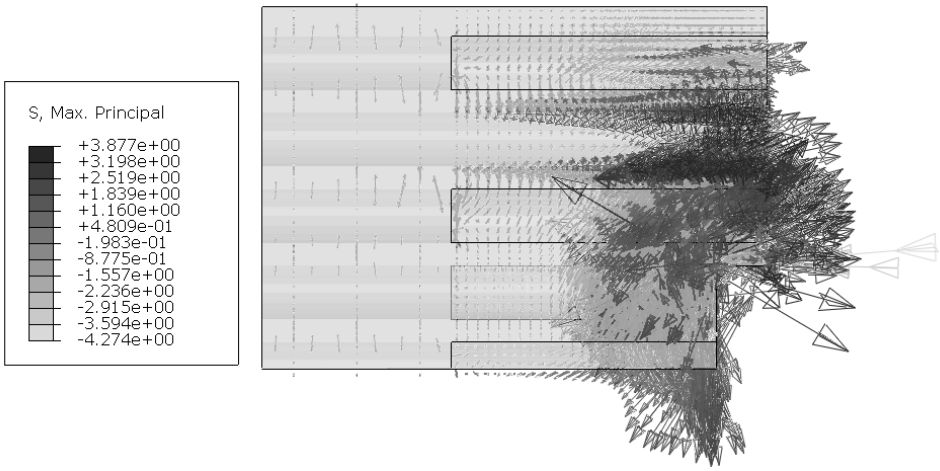

Figure 6.23 Maximum principal stress vectors for the slab of the model SP5

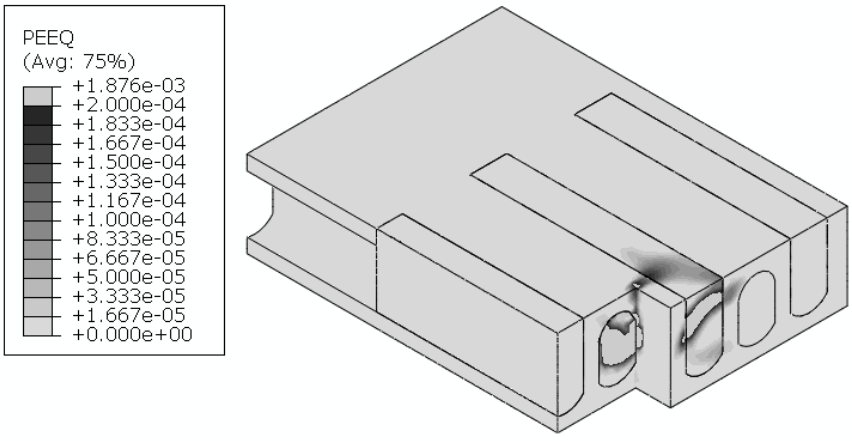

Figure 6.24 Contour plot of the slab (PEEQ) of the model SP5

The push out specimen SP6 failed in a mixed mode derived from the plastic bending of the YP and the brittle cracking of concrete exhibited at a later stage during the application of the load, as it was described in paragraph 5.2 of chapter 5. Figure 6.25

shows the contour plot of the equivalent plastic strain (PEEQ) of the YP for the numerical model SP6 at the end of the analysis. Figures 6.26 and 6.27 show the minimum and maximum principal compressive and tensile stress field respectively developed in the slab at the end of the analysis. Similarly to all the other specimens, the principal compressive stress field developed is small and the stresses are within the range of 2-15 N/mm^2. The maximum principal tensile stresses developed between the 3rd and the 4th core of the HCU are around 1.8 N/mm^2 exceeding the tensile strength of the *in situ* concrete which is equal to 1.7 N/mm^2. Figure 6.28 shows the contour plot of the equivalent plastic strain (PEEQ) of the slab of the numerical model SP6. The maximum plastic strains are concentrated between the third and the fourth core of the HCUs in the direction of the loading. The maximum plastic strain developed is equal to 7.5 10^{-3}. The numerical model developed for the specimen SP6 indicates that the tensile stresses developed in the slab exceed the tensile strength of the concrete slab in the region described above as well as initiation of plastic damage.

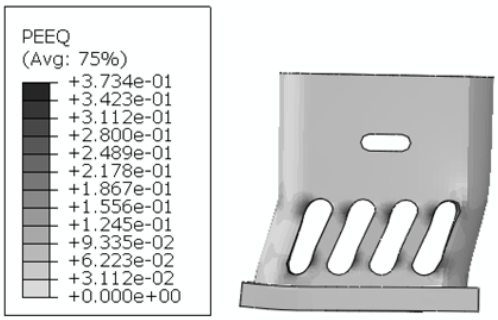

Figure 6.25 Contour plot of YP (PEEQ) for the numerical model SP6

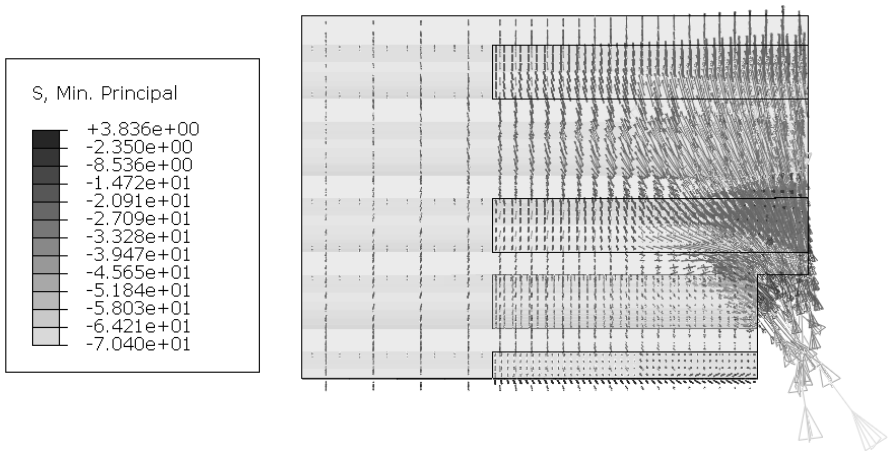

Figure 6.26 Minimum principal stress vectors for the slab of the model SP6

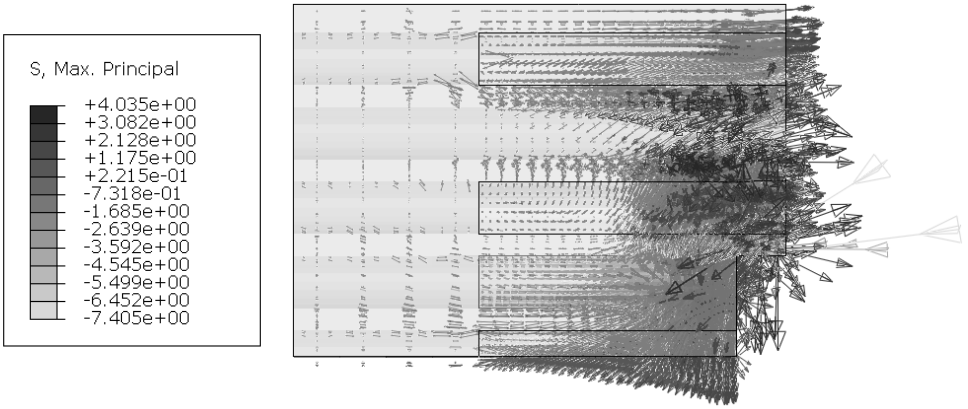

Figure 6.27 Maximum principal stress vectors for the slab of the model SP6

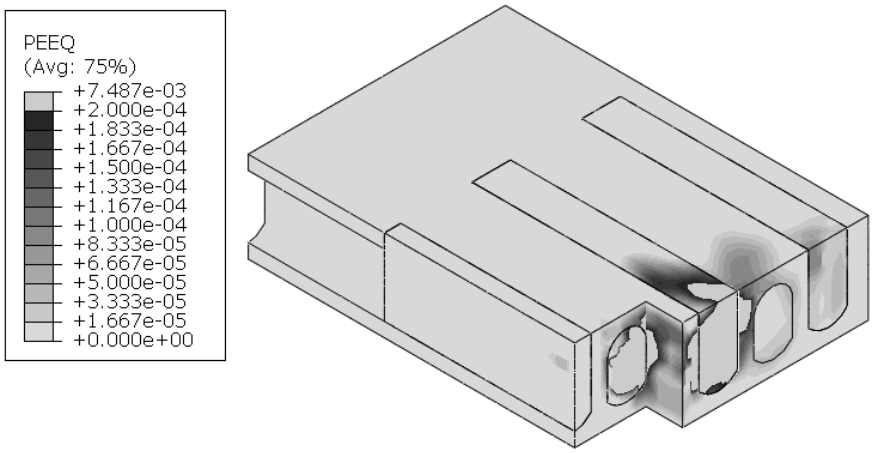

Figure 6.28 Contour plot of the slab (PEEQ) of the model SP6

The excessive deformation of the YP and the development of plastic strains at the ends of the steel strips and vertical walls demonstrated the ductile behaviour of the specimens SP1A, SP2B, SP3 and SP4B shown in tests. The minimum and maximum principal stress vectors which were extracted for these specimens indicated that the slabs are within elastic state of stress. Between the third and the fourth core of the HCU a diagonal principal tensile stress field was developed which was critical for the specimens SP5 and SP6, since the stresses developed exceeded the tensile strength of the concrete components. Additional critical regions including the second and the third core of the HCU were found for the specimens SP5 and SP6.

6.5.2 Force-slip Behaviour

Figures 6.29-6.32 show the experimentally determined force-slip curves of the push out specimens SP1A, SP2B, SP3 and SP4B respectively superimposed by the numerical

ones. The force-slip curve of the numerical model SP1A is almost identical to the experimental one up to 36 mm of slip. The force-slip curves of the numerical models SP2B, SP3 and SP4B are in very good agreement with the experimental ones. The numerical force-slip curve of the specimen SP2B diverges from the experimental one by 5% after the slip of 15 mm.

Figure 6.33 shows the experimentally determined force-slip curve of the push out specimen SP5. The numerical solution for the specimen SP5 is given up to 5.4 mm slip and corresponding force 338 kN. Since the numerical models included a number of material and contact non-linearities, the Standard solver provided by the Abaqus software cannot process effectively all the contact and material non linearities introduced to the models up to the maximum slips achieved in tests.

The numerical force-slip curve diverges from the experimental one. Taking into account that the application of the loading during the test SP5 was applied improperly due to imperfections of the HCUs, the actual boundary conditions of the problem is difficult to be represented in the numerical model.

Figure 6.34 shows the experimentally determined force-slip curve of the push out specimen SP6. The numerical force-slip curve of the specimen SP6 is in good agreement with the experimental one. Although the maximum force obtained in test is comparable to the one obtained from the numerical solution, 427 at 19.6 mm and 447 kN at 24.5 mm respectively, there is no evidence of the strength reduction shown in the experimental curve due to the initiation of shear cracking at 19.6 mm on the numerical force-slip curve. It should be noted that the numerical solution was based on a concrete mesh of around 15-20 mm. The influence of finer concrete mesh on the numerical solution should be investigated. A finer concrete mesh using the Standard solver tends to increase the contact problems during the analysis since the number of finite elements increases, making unstable the numerical solution which stops prematurely. The introduction of the damage parameters D_c and D_t [6.7] to capture the stiffness degradation of the concrete material after the maximum compressive and tensile stress is reached is not beneficial for the same reason. Nevertheless, the numerical models developed are still capable of predicting when the maximum stresses reach the concrete strength of the slabs, as shown in the previous paragraph.

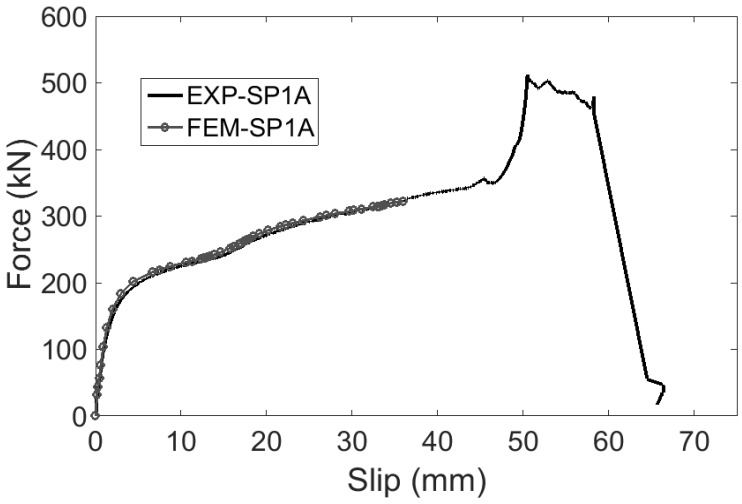

Figure 6.29 Force-slip curves of specimen SP1A

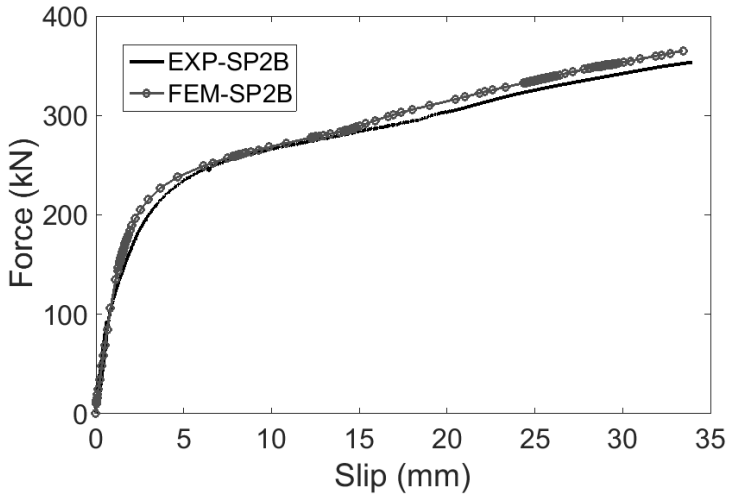

Figure 6.30 Force-slip curves of specimen SP2B

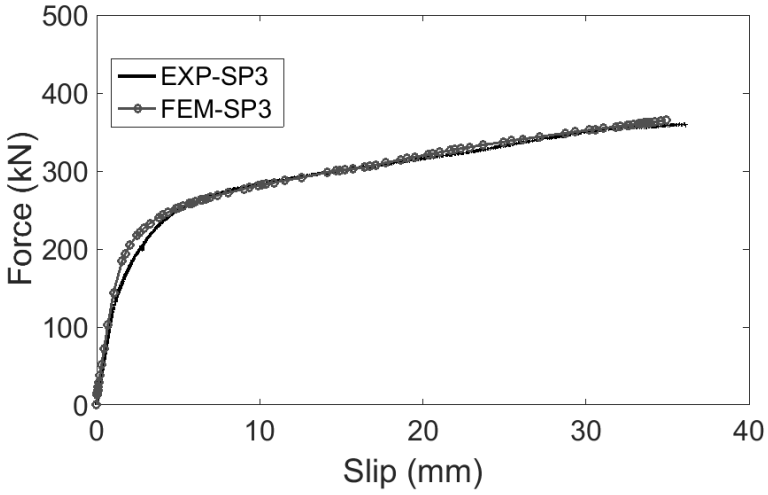

Figure 6.31 Force-slip curves of specimen SP3

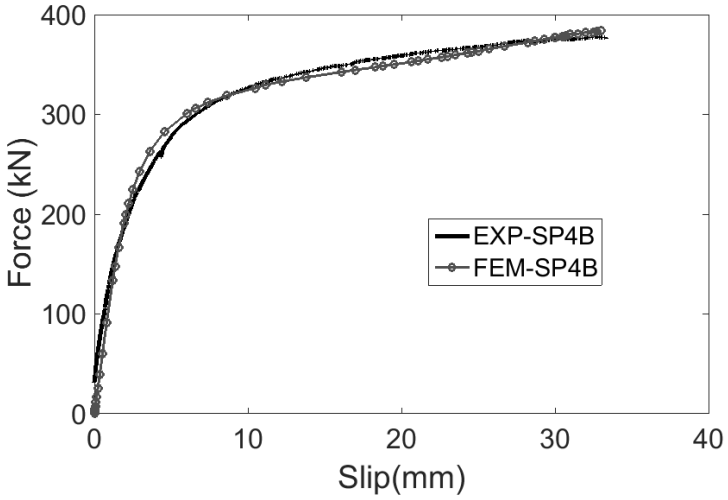

Figure 6.32 Force-slip curves of specimen SP4B

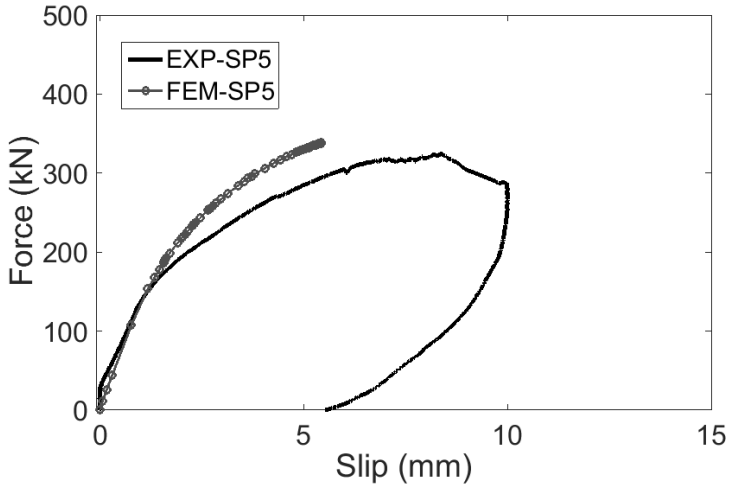

Figure 6.33 Force-slip curves of specimen SP5

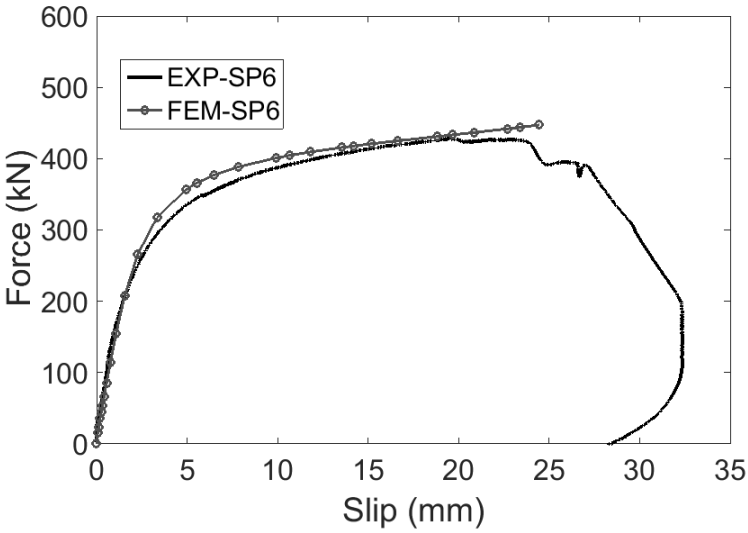

Figure 6.34 Force-slip curves of specimen SP6

6.5.3 Strength and Stiffness Comparisons

Table 6.1 summarizes the experimental and the numerical results including the experimental yield strength, $F_{y,exp}$, the maximum force obtained from tests, $F_{max,exp}$, the slip at the maximum force, $s_{max,exp}$, the measured stiffness, $K_{i,exp}$, the numerical yield strength, $F_{y,FEM}$, the maximum force obtained from the FEM analysis, $F_{max,\ FEM}$, the slip at the maximum force obtained from the FEM analyses $s_{max,\ FEM}$ and the stiffness obtained from the FEM analysis, $K_{i,FEM}$.

Table 6.2 gives the ratios between the experimental yield force to the numerical one indicated as $F_{y,exp}/F_{y,FEM}$, the maximum force obtained from tests to the numerical one, indicated as $F_{max,exp}/F_{max,FEM}$ and the stiffness obtained from tests to the numerical one indicated as $K_{i,exp}/K_{i,FEM}$. The ratio $F_{max,exp}/F_{max,FEM}$ shown in Table 6.2 is given only when the slip at the maximum force obtained from the experimental and numerical results is almost identical.

Based on the results shown in Table 6.2, the ratio $F_{y,exp}/F_{y,FEM}$ has a mean value of 0.98 with standard deviation 0.02 for all specimens apart from SP5, which indicates that the numerical models can accurately predict the yield force. The ratio $K_{i,exp}/K_{i,FEM}$ has a mean value of 0.97 with standard deviation of 0.08 which indicates that the stiffness measured in the tests can be reasonably predicted by the numerical models developed.

	Tests				FEM			
Specimen	$F_{y,exp}$	$F_{max,exp}$ (kN)	$s_{max,exp}$ (mm)	$K_{i,exp}$ (kN/mm)	$F_{y,FEM}$ (kN)	$F_{max,FEM}$ (kN)	$s_{max,FE,M}$ (mm)	$K_{i,FEM}$ (kN/mm)
SP1A	170	357	47	95	170	333	36	95
SP2B	200	339	33	123	210	360	33	110
SP3	230	359	36	135	230	365	35	135.2
SP4B	260	375	33	105	260	384	33	113
SP5	N.A.	321	8.3	110	N.A.	338	5.4	138
SP6	320	427	19.6	138	330	446	24.5	138.5

Table 6.1 Experimental and numerical results

Specimen	$\frac{F_{y,exp}}{F_{y.FEM}}$	$\frac{F_{max,exp}}{F_{max.FEM}}$	$\frac{K_{i,exp}}{K_{i.FEM}}$
SP1A	1	N.A.	1
SP2B	0.95	0.94	1.1
SP3	1	0.98	0.99
SP4B	1	0.98	0.93
SP5	N.A.	N.A.	0.80
SP6	0.96	N.A.	0.99

Table 6.2 Ratios between experimental and numerical results

6.5.4 Development of Strain in YP and Rebars

The results obtained from the strain gauges are represented in force-microstrain graphs. The force is the total force produced by the numerical solution at the end of each analysis. The development of microstrain recorded by the strain gauges in the tests was compared to the logarithmic microstrain (LE22) extracted from the Abaqus output file. Figures 6.35-6.41 show the results of the strain gauges installed on the YP for the specimens SP1A, SP2B, SP3, SP4B and SP5. It was chosen not to display more than four force-microstrain curves in the same graph in order the results to be more visible. The position of each strain gauge is shown in the inset of each figure. The strains were averaged approximately within a region equal to the size of the strain gauges.

The results indicate that the prediction of the strain gauge recordings by the numerical models is good. It is mentioned that the results are sensitive to the precise position of the strain gauges, to the mesh selected and to the region within which the strain is averaged. The excessive deformation of the YPs shown in specimens SP1A, SP2B, SP3 and SP4B is verified by the excessive strains developed in the steel strips and vertical walls of the YP reaching values up to 5000 με. The numerical model for the specimen SP5 indicates onset of yielding in the region where the gauge 1 was installed on the top end of the YP's steel strip reaching strains of slightly more than 2500 με, which is the yield strain of the material for the tube of 10 mm thickness.

Strain gauges were installed on the rebars of specimen SP6. Figure 6.42 shows the position of the three strain gauges installed on the rebars denoted as 'Rebar 1' and 'Rebar 2' of specimen SP6. The longitudinal stress (S11) along the axis of the rebars was extracted from the Abaqus output file at the end of the analysis. Figure 6.43 shows

the contour plot of the longitudinal stress (S11) developed in the two rebars of specimen SP6. The longitudinal stress in the precise position where the gauges 1, 2 and 3 were placed on the rebars of specimen SP6 is 104.63, 104.75 and 119.8 N /mm^2 respectively. The values obtained from the numerical solution are very close to the ones obtained from the experiments equal to 100 N/mm^2 approximately for all the gauges at the end of the test. According to the numerical solution extracted by the Abaqus, the position at which the tensile stress along the length of the rebars is maximized lies in the middle of each rebar.

Figures 6.44-6.48 show the contour plot of the longitudinal stress (S11) developed in the two rebars in specimens SP1A, SP2B, SP3, SP4B and SP5 respectively. Based on the numerical solutions, the maximum tensile stress developed in the two rebars at the end of each analysis is between 127-150 N/mm^2 for the numerical models SP1A, SP2B and SP3, while the same stress is between 200-227 N/mm^2 for the numerical models SP4B, SP5 and SP6. The results indicate that the rebars contribute to the shear resisting mechanism although they do not yield. The yield strength of the rebars was found 500 N/mm^2 according to the tensile test results presented in paragraph 4.3.1 of chapter 4.

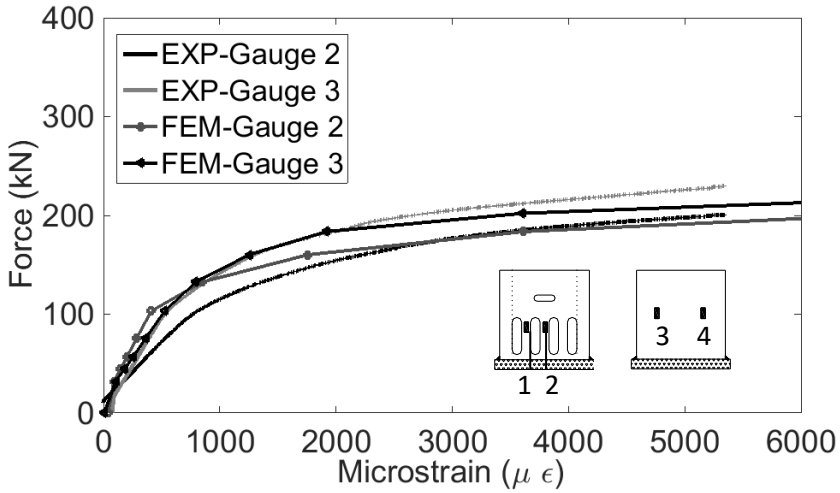

Figure 6.35 Force-microstrain curves of gauges 2 and 3 of specimen SP1A

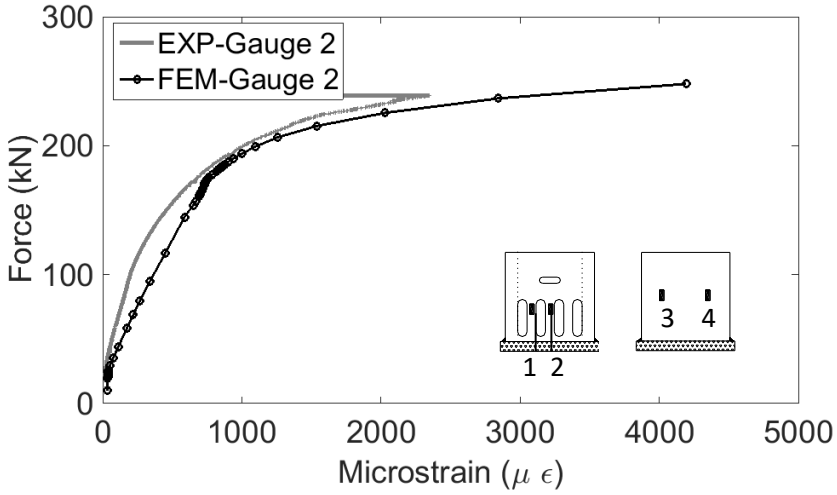

Figure 6.36 Force-microstrain curves of gauge 2 of specimen SP2B

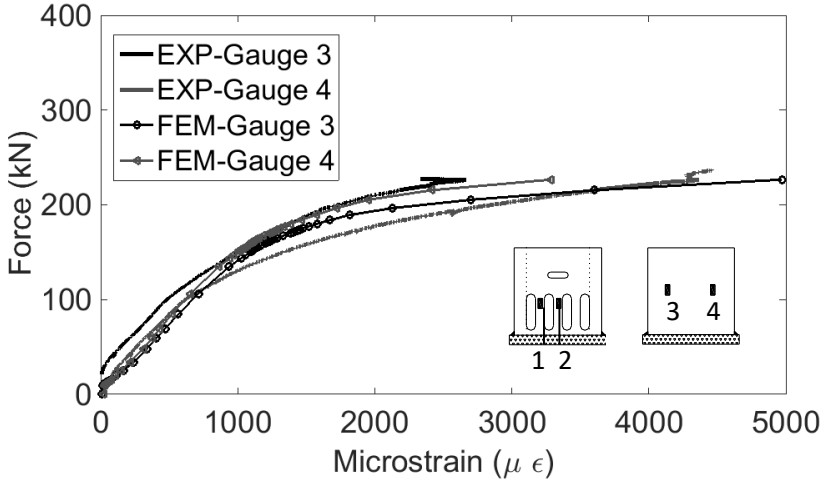

Figure 6.37 Force-microstrain curves of gauges 3 and 4 of specimen SP2B

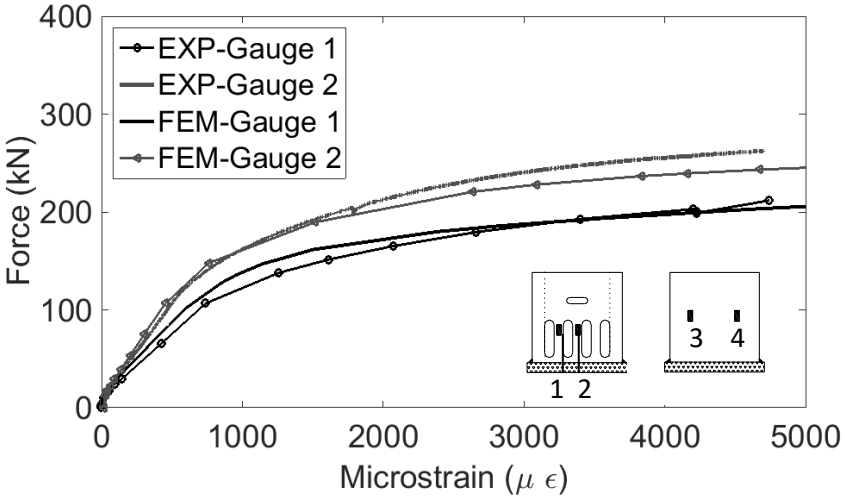

Figure 6.38 Force-microstrain curves of gauges 1 and 2 of specimen SP3

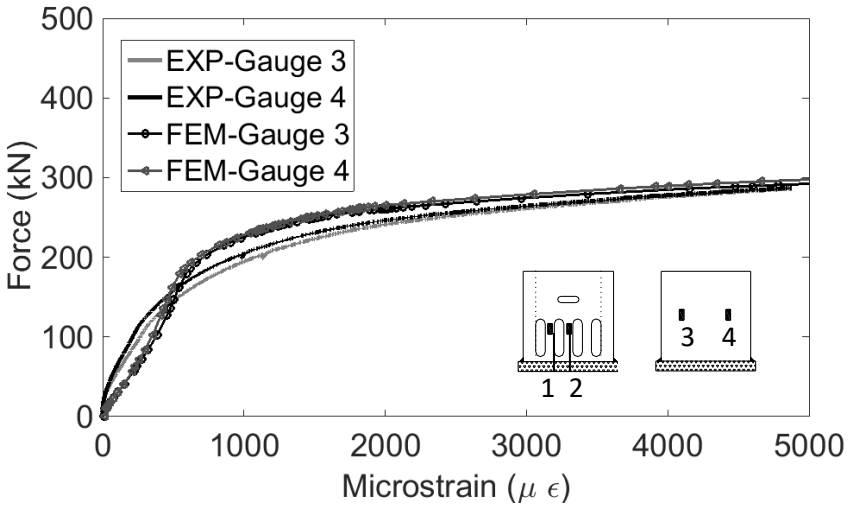

Figure 6.39 Force-microstrain curves of gauges 3 and 4 of specimen SP3

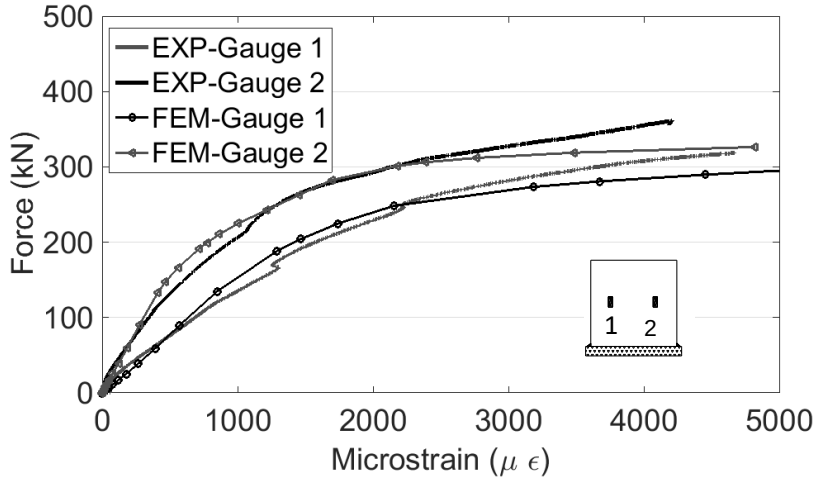

Figure 6.40 Force-microstrain curves of gauges of specimen SP4B

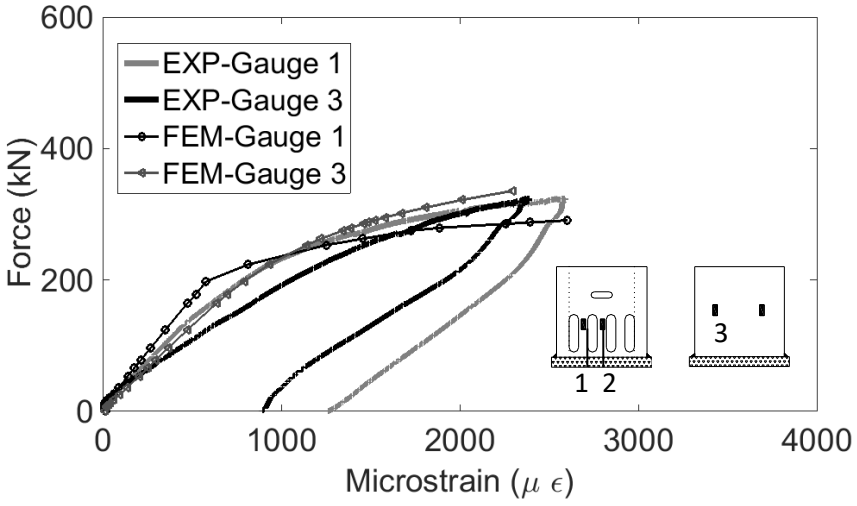

Figure 6.41 Force-microstrain curves of gauges of specimen SP5

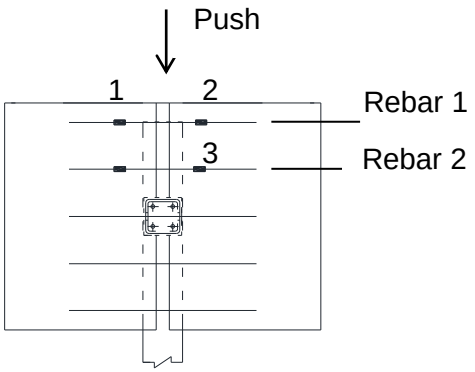

Figure 6.42 ‘Rebar 1’ and ‘Rebar 2’ of push out specimen SP6

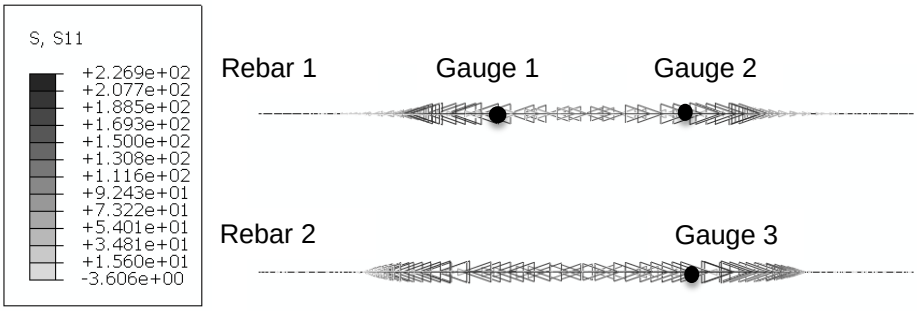

Figure 6.43 Contour plot of rebars (S11) of the numerical model SP6

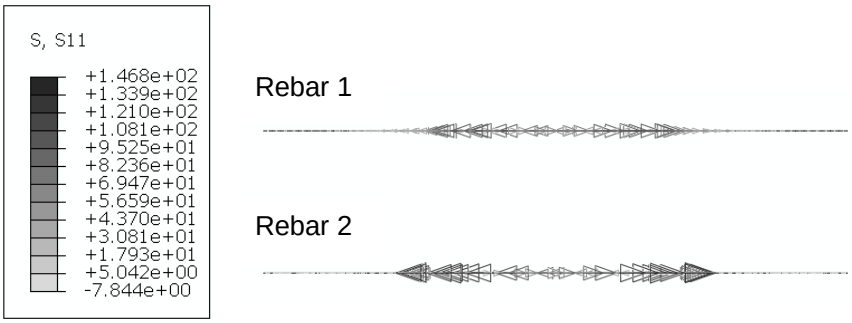

Figure 6.44 Contour plot of rebars (S11) of the numerical model SP1A

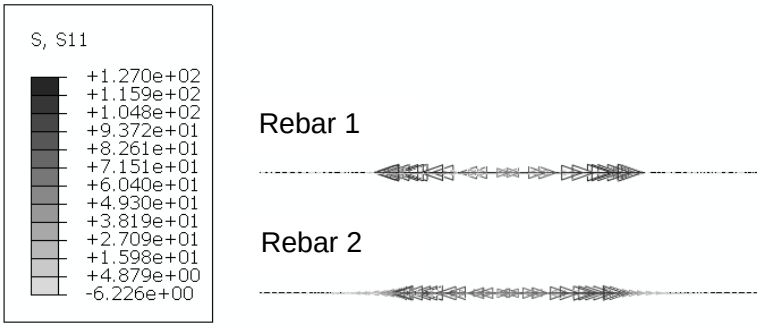

Figure 6.45 Contour plot of rebars (S11) of the numerical model SP2B

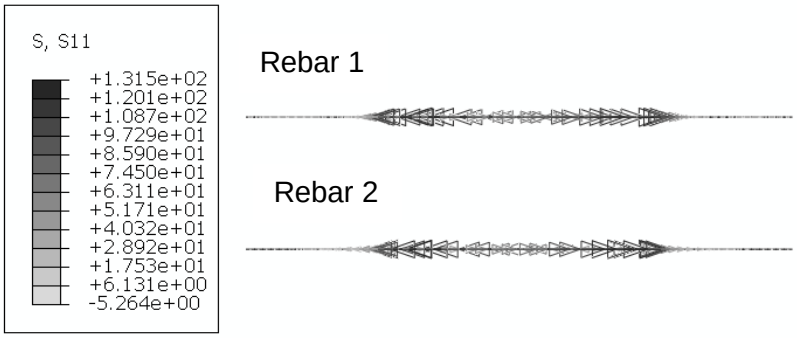

Figure 6.46 Contour plot of rebars (S11) of the numerical model SP3

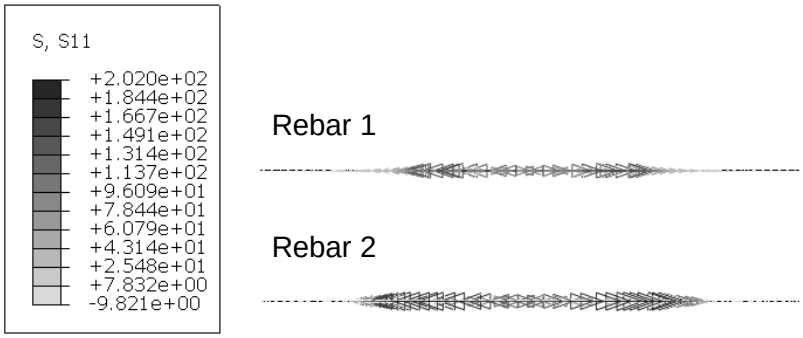

Figure 6.47 Contour plot of rebars (S11) of the numerical model SP4B

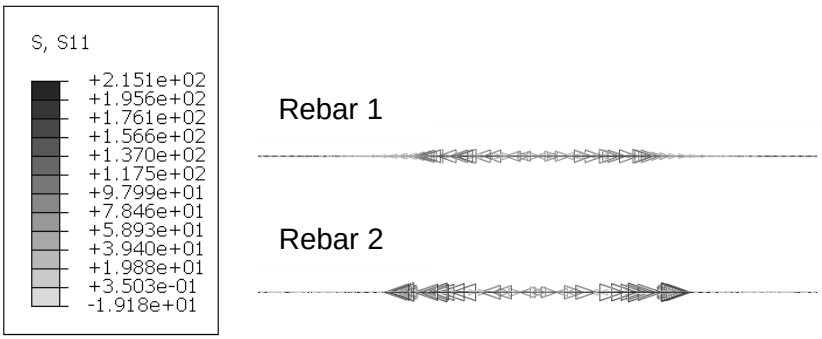

Figure 6.48 Contour plot of rebars (S11) of the numerical model SP5

6.6 Summary

Three dimensional non- linear numerical models were developed for the push out specimens SP1A, SP2B, SP3, SP4B, SP5 and SP6 using the Abaqus Standard software (v.6.14). The numerical models included material, geometric and contact non linearities. The concrete damage plasticity model provided by the Abaqus software was used considering isotropic compressive and tensile plasticity. Plastic stress-strain behaviour was taken into account for the steel parts of the connection. Hard contact and

penalty friction formulations were used to describe the normal and the tangential behaviour of all the contact pairs defined between concrete and concrete, and concrete and steel interfaces. The numerical results included the force-slip behaviour, the minimum and maximum principal stress vectors, the development of strains in the YP represented in force-microstrain graphs and the maximum tensile stresses developed in the rebars. The results showed that the behaviour of the specimens SP1A, SP2B, SP3 and SP4B was characterized by the plastic deformation of the YP up to 30-35 mm of slip. The minimum and maximum principal stress vectors which were extracted for the slabs of the specimens indicated that the slabs are within elastic state of stress. Between the 3rd and the 4th core of the HCU, a diagonal principal tensile stress field was developed which was critical for the specimens SP5 and SP6, since the stresses developed exceeded the tensile strength of the concrete components. The force-slip behaviour of the push out specimens can be accurately predicted by the numerical models when no shear cracking is involved. The results obtained from the strain gauges installed on the steel strips and vertical walls of the YP and represented in force-microstrain graphs showed good agreement with the numerical results extracted by the Abaqus output file. The tensile stress of around 100 N/mm^2 developed in the rebars of specimen SP6 was in good agreement with the one taken from the numerical solution. Based on the numerical solutions, the maximum tensile stresses developed in the rebars of all specimens were within 127-227 N/mm^2. This indicated that the rebars contribute to the resisting mechanism though they do not yield.

6.7 Reference List

[6.1] British Standards Institution (BSI). BS 5975: 2008+A1:2011, Code of practice for temporary works procedures and the permissible stress design of falsework, London, UK (2011)

[6.2] British Standard Institution (BSI), Draft prEN 12812 Falsework - Performance requirements and general design, Draft for Public Comment 97/102975DC, London, UK, April 1997

[6.3] fib Model Code 2010 for concrete structures. Comité Euro-International du Béton, Secretariat permanent, Case Postale 88, CH-1015 Lausanne, Switzerland, 180

[6.4] X.D. Dai, D. Lam, E. Saveri E., *Effect of concrete strength and stud collar size to shear capacity of demountable shear connectors*, J. Struct. Eng.141(11):04015025-1-04015025-10 (2015)

[6.5] X. Liu, M.A. Bradford, S.S.M. Lee (2014), *Behaviour of high strength friction grip bolted shear connectors in sustainable composite beams*., J. Struct. Eng., 141(6), 1-12 (2014)

[6.6] ASM International. <https ://www.asminternational.org/documents /10192/3465262/05105G_Chapter_1. pdf/e13396e8-a327-490a-a414-9bd1d2bc2bb8> (June 2018)

[6.7] ABAQUS 6.14. Analysis User's guide. DS SIMULIA Corp. Velizy Villacoublay, France (2014)

[6.8] J. Lubliner, J. Oliver, S. Oller, E. Onate, *A plastic-damage model for concrete*, Int. J. Solid Struct., 25, 299-329 (1989)

[6.9] J. Lee, G.L. Fenves, *Plastic-damage model for cycling loading of concrete structures*, J. Int. Eng. Mech, ASCE, 124(8), 892-900 (1998)

[6.10] A.S. Genikomsou, M.A. Polak, *Finite element analysis of punching shear of concrete slabs using damaged plasticity model in ABAQUS*, Eng. Struct., 98, 38-48 (2015)

[6.11] T. Jankowiak, T. Lodygowski, *Identification of parameters of concrete damage plasticity constitutive model*, J. Foundations of civil and environmental engineering, 6, 53-69 (2005)

[6.12] H. Kupfer, H.K. Hilsdorf, H. Rusch, *Behaviour of concrete under biaxial stresses*, ACI Journal, 65 (8), 656-666 (1979)

[6.13] Y. Sümer, M. Aktaş, *Defining parameters for concrete damage plasticity models*, Challenge Journal of Structural Mechanics, 1(3), 149-155 (2015)

[6.14] M. Pavlovic, Z. Markovic, M. Veljkovic, D. Budevac, *Bolted shear connectors vs. headed studs behaviour in push out tests*, J. Constr. Steel Res., 88:134-149 (2013)

[6.15] A. Prakash, N. Anandavalli, C. K. Madheswaran, J. Rajasankar, N. Lakshmanan, *Three Dimensional FE Model of Stud Connected Steel-Concrete Composite Girders Subjected to Monotonic Loading*, International Journal of Mechanics and Applications, 1(1), 1-11 (2011)

[6.16] J.C. Lim, T. Ozbakkaloglu, A. Gholampour, T. Bennett, R. Sadeghi, *Finite-Element Modelling of Actively Confined Normal-Strength and High-Strength Concrete under Uniaxial, Biaxial, and Triaxial Compression*, J. Struct. Eng. 142 (11), 04016113 (2016)

[6.17] BSI (British Standard Institution). BS-EN1992-1-1-Eurocode 2: Design of concrete structures, General rules and rules for buildings, London, UK (2004)

Chapter 7-Summary and Conclusions

7.1 Summary

A novel demountable steel yielding mechanism (YP) has been proposed for use in precast steel concrete composite beams in buildings. The proposed connection is benefited from the use of precast hollow core slab units (HCUs) offering standard advantages. It is the first attempt in the existing literature review that a demountable connection for use in steel concrete composite beams is used in conjunction with HCUs. The composite action between the HCUs and the steel section is achieved by the use of the YP. The unique shape of the YP promotes a ductile and predictable force-slip behaviour and allows for easy deconstruction since it is not fully embedded in the concrete opposingly to the conventional steel concrete composite connections. No usage of welding is required on site and all the component parts of the connection can be rapidly assembled. The large shape of the YP minimizes potential concrete failures as the shear force is distributed in a larger area into the concrete component compared to welded headed studs. The shear resistance and the stiffness of the DSC proposed can be controlled based on the chosen geometric features of the steel yielding mechanism. Twelve horizontal full scale push out tests were performed to investigate the physical behaviour of the DSC proposed. The results showed that the YP can achieve high shear strength and very high slip capacity, if properly designed. The deconstruction procedure was implemented within the lab environment. All the steel structural parts of the connection were reused over and over again in tests; the concrete slabs of one specimen were additionally reused in a new test up to ultimate loading without affecting the structural behaviour. Simplified equations were proposed based on plastic beam analysis and the results showed that can accurately predict the yield strength obtained from the tests. Shear cracking was found to be critical failure for the concrete slabs. It was found that the shear resistance of the concrete slabs can be reasonably predicted by the shear friction theory based on an existing model available in the literature review. Detailed non-linear numerical models for six push out tests (one numerical push out model per different shear connector geometry) were developed using the Abaqus Standard software (v.14). The results showed that the numerical models can predict the plastic behaviour of the YP and indicate critical regions where the tensile stresses exceed the tensile strength of the slabs.

7.2 Conclusions

Based on the results presented in the research work and within the boundaries of the experimental and numerical works undertaken, the following conclusions are drawn:

1) The YP allows for direct and easy assembly since all the component parts are prefabricated and no usage of welding is required on site. The deconstruction procedure is facilitated by the unique shape of the YP which is not embedded in the concrete slabs and can be implemented by working only from the top side of the steel section, thus minimizing the number of workers required for disassembly.

2) All the steel structural components apart from the YP are fully reusable under ultimate loading. The concrete slabs may be additionally reused provided that a proper design has been made to avoid early shear cracking. Potentially, all the structural components may be reused under service loading as no damage was observed in any structural part in tests during this range of loading.

3) The YP can provide high shear resistance. The yield strength of the YP achieved in tests was in the range of 170-320 kN and the maximum force obtained was 250-427 kN. A qualitative comparison with a common 19 mm diameter welded headed stud used in combination with HCUs indicates that the potential of the YP in terms of shear resistance is to achieve three times the shear strength of the former.

4) The YP can provide very high slip capacity reaching at least 30 mm slip for the specimens belonging to the group SP1-SP4 designed to have the ductile failure mode. The specimens SP5 and SP6 which failed in concrete shear cracking achieved 8.3 and 19.6 mm slip respectively, larger than the slip capacity required by the Eurocode 4 for ductile shear connectors.

5) The YP can provide a stiffness of 75-135 kN/mm depending on the selected geometric characteristics. A qualitative comparison with a welded headed stud of 19 mm diameter used in combination with HCUs indicates similar stiffness between the two.

6) The transverse slab separation measured for the specimens SP1A and SP6 was found equal to 1.98 and 2.48 mm respectively at 80% of the ultimate load and it is found to be within the specified limits of Eurocode 4 [7.1].

7) The yield strength of the YP can be accurately predicted by the simplified equations based on fundamental mechanics when there is no early concrete failure. The average prediction is within 6% with standard deviation equal to 0.05.

8) Shear cracking was found to be critical for the concrete component among other potential failures of the slabs, i.e. ripping, splitting and shear cracking. The shear resistance of the concrete slabs was reasonably predicted by the shear friction model proposed in Eurocode 2.

9) The push out specimens were designed to have a YP yield strength of 150-345 kN in combination with *in situ* concrete strength of 30-68 N/mm^2 in cubical samples. The specimens including *in situ* concrete strength of 38-68 N/mm^2 and medium YP yield strength of 150-260 kN exhibited ductile failure mode. The specimens SP5 and SP6 including *in situ* concrete strength of 30 and 35 N/mm^2 respectively and high YP yield strength, i.e. 345 and 310 kN respectively, failed in concrete shear cracking.

10) The specimen SP1C exhibited out of bending deformation which resulted in reduced shear resistance and stiffness. Therefore, a proper amount of concrete should be placed around the corners of YP to avoid this behaviour.

11) The initial concept included the use of innovative blind bolts to fix the YP on the top flange of the steel section. Based on the first two tests, the use of the blind bolts did not benefit the structural behaviour of the proposed connection; the blind bolts were not capable of resisting the combined shear and secondary bending moment introduced to the base of the YP and thus fixing together the YP and the top flange of the steel section. This further resulted in premature concrete failures.

12) The 4th core of the HCU located just before the YP in the direction of the load applied should be full of *in situ* concrete to avoid early shear cracking of the slabs based on the first test and to ensure the transfer of the shear from the YP to the concrete component; a solid amount of concrete placed at the position of the 4th core resists the tension stress field imposed by the YP to the concrete which is critical at this region.

14) The numerical models developed for six push out specimens showed that the plastic behaviour of the connection was characterized by the excessive deformation of the YP demonstrated in tests SP1A, SP2B, SP3 and SP4B. The stress vectors extracted by the Abaqus output file indicated that the slabs of these specimens remained within elastic state of stress, which is in good agreement with the experimental results. The force-slip curves for the specimens exhibited ductile failure mode were accurately predicted by the numerical models.

15) The maximum principal stress vectors extracted by the Abaqus output file for the specimens' slabs of SP5 and SP6 indicated critical regions, i.e. between the third and the fourth core of the HCUs and the second core of the HCUs, where the stresses developed in the slabs approached the tensile strength of the concrete components. The reduction of the strength shown in the experimental force-slip curves of those specimens due to shear cracking could not be obtained. It is recommended that the Explicit solver should be used which is capable of modelling efficiently complex non - linear problems including contact and material non linearities. The influence of the concrete component's mesh size should be investigated on the results.

16) The minimum principal stress vectors extracted by the Abaqus output file indicated a diagonally developed compressive stress field which is very small for all the specimens. This is in good agreement with the strain gauges results installed on the concrete region around the YP and closer to the corners of it which recorded very small compressive strains of less than 500 με.

17) The steel rebars placed in the cores of the HCUs contribute to the shear transfer mechanism although they do not yield as confirmed by the gauges' results installed on the rebars of specimen SP6 and by the FEM results extracted for the six push out specimens. According to the numerical solutions, the rebars contribute to the shear resisting mechanism with less than half their yield strength.

18) The excessive deformation of the YPs shown in the experiments was verified by the numerical results. The plastic strains at the top ends of the YPs steel strips and vertical walls reached excessive strains of 5000 με. The YP of the specimen SP5 exhibited onset of yielding reaching strains of slightly more than 2500 με, which is the yield strain of the material, in the region close to the top end of the steel strips.

7.3 Future Research

The following suggestions are proposed for further research:

1) Parametric numerical analyses to expand the experimental results obtained within this research project including a range of *in situ* concrete strengths for each YP geometry. The Abaqus/Explicit solver considering quasi-static analysis should be used which is more efficient to solve a number of complex non linearities. The results obtained from the parametric analyses can be used for the establishment of a reliable design procedure for the demountable steel concrete composite beams using YPs in conjunction with HCUs.

2) The push out specimens designed within this research project included the 4^{th} core of the HCUs located just before the YP in the direction of the loading full of *in situ* concrete. Parametric experimental and numerical analyses may be conducted to investigate the influence of the non -filled with *in situ* concrete 4^{th} core of the HCUs on the failure modes and the force-slip behaviour.

3) The geometric shape of the YP can be changed so as to increase the shear resistance and stiffness of the proposed DSC by including structural tubes of rectangular hollow sections (RHS) additionally to the squared hollow section (SHS) used in the present research work.

4) The method and the means of deconstruction should be optimized so as to remove limited amount of concrete around the YP upon disassembly of the demountable connection. The deconstruction may be facilitated using a coupler in the middle rebar and thus avoiding to cut it. The optimized solution should be retrieved in collaboration with the relevant Industry.

5) Full scale composite beam tests should be performed to overall investigate the behaviour of the YP under combined longitudinal shear and bending moment.

6) The usage of the YP as shear connector may be extended in steel concrete composite beams with solid precast concrete planks.

7) More parametric experimental and numerical studies in this thesis may be conducted so as to include more parameters, e.g. thickness of the YP's steel base, steel material of YP and steel base.

7.4 Reference List

[7.1] BSI (British Standard Institution). BS EN 1994-1-1: 2004: Design of composite steel and concrete structures- Part 1.1: General rules and rules for buildings, London , UK (2004)